ION EXCHANGE MEMBRANE SYSTEMS: MODELING AND OPTIMIZATION FOR SALINITY GRADIENT ENERGY GENERATION

A Dissertation
Presented to
The Academic Faculty

by

Bopeng Zhang

In Partial Fulfillment
of the Requirements for the Degree
Doctor of Philosophy in the
School of Civil and Environmental Engineering

Georgia Institute of Technology
August 2018

ION EXCHANGE MEMBRANE SYSTEMS: MODELING AND OPTIMIZATION FOR SALINITY GRADIENT ENERGY GENERATION

Approved by:

Dr. Yongsheng Chen, Advisor
School of Civil and Environmental Engineering
Georgia Institute of Technology

Dr. Shuman Xia
School of Mechanical Engineering
Georgia Institute of Technology

Dr. John Crittenden
School of Civil and Environmental Engineering
Georgia Institute of Technology

Dr. Xing Xie
School of Civil and Environmental Engineering
Georgia Institute of Technology

Dr. Sotira Yiacoumi
School of Civil and Environmental Engineering
Georgia Institute of Technology

Date Approved: May 2, 2018

To Rongrong, my wife who has been the most supportive during my years of effort.
And to Caleb, my son whose smile shines my life.
I love you.

ACKNOWLEDGEMENTS

First, I would like to express my deepest gratitude to my thesis advisor, Dr. Yongsheng Chen, who has supported my opportunity to conduct my research. His valuable and detailed guidance, teaching, and mentoring throughout my years of study has brought this thesis to fruition. His pertinent advice and guidance on my career development is also greatly appreciated.

I would also like to thank my committee members Dr. John Crittenden, Dr. Sotira Yiacoumi, Dr. Shuman Xia, and Dr. Xing Xie for their time and precious comments on my research. Their invaluable advice and discussions were of great help to shape my research.

My special thanks also go to every member in Dr. Chen's group. I would like to thank my friend Dr. Jin Gi Hong, a graduate from the group, for all previous guidance and help in my early years. Dr. Kungang Li, a graduate from the group and my friend, for his help and encouragement on my research. I also appreciate my current colleagues and collaborator, Haiping Gao, Xin Tong, Xiaoyang Meng, Thomas Igou, Jahanzeb Khan, Chunyan Xu, and Su Liu, for the great atmosphere in the office and lab, and great discussions on our research. I also thank my former collaborators, visiting scholars, Dr. Carolina Fernandez-Gonzalez, Dr. Hongguo Zhang, Dr. Elif Demirel, Shihua Xie. I am also indebted to Dr. Guangxuan Zhu for his support on lab management.

Last but foremost, my biggest thanks and love go to my wife, Rongrong and my adorable son, Caleb. I also would like to thank my parents and parents-in-law for their support with full heart and faith in me.

TABLE OF CONTENTS

LIST OF TABLES

LIST OF FIGURES

LIST OF ABBREVIATIONS

AEM	Anion exchange membrane
AC	Alternating current
AFM	Atomic force microscope
BESs	Bioelectrochemical-based systems
CEDI	Continuous electrodeionization
CEM	Cation exchange membrane
DBL	Diffusion boundary layer
DC	Direct current
DI	Deionized
DMSO	Dimethyl sulfoxide
DS	Degree of sulfonation
ED	Electrodialysis
EDX	Energy dispersive X-ray spectroscopy
EIS	Electrochemical impedance spectroscopy
FCD	Fixed chare density
FE-SEM	Field emission scanning electron microscope
FTIR	Fourier transform infrared
GPE	Glycidyl phenyl ether
IEC	Ion exchange capacity
IEMs	Ion exchange membranes
IERBs	Ion exchange resin beads
MFC	Microbial fuel cell

MRC	Microbial reverse electrodialysis cell
NMP	N-Methyl-2-pyrrolidone
NP	Nanoparticles
PE	Polyethylene
PMMA	Poly(methyl-2-methacrylate)
PPO	Poly(2,6-dimethyl-1,4-phenyleneoxide)
PRO	Pressure retarded osmosis
PVC	Poly(vinyl) chloride
RED	Reverse electrodialysis
RO	Reverse osmosis
SD	Swelling degree
SPPO	Sulfonated poly(2,6-dimethyl-1,4-phenyleneoxide)

SUMMARY

The development of renewable and sustainable energy-conversion technology is widely recognized as an important strategy for global energy security. Water salinity is one such renewable energy source that has yet to be explored. Through the mixing of freshwater with salt water, free energy is created, thus the chemical potential of low salinity water and high salinity water can be converted into electrical energy. One of the most promising techniques to harvest salinity gradient energy is reverse electrodialysis (RED). In RED, the controlled mixing of two aqueous solutions with different salinities leads to a change in Gibbs free energy that can be liberated as electrical energy through ion transport across ion exchange membranes (IEMs). RED technique is still not ready for commercialization, because system power output efficiency is often limited in natural water conditions. In a RED stack, cation exchange membranes (CEMs) and anion exchange membranes (AEMs) are crucial components for the overall energy generation efficiency. Considering the nature of the electrochemical cell system, it is conceivable that the membrane properties – ionic conductivity and permselectivity – have significant effects on RED power performance. Specifically, high conductivity with high permselectivity are desirable for RED. A better understanding of factors determining membrane conductivity and permselectivity will therefore be critical to commercialize RED technology.

This study focuses on advancing the understanding of IEMs through modeling and experimental validation to improve power generation efficiency of the RED stack. Specifically, insights derived from literature review have resulted in greater understanding of limiting factors including system conductivity. Efforts were made to significantly

increase the conductivity in the compartments filled with low concentration solution. As this limiting factor has been mitigated, the next improvements must be achieved on IEMs. A theoretical model was developed and validated, incorporating factors affecting membrane conductivity in the RED stack application environment. The membrane conductivity and other properties become complicated upon mixing of nanomaterials during membrane synthesis. Therefore, mechanism exploration through modelling and simulation was also fruitful. Furthermore, the microstructure variation has also displayed a correlation with membrane thickness and was explained by statistical modeling and simulation. Based on the model and simulation results, a deepened understanding of membrane conductivity and permselectivity now enable future fine-tuning of membrane properties during material selection and synthesis processes.

In summary, this dissertation has advanced our understanding of IEMs and application in salinity gradient energy generation using RED techniques. Specifically, several computational modeling and simulation methods have successfully revealed underlying characteristics of IEMs with respect to their conductivity and permselectivity. With this new knowledge, optimization approaches of the RED system are better informed. Furthermore, most theoretical derivations and model simulations are generic and therefore, can potentially be used in similar systems including electrodialysis. Overall, the results of this study are anticipated to benefit the future optimization of energy-capture in RED and provide a better pathway for sustainable salinity gradient power generation.

CHAPTER 1. INTRODUCTION

The growing concern of energy scarcity and environmental impacts related to conventional energy production have galvanized the exploration of sustainable energy technologies. As early as 1954, technologies using the reverse electrodialysis (RED) process to harvest energy have been realized by mixing solutions of different electrochemical potentials [1]. In the 1970s, prototypes appeared leveraging either RED or controlling reverse osmosis process to achieve energy generation [2, 3]. With respect to natural systems, solutions available for potential mixture can be found at the intersection of river estuaries and oceans where freshwater and seawater meet. Theoretically, the potential energy generation from mixing these two sources is equivalent to water falling over 270 m, with a total power of 2.4 – 2.6 TW [1, 4-6]. If an even higher salinity gradient is considered, such as that found between desalination concentrate and brackish water, the energy potential could be even higher [7]. Salinity gradient energy remains a largely untapped resource, and increased development of an engineered and optimized energy-capture method is needed. The two most promising approaches in capturing salinity gradient energy are formally known as (1) pressure-retarded osmosis (PRO), a membrane technology using semi-permeable membranes and (2) RED, which contains an alternating arrangement of ion exchange membranes (IEMs) in a stack similar to an electrodialysis stack. The successful application of RED for salinity gradient power mainly depends on membrane performance like many other membrane-based systems, so the role of membranes is of considerable importance in maximizing the RED power performance.

Today, IEMs have attracted wide interest and growing research and practical applications across various fields ranging from water treatment to industrial separation, to power generation, particularly using electrodialysis (ED), electrodialysis reversal (EDR), and fuel cell. Normally, each application emphasizes own physical and electrochemical requirements as the properties of membranes. The membranes, as a key component in this electrochemical system, its properties have been studied by many researchers to determine preferred characteristics and to investigate their significance to the power performance. Considering the nature of the electrochemistry cell system, it is convincible that the membrane properties such as electrical area resistance, permselectivity, and ion exchange capacity, have significant effects on RED power performance. Specifically, low area resistance, high selectivity, high ion exchange capacity, and high charge density are reported to be desirable for ion exchanging process such as RED. As a result, study on fundamental properties of IEMs would potentially guide future material selection and synthesis. With hurtles solved, the RED power generation using salinity gradient has a great potential to play a vital role in the sustainable development of energy sources. Thus, the focus of this study is on the RED system and associated IEM properties.

In this dissertation, Chapter 1 provides a comprehensive literature review on the state-of-the-art development in salinity gradient energy generation using RED. Key membrane properties of concern in RED application has been summarized. Physicochemical processes affecting RED performance are also elaborated and current modeling work from literature has been summarized. Finally, the evaluation of RED performance is introduced.

Chapter 3 focuses on an investigation of the application of ion exchange resin in beads form in the RED stack. The stack conductivity has been improved and led to a better power generation. Modeling of conductance of different components in the resin-packed compartments revealed the mechanism of improved conductivity.

Chapter 4 demonstrates the work on a deeper understanding of IEM ionic conductivity (or resistance) under different measuring environments. As validated by experimental data, the model has been proven to predict apparent membrane resistance as determined by bulk material and hydrodynamic factors.

Chapter 5 dives deeper to study the microstructure of polymeric bulk material of membranes. A modeling study has revealed that incorporating certain dose of nanoparticles into the cation exchange polymeric backbone is beneficial in conductivity because of microstructural change by nanoparticles. The improvement of membrane increased with increased dose until the aggregation of nanoparticles decreased the marginal gain from more nanoparticle dose.

Chapter 6 investigates the findings of a statistical model work on the microstructure of membranes. Modeling results were extension of previous model studies and validated by experimental data. The dependency of membrane permselectivity has been successfully explained by simulation of microstructure variations of different microphases by simplifying membrane spatial structure as a simple cube lattice.

Chapter 7 summarizes findings in the dissertation and recommends future research direction.

CHAPTER 2. RESEARCH OBJECTIVES

Given the background and literature review of salinity gradient energy harvesting through RED, in this chapter, I will specify my research objectives and rationale.

2.1. Research Objectives

The overarching goal is to determine approaches to optimize RED system performance with respect to salinity gradient power generation. Throughout my research, I have applied an integrated methodology by combining theoretical modeling and simulation with experiments. Data collected from experiments are used to validate mathematical models or statistical simulations that provide more insights into underlying physical processes. Applying developed models renders predictive power and potential guidance to further experiments.

Specifically, a comprehensive literature review and preliminary study has been conducted on the RED system that pinpointed two key optimization parameters: 1) the overall ionic conductance, and 2) stack electrical potential from accumulated membrane potential. Then, the research aims to solve the problems individually by: 1) significantly improving ionic conductivity in dilute solution compartments in the stack; 2) modeling and predicting parameters that determine IEM conductance and permselectivity, and therefore affect stack conductivity and potential.

Considering these objectives, I consider the following hypotheses:

- Power density from a RED stack is considered as the only indicator of RED performance.
- Salinity gradient is fixed on a level between seawater and river water considering the wide availability and ease of application.
- Another major contributor to stack resistance, IEM, can be optimized by incorporating nanoparticles into the polymeric chain. However, there exists an optimum degree of nanoparticle loading to the polymer matrix which can be explained by nanoparticle aggregation.
- Conductivity and permselectivity of membranes are determined by membrane microstructure. A simulation based on statistical analysis can model the change of microstructure and transport properties upon physical and chemical property changes (e.g. thickness of membrane and swelling of membrane).

2.2. Originality and Merit of the Research

The findings of this dissertation are original and have deepened the understanding of both RED and IEMs. Specifically, the knowledge gained from this dissertation is dedicated to the development of better performing IEMs and improving salinity gradient energy generation through the following five achievements:

- Optimization of RED stack performance through novel approaches;
- Better understanding of factors affecting membrane resistance measurement;
- Theoretical explanation of property improvements of nanocomposite IEMs;
- Balanced membrane permselectivity and conductivity design through simulation;

- Modeling and simulation results are generic and therefore applicable to other related fields (e.g. electrodialysis).

CHAPTER 3. BACKGROUND AND LITERATURE REVIEW

3.1. Principles of RED

RED is characterized by alternating cation and anion exchange membranes in a system similar to an electrodialysis stack. Instead of conducting desalination or acid-base production, RED aims to harvest energy from the created salinity gradient. The compartments between these membranes are filled with high concentration solutions and low concentration solutions in an alternating fashion (Figure 1). Ion exchange membrane arrays guide the direction of ion transport (cations to the right and anions to the left in Figure 1) driven by chemical potential difference (salinity difference) between the solutions to generate voltage across the membrane. This voltage accumulates over each membrane throughout the entire RED stack and drives an electrical current if an external circuit is configured with power-harvesting devices. A redox pair (usually $K_4Fe(CN)_6$ / $K_3Fe(CN)_6$), contained in the solution in two end chambers in contact with electrodes, facilitates the transformation of ionic current to mobilize electrons in the wire. To harvest energy continuously, the solutions in different compartments flow at a set rate to maintain membrane potential throughout the stack.

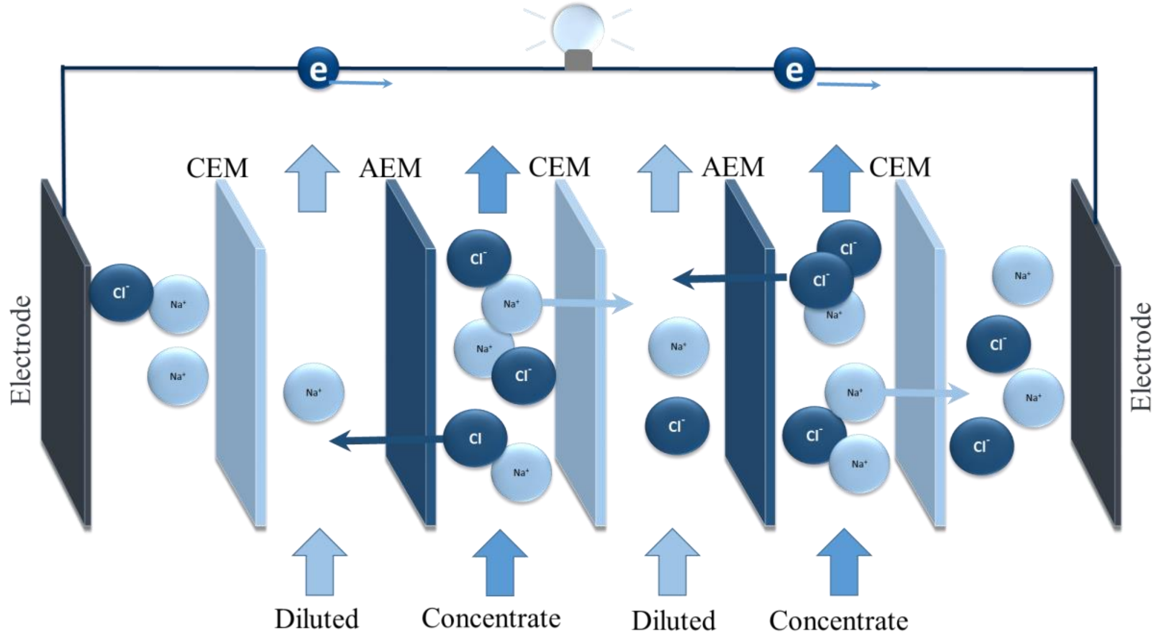

Figure 1 – A schematic representation of a RED stack with two cells. The redox pair helping ionic current to electron flows in the wire is not depicted. Concentrate and diluted feed solutions are usually supplied continuously to maintain the stack potential and non-deteriorating current flow.

3.2. Key Membrane Properties of IEMs in RED

As key components in a RED stack, IEMs largely influence the effectiveness and efficiency of RED system. Therefore, IEM properties have long been the focus of scientists and engineers who are trying to improve the efficiency of the system. Plenty of research has been conducted to optimize electrochemical system performance, but little research has focused on the desired properties of IEMs and the important roles they can play in optimizing RED systems.

IEMs are ion containing polymer electrolytes, which can be classified as part of both cation exchange membranes (CEMs) and anion exchange membranes (AEMs). CEMs contain negatively charged functional groups, which allow the transport of cations but repel anions. Meanwhile, AEMs contain positively charged functional groups and have the inverse ability regarding ion permeation.

3.2.1. Ionic resistance and permselectivity

Because the RED system is essentially a dialytic battery, the ionic resistance (or ionic conductivity since ions are actually conducting electricity) of an RED system is analogous to the internal resistance of a battery. As a major part of this internal resistance, the ionic resistance of IEM in the RED system is typically measured experimentally. Similar to the internal resistance of a battery, the ionic resistance determines the energy loss in an operating stack, which affects the power output of the system [8, 9].

The determination of membrane resistance is not straightforward because the measurement is usually taken while the membrane is in a solution as encountered in power generation applications; however, the conditions, such as the solution concentration, temperature, concentration gradient across the membrane, and experimental methods all affect measurement and results. This cause and effect relationship necessitates a detailed discussion.

The ionic resistance of membranes is commonly measured using indirect methods (no direct contact of the electrodes and the membrane) in RED research [8-12]. Alternating current (AC) is preferable because it avoids electro-chemical reactions that may occur during measurement and is more accurate in differentiating the pure membrane resistance from common resistance, including diffusion boundary layer (DBL) and double layer effects. Direct current (DC) is also reported to be useful in resistance measurements [8, 11, 13]. Membranes to be measured are immersed in sodium chloride or potassium chloride solutions of concentrations of 0.5 M or 1.0 M; however, the resistance may change with different external solutions and temperatures [10, 14].

In RED applications, IEMs divide salt solutions of different concentrations. As a result, the apparent membrane resistance is significantly different from the measured value in a 0.5 M NaCl solution [10, 15]. Therefore, a more comprehensive measurement of membrane resistance considering the effect of the external solution concentration is critical in modeling the RED system. Two techniques, namely chronopotentiometry and electrochemical impedance spectroscopy (EIS), have been used to solve difficulties during membrane resistance measurement.

Chronopotentiometry is widely used to investigate kinetic effects and adsorption during the transport process in IEMs [16, 17]. Through chronopotentiometry studies, the time dependence of the concentration gradients and the thickness of DBL under different current density can be determined. In addition, the validity of the Nernst-Planck equation and the Donnan theory are also confirmed under transient conditions [16, 18]; however, chronopotentiometry is not sufficient for measuring the double layer and quantifying its electrochemical effect on the membrane.

EIS is a technique used for studying and characterizing the electrical properties of porous materials and can be used to characterize IEMs. EIS provides another perspective in the study of the IEM system by equating the system to an electrical circuit with capacitors and resistors [19, 20]. The existence of three sub-layers of the IEM system, including the membrane, the electrical double layers, and the DBLs, have been studied using the EIS technique, and the quantitative circuit model has been established [19]. By changing the frequency of the applied AC potential, the resistance of the solution and the electrical double layer can be differentiated [11, 21]. For example, when the applied AC frequency is low or when DC is applied to the membrane system, the resulting electrical equivalent circuit indicates the effect of the diffusion layer and the electrical double layers as well as their contribution to the total electrical resistance of the system. Finally, an analysis under high frequency AC reveals the resistance attributed to the membrane polymer itself [22].

Permselectivity describes the ability of a membrane to prevent co-ions from passing through the membrane. It is measured by transport number and related to the fixed charge concentration of the membrane and the external solution concentration. Theoretically, a perfect IEM would have a permselectivity of one when the complete exclusion of the co-ions from the membrane is achieved; however, according to Donnan’s theory, a certain amount of co-ions could contribute to the transport current [23, 24]. Thus, the permselectivity would decrease below the ideal value of 1 as the solution concentration increases [14].

In practice, the apparent permselectivity is of more concern in RED because it determines the membrane potential (E_m) achievable under the given circumstances according to the following equation [25]:

$$E_m = \alpha_m \frac{RT}{F} \ln\left(\frac{\alpha_c}{\alpha_d}\right) \tag{1}$$

where α_m is the apparent membrane permselectivity (dimensionless), R is the gas constant ($J \cdot mol^{-1} \cdot K^{-1}$), T is the absolute temperature (K), F is the Faraday constant ($C \cdot mol^{-1}$), α_c is the activity ($mol \cdot L^{-1}$) of the concentrated salt solution, and α_d is the activity ($mol \cdot L^{-1}$) of the diluted salt solution.

The relationship between the permselectivity and the ionic resistance of the membrane is complicated because of the interactive effects from fixed charged groups and membrane swelling, as discussed in the previous section. Some researchers have concluded that it is not necessary to achieve both high permselectivity and low ionic resistance because an RED system can tolerate moderate permselectivity. After all, the main goal is to produce electricity and not to separate solutions [9]. The requirement of membrane resistance is stricter for an RED application than an ED application because the improvement of membrane conductivity is a step in the process of optimization; however, efficiency is the major hurdle that a successful RED application must overcome. Thus, membrane resistance is central to this hurdle because it is the key parameter that determines system efficiency. On the other hand, the permselectivity is more important in the ED process, especially for continuous deionization in which the purity of the products is of greater concern [26, 27]. This allows the resistance to be sacrificed to some extent. In summary, the development and synthesis of IEMs with well-balanced permselectivity and low resistance is desirable to optimize the RED salinity gradient power generation process [28].

3.2.2. Thermal stability, chemical stability, and mechanical strength

The thermal stability of IEM depends on the crosslinking degree, thermal stability of inert polymers, and reinforcing fabric (e.g., poly(vinyl) chloride or PVC and polyethylene (PE)). The size of the counter-ion also affects the thermal stability of the membrane [29]. In general, the requirements ensuring thermal stability of IEMs used in RED are not high when compared to thermal stability requirements for more common devices such as fuel cells [30]. The common temperature used for RED systems is generally around room temperature with a possible seasonal variation within 30 K.

Chemical stability depends on the durability of the membrane in various acidic or alkaline solutions. In general, cation exchange members (CEMs) are more durable than anion exchange membranes (AEMs) in terms of both thermal stability and chemical stability in strongly acidic and strongly alkaline solutions because the quaternary ammonium groups in AEMs tend to decompose at elevated temperatures and in concentrated alkali solutions [14, 31].

Chemical stability is important for ED processes because the electricity applied to the system would inevitably dissociate water molecules and generate proton and hydroxyl ions [32]. In specific ED applications, such as acid-base manufacturing, the pH change in the solution flow due to IEMs is significant. The chemical stability of IEMs to withstand harsh pH environments is important. In addition, the current density applied in most ED processes is near the limiting current density or even in the over-limiting range in order to achieve the highest possible reaction rate. The high electrical field in the membrane bulk exerts a relatively strong force onto fixed charges. It is thus crucial to have a high stability of fixed charge groups in the membrane bulk [33]. In the case of RED application, the dissociation of water is limited to a negligible extent on the electrodes, so that pH of the resin solution is expected to be stable. Feeding solutions (river and salt water) are close to neutral, and no significant process would alter or interfere with the pH throughout the residence time of the solution in each compartment. Consequently, the chemical stability of IEMs is not crucial in RED application [21, 34].

Membrane mechanical strength is necessary to prevent the flow of feed solutions from creating hydraulic pressure over the membrane in addition to the concentration gradient caused by osmotic pressure. However, in typical seawater/river water cases, the concentration difference is in the range of 0.01 M to 0.5 M (a bit over an order range). Some ED processing may encounter a gradient of several orders (e.g., deionization). The osmotic pressure exerted onto the membrane is quite different. On the other hand, the mechanical strength of the membrane is not as crucial in the RED system when compared with the PRO technique. In the latter case, membranes have to withstand tremendous hydraulic pressure given a water flux of 20-50 L m^{-2} h^{-1} [35].

The common practice of cross-linked membrane material is very helpful in strengthening, but crosslinking also tends to increase the membrane resistance [14, 33]. As will be discussed later, resistance of the membrane is more important, and it is unproductive to sacrifice the resistance in order to improve mechanical strength through crosslinking.

3.2.3. Swelling Degree, Ion Exchange Capacity, and Fixed Charge Density

The swelling degree (also known as water content) of the membrane is usually expressed as the water content or water uptake of the membrane under a given condition. The swelling degree is dependent on the nature of the membrane structure and material as well as the outer solution condition [21, 36]. IEC represents the number of fixed charges on the membrane in a unit of membrane dry weight. Most CEMs incorporate sulfonic acid ($–SO_3^{2-}$) or carboxylic acid groups ($-COO^-$) in the membrane structure, while ammonium groups ($–NR_3^+$, $–NH_4^+$, $–NH_2$, $=NH$, $\equiv N$) are common in AEMs. The type and distribution of these ion exchange groups classify different membranes. The ion exchange capacity (IEC) of ion exchange membranes (IEMs) are usually determined experimentally according to the titration method using a strong acid or base of HCl for CEMs and NaOH for AEMs, respectively.

Swelling is usually considered to be an adverse effect because it tends to decrease the permselectivity of ion exchange membranes, but it also decreases the membrane resistance in certain cases, especially for anion exchange membranes [9, 28, 37]. For applications such as RED, the loss of permselectivity may not be an adverse effect if a much lower resistance is achieved. For example, Geise *et al.* (2013) made AEMs based on poly (phenylene oxide) and poly (sulfone) polymers. High swelling degrees led to increase in conductivity of more than three orders of magnitude, while the permselectivity decreased by only 6% [28]. As will be discussed in the following section, a slight decrease of permselectivity on power output would compensate for a significantly lowered resistance in respect to power generation.

A high IEC indicates more ion exchange groups in the membrane bulk, but swelling tends to dilute the concentration of these groups as the distance between these ion exchange groups increases as the membrane is immersed in solution. Therefore, the ratio of IEC and swelling degree, termed as the fixed charge density (or fixed ion concentration), depicts the overall effects of the swelling degree on IEC and provides a direct relationship between the two electrochemical properties of an IEM [9, 38]. The fixed charge density (meq·g H_2O^{-1}) is defined in Eq. 2 if the IEC and water uptake of a membrane are known [9, 14, 39]:

$$FCD = \frac{IEC}{w_u} \tag{2}$$

where FCD is the fixed charge density, and w_u is the water uptake (dimensionless).

The advantage of using fixed charge density is easily seen when IEC and water content do not change simultaneously. For example, increased IEC is reported to result in higher permselectivity of IEMs [40]; however, the water content in the membrane phase may vary under different solution concentrations due to osmotic de-swelling and the decrease of free volume in the membrane phase [41]. As a result, the final membrane may exhibit lower permselectivity with the same IEC because its final fixed charge density is lower. This de-swelling effect on the membrane is more pronounced in AEMs than in CEMs [9, 24, 28, 41].

3.3. RED System Performance

The optimization of the RED system is crucial for potential large-scale applications. In order to effectively capture the salinity gradient as power, an RED stack with 20 to 50 cells may be necessary [42]. In this type of set-up, not only is the performance of the membrane influential, but other components, including feed solution compartments, electrodes, and spacers, have a significant effect. They all cause ionic resistance but to different degrees. As soon as the transport of ions through membranes begins, concentration polarization occurs and affects the overall resistance. The estimation and measurement of power output depends largely on the understanding of these processes and their effects. Furthermore, the successful development of this technology should not only include enhancement of the electrochemical properties of the stack but also optimize other factors, including spacer design, electrode requirements, pumping energy consumption, and pretreatment of the water, to reduce membrane fouling.

3.3.1. Internal resistance of the system

The resistance of an RED stack is the summation of resistances of all components in a series, including electrodes, electrolytes, diffusion boundary layers at the membrane surface, and membranes. Simplified models neglect the resistance of diffusion boundary layers or combine its contribution with membrane resistance and express the overall resistance (Ω) as follows [2, 43]:

$$R_{stack} = \frac{N}{A}\left(R_a + R_c + \frac{d_c}{\kappa_c} + \frac{d_d}{\kappa_d} \right) + R_{el} \tag{3}$$

where A is the effective membrane area (cm^2), R_a is the AEM resistance ($\Omega \cdot$cm^2), R_c is CEM the resistance ($\Omega \cdot$cm^2), R_{el} is the resistance (Ω) of electrodes, d_c is the thickness (cm) of the concentrated solution, d_d is the thickness of diluted solution, κ_c is the specific conductivity (mS$\cdot$cm^{-1}) of the concentrated solution, and κ_d is the specific conductivity (mS$\cdot$cm^{-1}) of the diluted solution. The presence of spacers will significantly lower the power output due to the loss of membrane area from non-conductive spacer blockage [9]. If the spacer shadow effect is considered as the portion of the membrane area masked by the spacer denoted as β, the resistance of the stack can be written as [6, 9]:

$$R_{stack} = \frac{N}{A}\left(\frac{R_a}{1-\beta} + \frac{R_c}{1-\beta} + \frac{d_c}{\kappa_c} + \frac{d_d}{\kappa_d} \right) + R_{el} \tag{4}$$

However, there is no consensus on the qualification of shadow effect β. An apparent shadow effect can be measured as the ratio of experimental power achieved using AC as W_{AC} (W) and the theoretical power achievable W_{theo} (W) as the following equation [12, 39]:

$$\beta = \left(1 - \frac{W_{AC}}{W_{theo}} \right) \times 100\% \tag{5}$$

W_{theo} is estimated based on the Nernst equation under the assumption of 100% permselectivity at a given salinity condition. The ratio of a theoretically calculated membrane area to an actual membrane area used in practice is also suggested [6, 32]. Then, the resistance of all different parts of a cell are multiplied with the exception of the electrodes [42]. The electrode resistance may be considered negligible if the stack is scaled with a large number of cells (e.g., larger than 20 cells) but with only two electrodes [4, 44].

A more comprehensive consideration of the stack resistance also includes the diffusion boundary layer and the salinity gradient resistance [45]. Considering all of these effects, the resistance of a RED stack (Ω) of N cells is expressed as:

$$R_{stack} = N\left(R_{ohmic} + R_{\Delta C} + R_{BL}\right) \tag{6}$$

where R_{ohmic} is the membrane resistance (Ω) attributed to ionic transport through the membranes, which is equal to the one cell resistance discussed above, $R_{\Delta C}$ is the resistance (Ω) attributed to the reduced electromotive forces as a consequence of the change in the concentration of the bulk solution, and R_{BL} is the boundary layer resistance (Ω) due to concentration polarization.

The $R_{\Delta C}$ considers the change of the solution concentration from the inlet to the outlet of the solution compartment. The result of this concentration gradient is the spatial difference of membrane potential. The resistance due to the concentration change in the bulk solution is expressed as:

$$R_{\Delta C} = \frac{V_{stack} - V_{average}}{JA} = \frac{\alpha RT}{FJA} \ln\left(\frac{1 + \dfrac{JL}{Fq_d c_d}}{1 - \dfrac{JL}{Fq_c c_c}}\right) \tag{7}$$

where J is the current density (A·m^{-2}), α is the average apparent permselectivity of the membrane (%), c_c is the concentration (mol·L^{-1}) of the concentrated salt solution, c_d is the concentration (mol·L^{-1}) of the diluted salt solution, q_c and q_d are the flow rate (m^3·s^{-1}) of the concentrated and diluted solutions, respectively, and L is the cell length (m). Thus, the stack resistance relates to the electricity current and the hydrodynamic environment in the system.

The summation of resistance from all components is an effective representation of the entire RED stack resistance; however, in real RED application, possible errors of resistance estimation, specifically in IEMs and solution compartments, may occur when the feed solution concentration is different from the concentration when the resistance measurement was taken. For example, the apparent resistance of IEMs in a stack is significantly higher than the value from the standard measurement (with 0.5 M NaCl solution) [10, 11, 15]. Thus, the effect of changing resistance must be clarified and modeled for improved representation of the RED stack.

One proposed explanation compares the membrane resistance with the resistance due to concentration polarization, which is adequate to account for its concentration dependency [9, 10]. This will be discussed in more detail in the next section. A decrease in resistance is reported when the solution flow rate increases. This supports the theory because the resistance due to concentration polarization can be largely avoided or eliminated altogether when the proper agitation of electrolytes is maintained by providing a sufficient flow [9, 10, 16, 18].

Several models have been proposed based on experimental data. For example, Veerman *et al.* (2009) [42] fitted experimental data to an exponential function in the form of:

$$R_m = A + B \cdot e^{-rC} \tag{8}$$

where *A*, *B*, and *r* are all fitting parameters, and C is the solution concentration.

Later, Kim *et al.* (2013) [46] pointed out that membrane resistance is a linear function of the reciprocal of solution concentration:

$$R_m \propto \frac{1}{C} \tag{9}$$

The most recent development on this topic proposed the modified relationship as [15]:

$$R_m = A + \frac{r}{C} \tag{10}$$

where *A* and *r* are constants to be fitted from experimental data. The last model fits well and partly explains the phenomena found by Guler *et al.* (2013) that when the membrane thickness approaches zero, the membrane resistance does not extrapolate to zero [39]. More efforts are needed to further explore the physical meanings behind these empirical models.

Finally, the resistance of feed solutions, particularly from the diluted solution, decreases as the compartment thickness decreases. The resistance of the fresh water compartment has significant weight [10, 42]. One obvious approach to decrease stack resistance would be to decrease the compartment thickness. If both compartments are decreased, the resistance can be significantly lowered, but the pumping energy is further increased at the same time [45]. Several designs of RED stacks using different thicknesses of spacers in concentrated and diluted compartments have been reported in literature as well [43, 47]. If the diluted compartment uses thinner spacers (i.e., shorter intermembrane distance) than concentrated compartments, the system resistance could effectively be reduced as well as require less pumping energy for the entire system [2, 47]; however, a stack with different compartment thicknesses may suffer bulging caused by the pressure difference [48]. Another approach to decrease the resistance from the dilute compartment is derived from the assumption that the conductivity of a solution increases with an increasing concentration. If the concentration within the dilute compartment is increased, the resistance will be lowered. This is exactly the approach taken to utilize brine water as a high concentration feed and brackish or seawater as a low concentration feed [49, 50]. In this case, the water resource is not as widely available as it is when using seawater and river water. In summary, research efforts should be focused on novel approaches to decrease the resistance of solution compartments while requiring moderate pumping energy consumption in order to optimize the system efficiency.

3.3.2. Concentration polarization

Concentration polarization arises essentially because of the different transport number of ions in the bulk solution and in the membrane phase. The transport number in the membrane phase for counter-ions is higher than in the solution phase. Consequently, the depletion of counter-ions at the membrane-solution interface surpasses the feed speed from the solution bulk. A concentration gradient gradually forms as the transport of ions (i.e., the passage of ionic current) continues as it also does in an ED stack [24, 51, 52].

The widely used DC method in the measurement of membrane resistance may include the contribution of DBL resistance due to concentration polarization because the method essentially determines the sum of the membrane resistances and the DBL resistance. Therefore, in a RED system, the stack resistance acquired experimentally under the standard condition (i.e., 0.5 M NaCl solution) often fails to predict accurate power output when there is a current flowing between electrodes, as discussed in the previous section. This deviation is more pronounced in the fresh water compartment [19, 38].

One approach in quantifying the concentration polarization follows the original study conducted in the ED field. The change in the resistance is usually considered as ohmic and non-ohmic parts, which are due to solution conductivity change and membrane potential change, respectively [53]. Brauns [49] assumed a linear concentration gradient from the bulk solution to the membrane-solution interface at a steady state. Then, the ohmic resistance that results from the change of solution concentration can be calculated using the average concentration at the DBL layer:

$$R_{ohmic} = \frac{\delta}{\left(\frac{c_b + c_i}{2}\right) \cdot \Lambda_b} \tag{11}$$

where c_b and c_i are the concentrations ($\text{mol}\cdot\text{L}^{-1}$) of the bulk solution and the solution at the interface, respectively, Λ_b is the molar conductivity ($\text{S}\cdot\text{m}^{-1}\cdot\text{mol}^{-1}$) of the bulk solution, and

δ is the thickness (m) of the boundary layer [49]. A more precise way to estimate the same resistance is by integrating along the DBL thickness [53]:

$$R_{ohmic} = \frac{1}{\Lambda_b} \int_0^{\delta} \left(\frac{1}{c(x)} - \frac{1}{c_b} \right) dx \tag{12}$$

where $c(x)$ is the concentration of solution at a certain point within the boundary layer. The concentration at the membrane-solution interface c_i is estimated with respect to the limiting current density i_l (A·m^{-2}) as [16]:

$$c_i = c_b \cdot (1 - \frac{i}{i_l}) \tag{13}$$

where i is the current density (A·m^{-2}) in the system. It is important to note that even though the operating condition of RED has a current density far below the limiting current, the concept of the limiting current is still important for the estimation of DBL thickness and DBL resistance. The key parameters, such as the limiting current density and the thickness of DBL, can be determined using techniques such as chronopotentiometry and EIS, as discussed in Section 3.2.1. For the non-ohmic resistance due to membrane potential change, the same techniques are also applicable, and are widely used in the study of non-ohmic resistance due to concentration polarization [13, 15, 45, 54].

The situation becomes more complicated when the flow of water in the cell compartments affects the hydrodynamic environment of the DBL, which also affects the thickness and concentration at the solution-membrane interface. For example, Vermaas *et* *al.* (2012) developed a model assuming that the boundary layer resistance is proportional to the velocity shear at the membrane-solution interface [55]. The R_{DBL} is:

$$R_{DBL} \propto \frac{h}{v_{average}} = t_{res}\frac{h}{L} \tag{14}$$

where $v_{average}$ is the average velocity ($\mathrm{m \cdot s^{-1}}$), t_{res} is the residence time (s), L is the cell length (m), and h is the cell thickness (m). When the flow distribution within the solution compartment is considered, Eq. 13 can only estimate the DBL on an average basis [56]. Furthermore, the slight dependence of DBL resistance on current density is not considered in this hydraulic relationship; however, in the classical ED theory, the effect of current density on resistance is well-quantified, as seen in Eq. 13 [53]. Recently, researchers have taken these processes into account and provided more accurate simulations on system resistance and power generation [57, 58].

3.3.3. Power output

The theoretical salinity gradient power generation in an RED system with many cells has long been reported based on Kirchhoff's law and based on the fact that the potential generated from different cells is additive [45]. The stack of N membrane pairs generates an open-circuit potential of V_{stack} (Volt), which can be calculated as:

$$V_{stack} = 2N\frac{\alpha RT}{F}\ln\left(\frac{a_c}{a_d}\right) \tag{15}$$

where N is the number of stacks, R is the gas constant (J·mol^{-1}·K^{-1}), T is the absolute temperature (K), F is the Faraday constant (C mol^{-1}), α is the average apparent permselectivity of the membrane (%), a_c is the activity (mol·L^{-1}) of the concentrated salt solution, and a_d is the activity (mol·L^{-1}) of the diluted salt solution.

According to Kirchhoff's law, the power output (W) of the RED stacks is calculated as:

$$W = I^2 R_L = \frac{V_{stack}^2 R_L}{\left(R_{stack} + R_L\right)^2} \tag{16}$$

The power output is a function of overall stack resistance R_{stack} (Ω) and external load resistance R_L (Ω), so the output power, W (W), is maximized when R_{stack} and R_L are equal [2, 43], written as:

$$W_{\max} = \frac{V_{stack}^2}{4R_{stack}} \tag{17}$$

If the power density is defined as power output per unit membrane area, the maximum power density $P_{\max}$ (W·m^{-2}) is then calculated as:

$$P_{\max} = \frac{V_{stack}^2}{4AR_{stack}} \tag{18}$$

where A is the membrane area (m^2).

If the loss of energy from pumping water through the system is considered, the net energy density (P_{net}) can be estimated using the following equations [59]:

$$P_{pump} = \Delta P_c Q_c + \Delta P_d Q_d \tag{19}$$

$$P_{net} = P_{\max} - P_{pump} \tag{20}$$

where P_{pump} is the power density decrease due to hydrodynamic losses ($W \cdot m^{-2}$), ΔP_c and ΔP_d are pressure drops (Pa) over the concentrated and diluted compartments, respectively, and Q_c and Q_d are flow rates ($m^3 \cdot s^{-1}$) in concentrated and diluted compartments, respectively.

P_{net} is a better indicator of the efficiency of the RED system because it takes both energy gains and losses into account. It should also be considered that the power output cannot be maintained at the maximum value in real practice of the RED system because P_{max} is based on the largest concentration difference of the solutions on both sides at the beginning of the process. Inevitably, the concentration difference would decrease as well as the power output.

It should be noted that the gross power density reported in the literature could be obtained from theoretical calculation based on Eq. 18 or measured experimentally [9, 34, 42, 45]. Generally, the experimental power density using the chronopotentiometry or the galvanostatic method is lower than the calculated value [9, 39, 60]. This is another piece of evidence that the electrochemical property of the entire stack is not ideal and that effects such as concentration polarization are severely detrimental.

In addition, there are ions other than sodium (Na^+) and chloride (Cl^-) ions in seawater and river water. Multivalent ions, such as magnesium (Mg^{2+}) and sulfate (SO_4^{2-}) ions, also exist at a relatively lower concentration than salt. Post *et al*. (2009) identified the potential detrimental effects of multivalent ions. A multivalent ion concentration of 0.05 M in a concentrated solution and 2 mM in a diluted solution (base NaCl solution of 0.45 M and 3 mM, respectively) decreases the stack voltage and increases the stack resistance [61]. Their effects may also be important to the total efficiency of RED power generation. Hong *et al*. (2013, 2014) reported the modeling result to be a 15-43% decrease of power density in a system using simulated saline water as electrolytes flowing through RED stacks [62, 63]. Vermaas *et al*. (2014) also conducted experiments on RED stacks and used a mixture of 10% $MgSO_4$ and 90% NaCl (molar ratio). The resulting power density decreased by 29-50%, depending on the different IEM pairs tested [64].

3.4. Membrane Performance in RED

Because the RED system is the reverse process of electrodialysis (ED), many IEMs available on the market designed for ED have been investigated for their performance in the RED system. Only a brief collection of the most common commercial membranes is shown in Table 2, which is based on their reported applications in RED systems [9, 39]. Apparent desired properties, such as permselectivity and ionic resistance, are listed in Table 2 along with other important characteristics. The performance of different membrane pairs in specific stacks from the literature is summarized in Table 3. Other related information on stack design and operational parameters are also included.

Generally, more homogeneous membranes are commercially available than heterogeneous ones. For both commercial and tailor-made CEMs, sulfonated groups are universally used as ionogenic groups. Ionogenic groups used in AEMs are more diverse. The thicknesses of these membranes are mostly in the range of 100-200 μm because of limitations in terms of stack thickness and consideration of overall internal resistance of RED cells. For permselectivities, AEMs are less selective than CEMs in general. The permselectivity of AEMs range from 80-90%, whereas the CEMs are mostly above 95%.

Table 3 shows the highest power density reported from experimental data as 2.2 W m^{-2} using commercial membrane pairs (FAS and FKS) [45]. The use of thin spacers (100 μm) is a significant improvement. The effort to enhance IEM performance also results in high power density. The highest power densities of 1.3 W m^{-2} were achieved using custom-made or a mix of custom-made and commercial membranes (SPEEK, PECH, 0.7 wt% Fe_2O_3-SO_4^{2-} SPPO) in all cases [39, 65, 66]. A comparison that includes information from Tables 2 and 3 reveals that low resistance ($< 1.0\ \Omega\cdot cm^2$) is the key property, which is enhanced by specific design and custom-made membranes. On the other hand, the permselectivity is not significantly scarified (86.5-87.7%) because the low permselectivity of custom-made membranes is compensated for by very high permselectivity of the other membranes in a pair (ASV: 97%; CMX: 99%). For a pair consisting of both commercial membranes, those with a relatively low resistance (FKD/FAD and FKS/FAS) also resulted in better performance. One exception is the pair (CMV/AMV) that has a relatively high resistance and a mediocre permselectivity and still gives a high power density of 1.11 W m^{-2}. In general, this is in agreement with the discussion in Chapter 2 and the result of simulation work which determined that low resistance and well-balanced permselectivity are most important in membrane performance [67].

Stack design also affects overall performance when comparing the same pair of membranes used under different stack parameters; however, its effect is limited when thin spacers or higher flow rates are applied. Consequently, the improvement of membrane properties would be one of the main breakthroughs for the development of a successful RED application.

Table 1 – Summary of membrane properties of some commercially available IEMs

MEMBRANE PRODUCT	IEC (meq g_{dry}^{-1})	Permselectivity (%) [a]	Resistance ($\Omega\ cm^2$) [b]	Swelling degree (%)	Thickness (μm)	Ionogenic groups	Ref.
Cation Ion Exchange Membranes							
Homogeneous							
Fumasep® FKD	1.14	89.5	2.14	29	113	$-SO_3^{2-}$	[12]
Fumasep® FKS	1.54	94.2	1.5	13.5	40	-	[39]
Qianqiu CEM	1.21	82.0	1.97	33.0	205	-	[39]
Neosepta® CMX	1.62	99.0	2.91	18	164	$-SO_3^{2-}$	[9]
Neosepta® CMX	1.5-1.8	97	1.8-3.8	25-30	140-200	$-SO_3^{2-}$	[21]
Selemion® CMV	2.0-2.4	95.0-98.8	2.3-2.9	20-25	101-150	$-SO_3^{2-}$	[9, 21]
0.7wt% Fe_2O_3-SO_4^{2-} SPPO	1.40	87.7	0.97	26	100	$-SO_3^{2-}$	[65]
SPEEK 40	1.23	95.3	2.05	23	53	$-SO_3^{2-}$	[39]
SPEEK 65	1.76	89.1	1.22	35.6	72	$-SO_3^{2-}$	[39]
JJC-82		99.6	3.1				[68]
Heterogeneous							
Ralex® CMH-PES	2.34	94.7	11.33	31	764	$-SO_3^{2-}$	[9]
Anion Exchange Membranes							
Homogeneous							
Fumasep® FAD	1.42	86.0	0.89	34	74	-	[9]; [39]
Neosepta® ACS	1.4-2.0	-	2.0-2.5	20-30	150-200	$-N(CH_3)_3^+$	[69]
Neosepta® AMV	1.78-1.9	87.3	3.15	17.0	120-124	-	[21]; [39]
Neosepta® AMX	1.4-1.7	90.7	2.0-3.5	25-30	120-180	$-N(CH_3)_3^+$	[69, 70]
Selemion® ASV		97	3.7		120		[c]
Fumasep® FAS	1.12	89.4	1.03	8.0	33	-	[39]

Table 1 (continued)

Qianqiu AEM	1.33	86.3	2.85	35.0	294	-	[39]
PECH A	1.31	90.3	2.05	32.2	77	–NR3+	[34]
PECH B-1	1.68	86.5	0.82	49	33	–NR3+	[34]
PECH B-2	1.68	87.2	0.94	49	77	–NR3+	[34]
PECH B-3	1.68	87.0	1.32	49.1	130	–NR3+	[34]
PECH C	1.88	79.2	1.14	53.5	77	–NR3+	[34]
Heterogeneous							
JJA-72		99	3.0				[68]
Ralex® AMH-PES	1.97	89.3	7.66	56	714	-	[9]

a. Measured over the membrane between a 0.5 M and a 0.1 M solution

b. Measured in 0.5 M NaCl solution at 25°C

c. From manufacturer

Table 2 – Maximum power density from RED systems reported in the literature

Manufacture /Tailor made	CEM	AEM	Spacer type/thickness	Unit membrane area	Cell no.	Linear flow velocity	Concentration gradient	Gross Power density ($W \cdot m^{-2}$)†	Ref.
-	Polyethylene mixed with crosslinked polystyrene resins		Nonconductive spacer 1000 µm	8 cm^2	47	-	tap water/0.5M NaCl	0.20 (39°C)	[1]
Ionics	61CZL	103QZL	Turbulence promoter 1000 µm	232 cm^2	30	15 $cm \cdot s^{-1}$	0.0259/0.57 M NaCl		[2]
Rhone-Poulenc	CRP	ARP	Nonconductive 3000 µm	40 cm^2	5	-	0.017/5.03 M NaCl	0.41	[71]
Asahi	CMV	AMV	Nonconductive 3000 µm	40 cm^2	5	-	0.017/5.03 M NaCl	0.4	[71]
MEGA	CMH-PES	AMH-PES	Nonconductive 200 µm	100 cm^2	5	1.7 $cm \cdot s^{-1}$	0.017/0.513 M NaCl	0.6	[39]
MEGA	CMH-PES	AMH-PES	Nonconductive 250 µm	100 cm^2	5	17 $cm \cdot s^{-1}$	0.017/0.508 M NaCl	0.65	[54]
Modified Commercial Polyethylene	JJC-82	JJA-72	Polyethylene spacer 550 µm	100 cm^2	30	0.21 $cm \cdot s^{-1}$	0.008/0.561 M NaCl	0.41	[68]
Modified Commercial Polyethylene	JJC-82	JJA-72	Polyethylene spacer 550 µm	100 cm^2	30	0.21 $cm \cdot s^{-1}$	0.017/0.556 M NaCl	0.388	[68]
Modified Commercial Polyethylene	JJC-82	JJA-72	Polyethylene spacer 550 µm	100 cm^2	30	0.21 $cm \cdot s^{-1}$	0.55/5.32 M NaCl	0.573	[68]

Table 2 (continued)

ACIPLEX	K-502	A-201	1 mm spacer for dilute; 10 mm spacer for salt	80 cm^2	29	1.9 cm·s^{-1} for dilute; 0.075 cm·s^{-1} for saline*	0.0017/0.598 M NaCl	0.26	[47]
Fumatech	FKS	FAS	Nonconductive 200 µm	100 cm^2	5	1.7 cm·s^{-1}	0.017/0.513 M NaCl	1.11	[39]
Fumatech	FKS	FAS	Nonconductive 100 µm	100 cm^2	5	4 cm·s^{-1*}	0.017/0.507 M NaCl	2.2	[45]
Custom-made	SPEEK40	PECH B2	Nonconductive 200 µm	100 cm^2	5	1.7 cm·s^{-1}	0.017/0.513 M NaCl	1.18	[39]
Custom-made	SPEEK 65	PECH B2	Nonconductive 200 µm	100 cm^2	5	1.7 cm·s^{-1}	0.017/0.513 M NaCl	1.28	[39]
Tokuyama/Custom-made	CMX	PECH B3	Nonconductive 200 µm	100 cm^2	5	1.7 cm·s^{-1}	0.017/0.513 M NaCl	1.07	[39]
Custom-made/Tokuyama	SPEEK40	AMX	Nonconductive 200 µm	100 cm^2	5	1.7 cm·s^{-1}	0.017/0.513 M NaCl	0.98	[39]
Tokuyama/Custom-made	CMX	PECH B2	Nonconductive 200 µm	100 cm^2	5	1.7 cm·s^{-1}	0.017/0.513 M NaCl	1.18	[39]
Qianqiu	Qianqiu CEM	Qianqiu AEM	Nonconductive 200 µm	100 cm^2	5	1.7 cm·s^{-1}	0.017/0.513 M NaCl	0.83	[39]
Custom-made/Tokuyama	SPEEK65	AMX	Nonconductive 200 µm	100 cm^2	5	1.7 cm·s^{-1}	0.017/0.513 M NaCl	1.1	[39]
Tokuyama/Custom-made	CMX	PECH B1	Nonconductive 200 µm	100 cm^2	5	1.7 cm·s^{-1}	0.017/0.513 M NaCl	1.27	[39]
Tokuyama/Custom-made	CMX	PECH A	Nonconductive 200 µm	100 cm^2	5	1.7 cm·s^{-1}	0.017/0.513 M NaCl	1.08	[39]

Table 2 (continued)

Tokuyama/ Custom-made	CMX	PECH C	Nonconductive 200 µm	100 cm^2	5	1.7 cm·s^{-1}	0.017/0.513 M NaCl	1.15	[39]
Asahi Glass	CMV	AMV	Nonconductive 200 µm	100 cm^2	5	1.7 cm·s^{-1}	0.017/0.513 M NaCl	1.13	[39]
Tokuyama	CMX	AMX	Nonconductive 200 µm	100 cm^2	5	1.7 cm·s^{-1}	0.017/0.513 M NaCl	1.07	[39]
Fumatech	FKD	FAD	Nonconductive 200 µm	100 cm^2	5	1.7 cm·s^{-1}	0.017/0.513 M NaCl	1.19	[39]
Fumatech	FKD	FAD	Nonconductive 200 µm	100 cm^2	25	1.16 cm·s^{-1*}	0.017/0.51 M NaCl	1.17	[60]
Fumatech	FKD	FAD	Nonconductive spacer 200 µm	100 cm^2	50	6.7 cm·s^{-1*}	0.017/0.513 M NaCl	0.93	[60]
Fumatech	FKD	FAD	Nonconductive 200 µm	100 cm^2	50	0.58 cm·s^{-1*}	0.017/0.51 M NaCl	0.95	[25]
Custom-made	Profiled CMH-PES	Profiled AMH-PES	Profiled IEMs serves as spacers 230 µm	100 cm^2	6	21 cm·s^{-1}	0.017/0.508 M NaCl	1.0	[54]
Tokuyama/ Custom-made	CMX	PECH (Pillar structure)	Nonconductive in concentrated compartment 100 µm; AEM serves as spacers in dilute compartment 100 µm	100 cm^2	2	6.7 cm·s^{-1*}	0.017/0.507 M NaCl	1.3	[66]
Tokuyama/ Custom-made	CMX	PECH (Wave structure)	Nonconductive in concentrated compartment 100 µm; AEM serves as spacers 100um	100 cm^2	2	6.7 cm·s^{-1*}	0.017/0.507 M NaCl	1.3	[66]

Table 2 (continued)

Tokuyama/ Custom-made	CMX	PECH (Ridge structure)	Nonconductive in concentrated compartment 100 µm; AEM serves as spacers 100um	100 cm^2	2	6.7 cm·s^{-1*}	0.017/0.507 M NaCl	1.1	[66]
Tokuyama/ Custom-made	CMX	PECH (Flat)	Nonconductive 100 µm	100 cm^2	2	6.7 cm·s^{-1*}	0.017/0.507 M NaCl	0.9	[66]
Tokuyama	CMX	AMX	Nonconductive 190 µm	42 cm^2	10	0.54 cm·s^{-1}	0.0096/0.605M NaCl	0.46	[48]
Tokuyama	CMX	AMX	Ion conductive spacer 320 µm	100 cm^2	3	0.83 cm·s^{-1}	0.017/0.5 M NaCl	0.8	[72]
Tokuyama	CMX	AMX	Nonconductive spacer 320 µm	100 cm^2	3	0.83 cm·s^{-1}	0.017/0.5 M NaCl	0.27	[72]
Neosepta	CMX	AMX	Nonconductive 200 µm	100 cm^2	25	1.16 cm·s^{-1*}	0.017/0.51 M NaCl	0.65	[60]
Asahi Glass	CMV	AMV	Nonconductive 200 µm	100 cm^2	25	1.16 cm·s^{-1*}	0.017/0.51 M NaCl	1.18	[60]
Neosepta	CMS	ACS	Nonconductive 200 µm	100 cm^2	25	1.16 cm·s^{-1*}	0.017/0.51 M NaCl	0.60	[60]
Qianqiu	Qianqiu CEM	Qianqiu AEM	Nonconductive 200 µm	75 cm^2	25	2.7 cm·s^{-1}	0.017/0.51 M NaCl	0.82	[59]
Qianqiu	Qianqiu CEM	Qianqiu AEM	Nonconductive 200 µm	100 cm^2	25	1.16 cm·s^{-1*}	0.017/0.51 M NaCl	1.05	[60]
Custom-made/ Selemion	0.7 wt% Fe_2O_3-SO_4^{2-}-SPPO	ASV	Nonconductive 250 µm	36 cm^2	3	6.7 cm·s^{-1}	0.017/0.51 M NaCl	1.3	[65]

* Calculated based on information provided
† Listed the highest gross power density achieved only

3.5. Current Stack/System Design

3.5.1. Ion conductive spacers

Theoretical power output and process efficiency are often affected by the concentration polarization and the spacer shadow effect. Concentration polarization is due to different transport numbers of the ions in the solution and in the membrane, which results in the depletion and the accumulation of ions at the membrane surface [32]. This phenomenon can be treated by optimizing the hydrodynamics in a RED stack [42, 72]; however, the spacer shadow effect occurring in RED is mostly due to the spacer materials caused by commercially available non-conductive spacers in the RED stack. This effect hinders ion transport from the solution phase to the membrane. The use of ion conductive material for RED spacers is often considered to reduce the shadow effect, allowing more available area for ion transport. Dlugolecki *et al*. [72] used ion conductive spacers to obtain a significant reduction of the spacer shadow effect. The elimination of the shadow effect led to a large reduction in stack resistance and an increase in power density. Furthermore, such optimization efforts on spacer design (e.g., use of ion conductive spacer) not only contributes to stack resistance reduction but may also help to reduce the effect of polarization [72, 73]. Nevertheless, considering that concentration polarization still plays a significant role in overall stack resistance, further efforts to optimize the hydrodynamics and stack design are still required to lessen the concentration polarization effect on power output. Greater energy production with low stack resistance depends on an effective stack design that consists of uniquely tailored spacers and IEMs for RED application.

3.5.2. Electrochemical couples for RED

The electrode system is one of the key components of the RED set-up. In the electrode system, electron transfer reactions allow the transformation of the charge carrier from an ion to an electron and then to a current. Only a few published works have reported an experimental investigation on the electrode material-redox couple system under RED operating conditions. However, Scialdone *et al*. [74] listed the following considerations for properly selecting suitable electrode systems: low voltage drops at the electrode-solution interface, the low cost of redox species and electrodes, the high solubility of the redox couple, the chemical and electrochemical stability of redox species, and the physical and chemical stability of electrodes. This discussion cannot encompass on all criteria in practice; however, an Fe(III) – Fe(II) couple warrants coverage. Serial electrolyte combinations, such as $FeCl_3/FeCl_2$, $[Fe(CN)_6]^{3-}/[Fe(CN)_6]^{4-}$ and Fe(III)-EDTA/Fe(II)-EDTA have been investigated [44, 74] and were found to be unstable under the investigated conditions. $[Fe(CN)_6]^{3-}/[Fe(CN)_6]^{4-}$ proved to be more effective in the absence of light and oxygen by combining with high redox couple concentrations and low current densities at both compact graphite and DSA electrodes. Success using $FeCl_3/FeCl_2$ lies in its stability, which remains constant at acidic pH for long durations at compact graphite electrodes [74]. Despite this success, more research on electrode systems with an RED application are needed to investigate feasible candidates for bench and large-scale stacks with an emphasis on safety, health, technical feasibility, and economics for real application.

3.5.3. Hybrid Processes Including RED

Various technologies and processes are being combined to explore synergistic approaches. The hybrid process of RED can maximize productivity and allow for various applications of technologies at a lower capital cost. In this section, various RED-based hybrid processes and their characteristics are reviewed to show trends in the application of hybrid RED processes.

Reverse osmosis (RO) is one frequently used technique for seawater desalination. In spite of its wide use, RO is still unsatisfactory because of its energy-intensive process. The hybrid process of RO and RED has complementary advantages over stand-alone RO or RED processes. The concentrated brine discharged from the RO process can be fed back to the RED system as concentrated salt water. This brine feed allows for a greater concentration gradient, which enhances the power generation and conversion efficiency of RED [75]. Diluted effluent water from the RED system can be used as a pretreated feed solution for the RO unit, which reduces the energy consumption in the system. This synergistic effect makes RO and RED an ideal combination for effective desalination and brine management with less energy consumption, which provides great advantages over the conventional RO processes [75].

Bioelectrochemical-based systems (BESs) can also be combined with RED to create another form of hybrid technology. BES technologies, such as the microbial fuel cell (MFC), use microorganisms at the bioelectrode (anode) to catalyze the oxidation reaction [76]. BESs help to reduce overpotentials for diverse electrochemical reactions, which also allows for the capture of energy from waste biomass as electricity or biofuels [77, 78]. Considering the fact that large electrode overpotential is one of the limiting factors in RED practice (which leads to up to 50% loss in efficiency [44]), combining RED with BESs can be beneficial for effective operation. Kim and Logan (2011) first proposed a microbial reverse electrodialysis cell (MRC), which contains the RED cell pairs in between MFC electrodes [76]. MRC exhibited three times the voltage (1.2 V) and 6.1 times the power density (4.3 $W \cdot m^{-2}$) compared with that of a stand-alone MFC [76, 79]. (Note that in this work the power density of MRC is expressed in $W \cdot m^{-2}$ of electrode). In addition, MRC also showed great potential in harvesting hydrogen gas by using ammonium bicarbonate salts, which are known to be regenerated by heating. Nam *et al*. [80] demonstrated a system for the production of hydrogen gas based on the concept of salt recovery being used as low-grade waste heat source, which is readily available in wastewater treatment plants. This allows for the use of a high salt solution in an RED system for electricity generation as well as hydrogen gas production in MRC.

In the early development stages of advanced RED application, hybrid processes of RED offered more opportunities for novel approaches to overcome the limitations of individual systems. More systematic experimental studies should be carried out to validate these RED hybrid processes based on current theoretical findings. The benefits to be obtained from hybrid processes of RED provide great opportunities for further innovation.

3.6. Summary

Although the advantages of harvesting energy using the salinity gradient from seawater and river water are well understood, a wide application of salinity gradient energy is still hurtled by system performance and material development. On one hand, major improvement can be achieved by improving stack conductance, either altering hydrodynamic environment to tackle the concentration polarization or decreasing ion transport distance. On the other hand, developing more conductive key components, such as IEMs and electrode materials based on fundamental understanding of ion transport and electrochemistry are also a promising approach. Specifically, for the RED process, the preparation of IEMs and understanding the properties and factors that determine the performance are the most crucial. With a review of literature, the key physicochemical and electrochemical properties of the ideal RED membranes are discussed as well as important performance-determining RED phenomena using experimentally obtained characteristics and theoretical RED models.

CHAPTER 4. ENHANCED IONIC CONDUCTIVITY AND POWER GENERATION USING ION EXCHANGE RESIN BEADS IN A REVERSE ELECTRODIALYSIS STACK

4.1. Abstract

In this chapter, I present an effective improvement in RED energy production by mitigating ionic conductivity limitations in dilute compartments. Specifically, ion exchange resin beads (IERBs) replaced non-conductive spacer fabrics in RED compartments with dilute NaCl solution in a modified stack containing fumasep® FKS and fumasep® FAS membranes. I compared the conductivity of an IERB packed bed and an inert glass bead-packed bed as a control to confirm IERB's effectiveness. When applied in RED, IERB decreased the stack resistance by up to 40%. The maximum gross power density improved by 83% in the RED stack compared to a regular RED stack at 1.3 $\text{cm}\cdot\text{s}^{-1}$ average linear flow velocity. IERB-filled stack resistance was modeled. The model results fit well with experimental data thereby confirming the effectiveness of the new approach presented here. Net power density is also estimated based on the measured pressure drop and pumping energy model. Both gross and net power density was improved by over 75% at higher flow rate. A net power density of 0.44 $\text{W}\cdot\text{m}^{-2}$ was achieved at a cell thickness of 500 μm. To the best of our knowledge, this research is the first to study the impact of IERB on power generation and establishes a new approach to improving power performance of RED systems.

4.2. Introduction

Extensive research has been conducted on the topic of salinity gradient power generation [4, 9, 43, 49, 55, 59, 65, 81-83]. The principles and performance of two different techniques harvesting salinity gradient, RED and PRO, have been in previous Chapters. I must overcome several challenges before initiating a large-scale application of RED technique. One of the major hurdles is a limited power output of the technique determined by stack resistance and membrane permselectivity. A lot of work has been conducted on improving the efficiency of RED power output by decreasing intermembrane thickness or using high performance custom made ion exchange membranes, ion-conductive spacers, and a corrugated membrane surface structure [34, 45, 54, 65, 72, 81]. These efforts aim to increase the ionic conductivity of the RED stack and the permselectivity of ion exchange membranes. However, these conventional methods have their limitations. For example, shortening intermembrane distance decreases ohmic resistance but increases pumping energy consumption. The net power density (gross power density subtracted by pumping energy requirement) is actually lowered when the intermembrane distance is lower than an optimal value in a specific RED system [45]. The performance of ion exchange membranes has improved significantly over the past few years, and several custom-made RED membranes have been synthesized [34, 65, 66]. However, improved membrane conductivity may counterbalance the membrane permselectivity. Cost-effective membranes with both high permselectivity and high conductivity is still a challenge [34, 65].

Many studies have illustrated that when the compartment thickness is over 200 µm, the ionic conductivity of the RED system is largely caused by the dilute compartments because of the low concentration of ions [2, 5, 7, 25, 43, 45]. Increasing the solution concentration in the dilute compartments would improve the conductivity. However, based on the Nernst equation, a brine solution of much higher concentration would be necessary to keep the stack potential on the same level, while high ion strength is detrimental to membrane performance in general [82, 84]. On the other hand, improved conductivity of feed solution is beneficial to power performance; therefore, RED system using brine water from specific sources, e.g. desalination plants, shows great potential in application [82, 85, 86]. A direct decrease of ionic resistance in the dilute compartment is nevertheless possible at a given concentration of fresh water (e.g. 0.017 M). Analogous electrodialysis systems, i.e., in the continuous electrodeionization (CEDI), desalination, and acid production processes, have applied ion exchange resin beads (IERB) to facilitate the ion transport through low concentration compartments [87-92]. The accumulation of counterions on the surface of these resin beads increases the local concentration of these ions. Overall transport of ions from one ion exchange membrane to the neighboring ion exchange membrane becomes easier in the dilute compartment through connections between these resin beads. Consequently, ionic conductivity is improved [93, 94].

To prove if the same concept can be applicable in RED stacks. I apply IERB in a RED stack. The application of IERB avoids complex membrane manufacturing procedures and can potentially maintain comparable power output at larger intermembrane distances. The current study, therefore, establishes a new approach to improving the power output of a RED system.

4.3. Materials and Methods

4.3.1. RED Stack Setup

Fumatehch electrodialysis stack (Module FT-ED40) was established in a laboratory environment. Two endplates made of polypropylene held 5½ pairs of commercial ion exchange membranes, FAS and FKS membranes (fumasep®, Fumatech, Germany), in all experiments (Figure 1). Considering the IERB load, the spacer thickness was chosen to be 500 µm as relatively thicker when compared to the state-of-the-art RED stack designs.[45, 54] The spacer (fumatech, PVC/polyester) is nonconductive with an overall dimension of 6 cm × 13 cm. The effective part of the woven fabric (polyester) on the spacer has a porosity of 60% and an area of 4 cm × 9 cm. The fabric part (polyester woven mesh structure) of the spacer was modified to accommodate resin beads with an opening (without polyester fabric) of 4 cm × 6 cm, and fabric at the inlets and outlets was maintained to prevent the washing out of resin beads (Figure 30 in Appendix A.3). Titanium mesh coated with Iridium plasma was used at both ends as an anode and cathode.

Analytical grade NaCl (Aldrich) and deionized water were used to prepare salt solutions. The NaCl solution was made at a concentration of 0.50 M as the concentrated solution and 0.017 M as the dilute solution. The rinse solution consisted of 0.25 M NaCl, 0.05 M $K_4Fe(CN)_6$, and 0.05 M $K_3Fe(CN)_6$. The NaCl solution was delivered by Masterflex® peristaltic pumps (Cole-Parmer, USA) with varying flow rates at 38 $mL \cdot min^{-1}$, 104 $mL \cdot min^{-1}$ and 190 $mL \cdot min^{-1}$. The corresponding linear flow velocity was calculated based on the cross-section area perpendicular to the flow direction assuming a uniform flow pattern within a compartment.

4.3.2. Ion Exchange Resin and Glass Beads

I used ion exchange resin (Sigma-Aldrich) in the bead form with a mesh size of 50-100. The size was determined to be suitable for this study because an IERB smaller than mesh 100 can be easily washed out through openings between spacer fabric and membrane surface. Key properties of resin beads have been listed in Table 3 and additional property information and characterizing methods are available in the Appendix A. Before usage, IERBs were equilibrium within 0.5 M NaCl solution for at least 24 h. Immediately before loading, IERBs were rinsed with deionized water and wiped out of extra water content on the surface using paper towel. Then, equally weighed cation exchange and anion exchange resin were mixed thoroughly and loaded into the dilute compartments by dispersing equal amount (by weight) of resin beads on ion exchange membranes facing a dilute compartment. Six grams of IERB per stack were applied evenly into five dilute compartments (1.2 g IERB each) to form a compact and homogeneous layer between membranes. The load amount was estimated based on the density of the mixture and occupiable space in a modified compartment. Similar size (mesh 50-100) glass beads (Sigma) were also used for comparison. Due to a higher density of glass beads, 14 g of glass beads was loaded into a stack (2.8 g for each compartment).

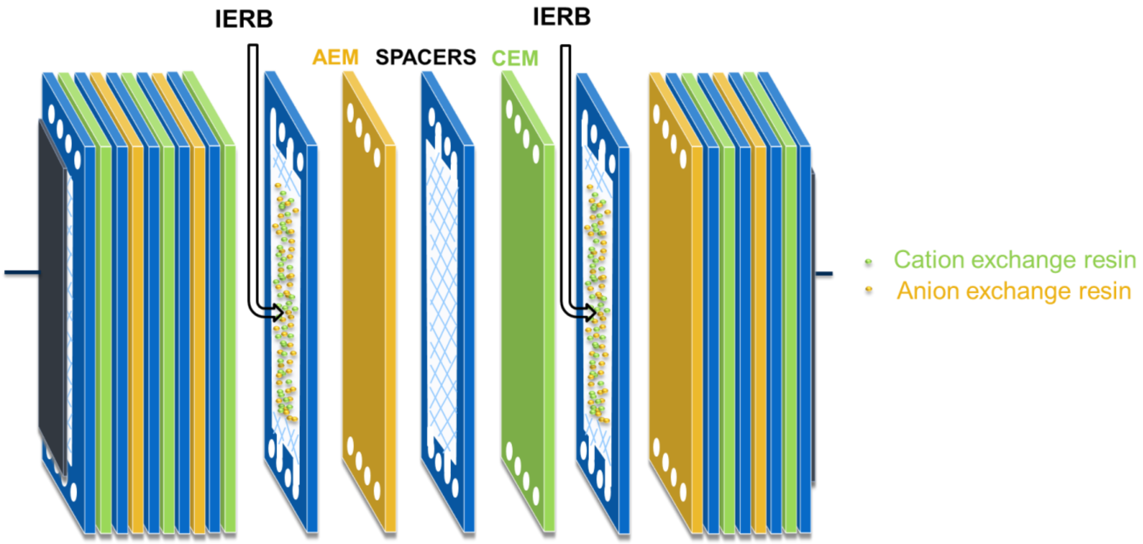

Figure 2 – The setup of the RED stack with five and a half cells. The IERB was loaded in the dilute compartments within the modified spacers. Schematic is not to scale.

\

Table 3 – Characteristics of IERB and inert glass beads

Mesh	Diameter (mm)	Type	Moisture[a]	Void ratio[b]		True density[b] ($g \cdot mL^{-1}$)
50-100	0.15-0.30	Dowex 50WX8-100	53%	0.317	0.401 (mixture)	1.10
50-100	0.15-0.30	Dowex 1X8-100	46%	0.389		1.07
50-70	0.21-0.30	G9143	-	0.390 (mixture)		2.4
70-100	0.15-0.21	G9018	-			2.4

a. Provided by manufacturer

b. Methods provided in Appendix A.1

Table 4 – Characteristics of commercial membranes

	Resistance[a] (Ω cm^2)		**Selectivity[b] (%)**	**Thickness[c] (μm)**
	Without concentration difference	With concentration difference		
FKS	1.30 ± 0.07	8.0 ± 0.28	98.3	30-37
FAS	1.19 ± 0.05	11.25 ± 1.3	94.6	30-37

a. Methods provided in the Supporing Information

b. Determined as the potential over 0.1 / 0.5 M NaCl

c. Provided by manufacturer

4.3.3. Ion Exchange Membranes

I employed the fumasep® ion exchange membranes as representative membranes for the study in our RED stack. FKS membrane served as the cation exchange membrane and FAS served as the anion exchange membrane. Several key properties of these two membranes have been listed in Table 4. I reported membrane resistance in two different measurements, one without concentration difference as the conventional method (with 0.5 M NaCl solution on both sides of the membrane), and the other with concentration difference (with 0.017 M NaCl solution on one side and 0.5 M NaCl solution on the other side). These measured values are listed in Table 4 (see also Appendix A.1 for more detail).

4.3.4. IERB and Inert Glass Beads Conductivity

Electrical conductivity measurements were conducted with a four-electrode connection using an Ivium potentiostat (Vortex®, Ivium Technologies, The Netherlands) at room temperature (21 ± 1°C). Two titanium mesh electrodes served as working and counter electrodes at both ends of the stack, while two silver wires (GF02315247, 99.99%, Aldrich) were used as reference and sense electrodes placed at end compartments between the two titanium mesh electrodes (Figure 2).

To determine the conductivity of IERB and quantify its effect on the compartment conductivity, a measurement cell was built and filled with 15 g of IERB mixture. Different concentrations of NaCl solution were injected and the conductivity of this 'resin bed' was measured using an alternating current (AC) method and analyzed using EIS (Electrochemical Impedance Spectroscopy) using IviumSoft software (Version 2.509, Ivium Technologies). Concentration series were: 0.001 M, 0.01 M, 0.017 M, 0.05 M, 0.1

M, 0.3 M, 0.5 M, 1.0 M. The same cell was used to measure the conductivity of glass beads and NaCl solution under corresponding concentrations. The specific conductivity of the resin bed was then plotted as a function of the specific conductivity of interstitial NaCl solution. A comparison of the conductivity of resin bed and interstitial solution was possible.

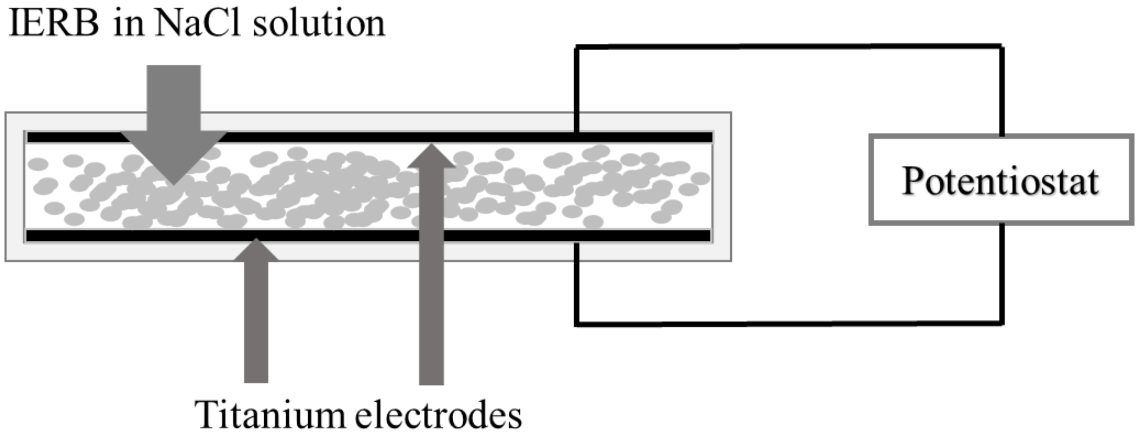

Figure 3 – Measurement cell for resin bed conductivity. Resin beads were filled in space between two titanium plate electrodes. NaCl solution of different concentration merged with IERB or glass beads to form a compact bed during the measurement.

4.3.5. Stack Resistance and Open Circuit Voltage

A RED stack, consisted of ion exchange membranes, dilute and concentrated water compartments, shows a resistance as a series of resistance-prone individual components. Therefore, the stack resistance R^c_{stack} can be calculated by a series resistance model in Eq. 21:

$$R^c_{stack} = \frac{1}{A_m} \cdot \left[n_c r_{cem} + n_a r_{aem} + N \cdot \left(\frac{d}{\kappa_d} + \frac{d}{\kappa_c} \right) \right] \tag{21}$$

where A_m is the effective area (m^2) of a single membrane, n_c and n_a are the numbers of cation and anion exchange membranes; N is the number of membrane pairs; d is the intermembrane distance (m); κ_d and κ_c are the specific conductivity ($S \cdot m^{-1}$) of dilute compartments filled with either IERB or glass beads, and concentrated compartments, respectively. Finally, r_{cem} and r_{aem} are the area resistance ($\Omega \cdot cm^2$) of cation and anion exchange membranes as the measured values with a concentration difference.

Chronopotentiometry was used to experimentally determine the stack resistance. Current density increased from 0 $A \cdot m^{-2}$ to 17.92 $A \cdot m^{-2}$ in 44 steps. In each step, the potentiostat maintained the current density for 15 seconds and took four potential measurements. Average potential values at each current level were plotted against the current density. The slope of the linear regression line was recorded as the ohmic stack resistance under direct current and compared with the calculated stack resistance. The potential measured at the beginning of the chronopotentiometry test (when current density was 0 $A \cdot m^{-2}$) was considered the OCV of the stack (see also Appendix A.3 for more detail).

4.3.6. Gross Power Density

The power density measurement was conducted using the same chronopotentiometry mode as used in the stack resistance measurement. The resulting voltage-current curves were used to calculate their product as power density (see also Appendix A.3 for more detail). The maximum product of voltage and current was adjusted by subtracting the maximum product from a blank run (with only one cation-exchange membrane in the stack). In each setting, tests were repeated at least three times. The reported maximum gross power density (P_{gross}) was the power normalized by the total membrane area. The power density of fumasep® membranes were measured using the same RED stack with regular spacers (referred to as "regular stack") and with glass-bead-filled in dilute compartments.

4.3.7. Pressure Drop and Pumping Energy

The hydraulic pressure difference between inlets and outlets of the RED stack was measured in a set-up as shown in Figure 3. Two glass pipes were connected to the inlet and outlet water pipes. Ends of both glass pipes were open so the water level could change freely to mark the water head when the two peristaltic pumps supplied distilled water into the system. The difference between the two water heads was measured as the water head drop (Δh) in meters, which was then translated to pressure drop (Δp) in mBars according to the following equation:

$$\Delta p = \frac{\Delta h \cdot \rho \cdot g}{100} \tag{22}$$

where ρ is the density of water (kg·m^{-3}) at 20°C, and g is the gravitational constant (m·s^{-2}).

The pressure drop provided a method to estimate the energy lost within the RED stack. To better evaluate the efficiency of an RED system, pumping energy loss was subtracted from the gross power generated to obtain the net power output.[95] Pumping power consumption (W) is calculated using the equation:

$$P_{pump} = \sum \Delta p_i \cdot Q_i \tag{23}$$

where Δp_i is the pressure drop (Pa) over either a dilute or concentrated compartment and Q_i is the flow rate (L·s^{-1}). The IERB or glass beads filling in the dilute compartments altered the hydraulic environment in those compartments. The pressure drop in the dilute compartments was generally different from the pressure drop observed in the concentrated compartments, and were measured separately.

Therefore, the net power density P_{net} (W·m^{-2}) can be estimated as the following:

$$P_{net} = P_{gross} - \frac{P_{pump}}{2NA_m} \tag{24}$$

where N is the cell number in the stack, and A_m is the active area (m^2) of an ion exchange membrane.

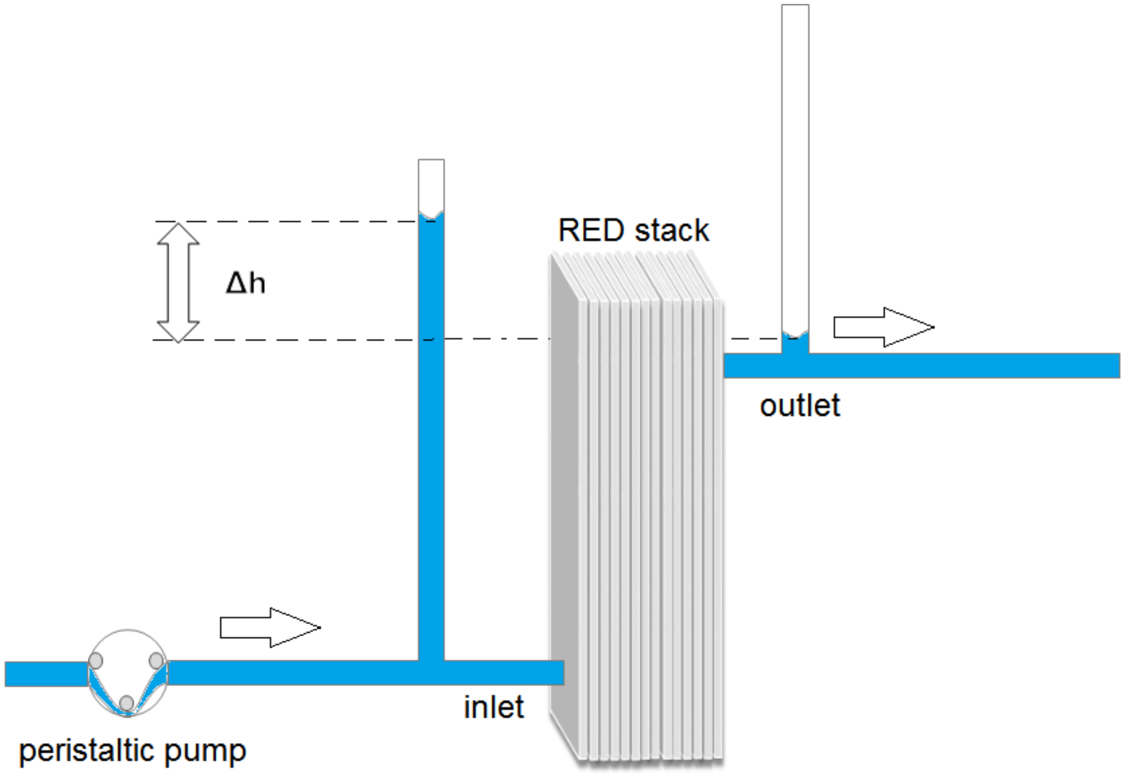

Figure 4 – Pressure drop was measured as the water head difference between inlet and outlet of the RED stack.

4.4. Results and Discussion

4.4.1. Effect of IERB on Ionic Conductivity

As shown in Figure 5a, ionic conductivity of NaCl solution, a resin-filled bed (NaCl solution filled with IERB), and a glass-bead-filled bed was higher when the interstitial solution concentration increased. Ionic conductivity of the resin bed was higher than the NaCl solution with the same concentration until the concentration of around 0.3 M was reached, and the curve of the resin bed conductivity intercepted with the interstitial solution conductivity line. However, when the interstitial solution concentration was higher than 0.3 M, the corresponding resin bed conductivity fell behind. For inert glass beads, the conductivity was significantly lower under all interstitial solution concentrations indicating a detrimental effect of glass bead filling on the conductivity. Figure 5b compares the conductivity of the resin bed and NaCl solution. This characteristic relationship, studied and reported in literatures, implies a mechanism explaining the improved ionic conductivity of a resin bed under relatively low concentration [94, 96, 97]. A porous plug model has been applied to quantitively study the presented conductivity trend of the resin bed as will be discussed in Section 4.4.2.

In a regular RED system, 0.017 M NaCl solution is commonly used as a dilute solution. A resin bed merged in 0.017 M NaCl solution illustrated the conductivity equivalent to an NaCl solution of about 0.25 M. The application of IERB in dilute compartments was expected to significantly decrease the resistance. Conversely, IERB-filled concentrated compartments would have lowered ionic conductivity than the 0.5 M NaCl solution. Therefore, I have only applied IERB in dilute compartments.

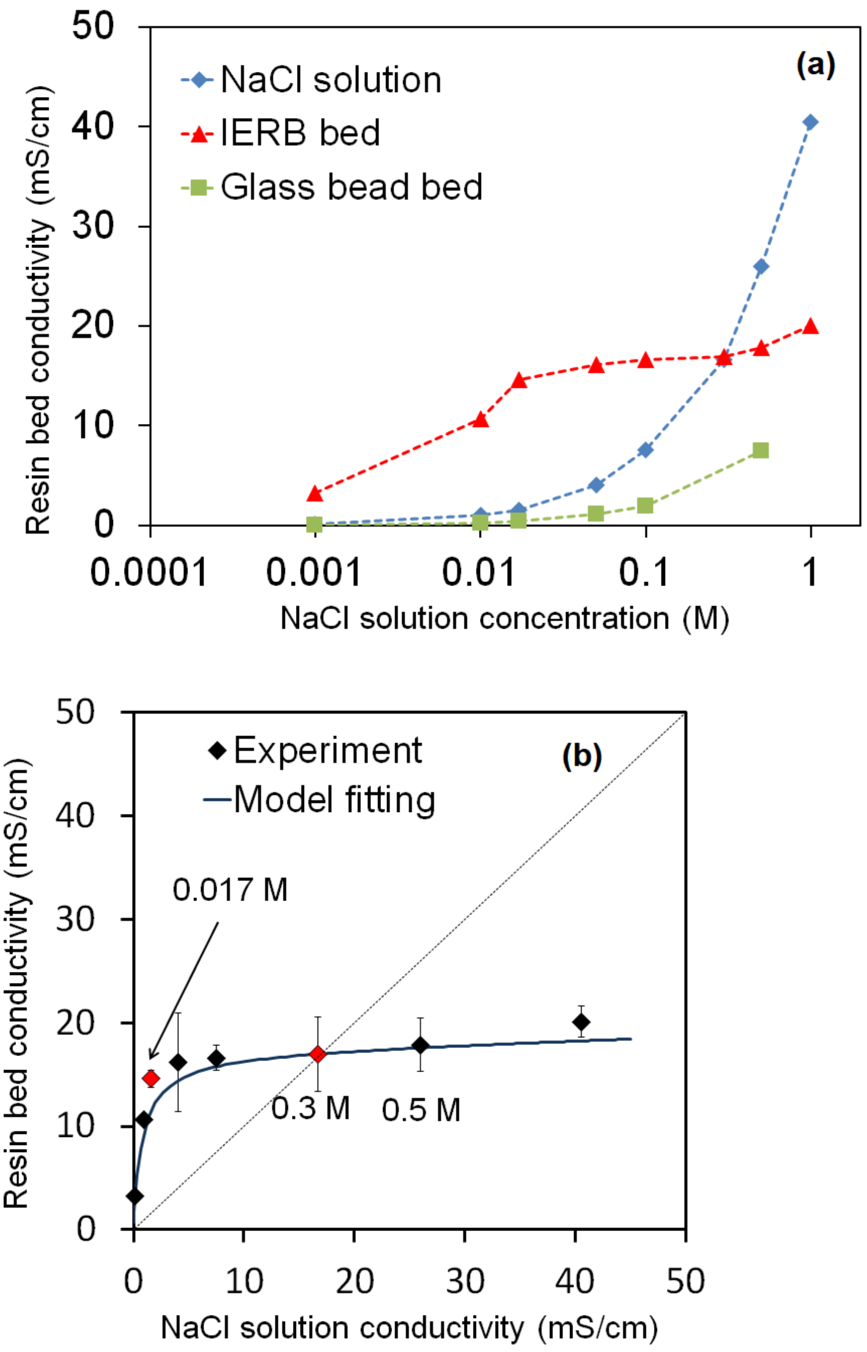

Figure 5 – (a) Specific conductivity of the resin bed, NaCl solutions, and the glass-bead-filled bed as a function of interstitial NaCl solution concentration. Dashed lines were added to guide eyes. (b) Specific conductivity of the resin bed as a function of the specific conductivity of interstitial NaCl solution. A diagonal line indicates equivalent NaCl solution specific conductivity. The curve represents the calculated values from porous plug model. For both figures, data points present concentration from left to right as: 0.001 M, 0.01 M, 0.017 M, 0.05 M, 0.1 M, 0.3 M, 0.5 M, 1.0 M.

4.4.2. Porous-plug model for resin bed conductivity

To better understand the conductivity behaviour of a resin-bead-packed compartment, a porous-plug model was applied following the procedure reported in the literature.[5] This model assumes that ionic current flows through three electrically different paths: (1) a mixture of resin phase and solution phase with a specific conductance of κ_1; (2) continuous phase of resin material with a specific conductance of κ_2; and (3) continuous phase of interstitial solution with a specific conductance of κ_3. Therefore, the specific conductance of resin-filled bed presents a conductivity (κ; $S \cdot m^{-2}$) of the sum of these three parallel elements as shown Figure 6.

$$\kappa = \kappa_1 + \kappa_2 + \kappa_3 \tag{25}$$

$$\kappa_1 = \frac{a\kappa_r\kappa_s}{d\kappa_s + e\kappa_r} \tag{26}$$

$$\kappa_2 = b\kappa_r \tag{27}$$

$$\kappa_3 = c\kappa_r \tag{28}$$

where κ_r is the specific conductance of resin material; κ_s is the specific conductance of interstitial solution as a function of solution concentration; *a* is the fraction of path (1); *b* is the fraction of path (2); and *c* is the fraction of path (3); *d* is the fraction of resin material in the thickness direction; and *e* is the fraction of solution phase in the thickness direction as shown in Figure 6.

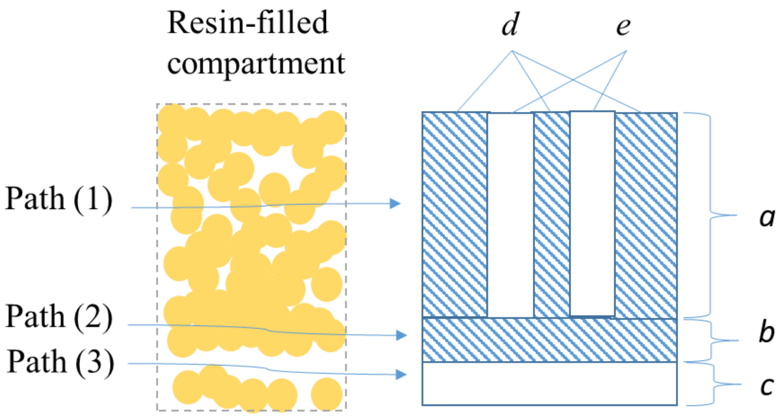

Figure 6 – Porous plug model with parameters explained

To calculate the parameters, I firstly plot resin-filled compartment conductivity (κ) versus interstitial solution conductivity (κ_S) from experimental data as shown in Figure 5b. The interseption and slope of the curve at characteristic points correlate with fractional parameters based on the mathematical properties of Eqs. 25 to 28 and generate Eqs. 29 to 33. Then, the parameters can be solved in a non-linear system of equations in five variables.

$$\frac{\kappa}{\kappa_r}|_{at\ \kappa_s=0} = b \tag{29}$$

$$\frac{d\kappa}{d\kappa_r}|_{at\ \kappa_s=0} = \frac{a}{e}+c \tag{30}$$

$$\frac{d\kappa}{d\kappa_r}|_{at\ \kappa_r=\kappa_s} = ae+c \tag{31}$$

$$a + b + c = 1 \tag{32}$$

$$d + e = 1 \tag{33}$$

Based on the experimental data, I calculated the parameters as shown in Table 5 at different concentrations of solution. The calculated conductivity using porous plug model is plotted as a curve as shown in Figure 5b. The presented trend implies that the resistance-in-parallel model simulates the behavior of resin bed well. A highly conductive resin phase contributed the most of conductivity when solution concentration was low. As solution concentration increased, resin bed conductivity was assumed to stay the same in the model. When the solution concentration was high enough, stagnant resin phase actually served as impedance of the total conductivity explaining the slow increase of resin bed conductivity towards high solution concentration.

Table 5 – Parameters used in porous plug model

Parameters	**Value**
a	0.9357
b	0.0332
c	0.0311
d	0.9516
e	0.0484

4.4.3. Stack Resistance and OCV

As seen in Figure 7, the resistance measured in a RED stack did not vary significantly with different flow rates except for the stack filled with glass beads. The regular stack had a resistance of 10 Ω at a flow rate of 23 $mL \cdot min^{-1}$, while the resistance of the IERB-filled stack was only 6.1 Ω. At a flow rate of 76 $mL \cdot min^{-1}$, the resistance of the regular stack decreased marginally to 9.7 Ω. The resistance of the IERB filled stack was not significantly affected by flow rate. The glass-bead-filled stack did show a significant decrease in the resistance from 22.1 Ω to 20.1 Ω under different flow rates.

An intermembrane distance of 500 μm was relatively large compared to contemporary RED systems. Because most of resistance in a dilute compartment was determined by convection controlled bulk solution, the effect of concentration polarization near membrane surface on resistance was relatively insignificant [12, 45]. Therefore, I did not observe obvious effect of flow rate on the stack resistance within the range concerned in this study. For an IERB-filled stack, improved ionic conductivity helped diminishing polarization caused by transport limitation at both membrane-solution and resin-solution interfaces [98]. As a result, stack resistance was affected by flow rate. The glass-bead-filled stack, due to its low conductivity in dilute compartments, suffered more from concentration polarization, and as a result, was affected obviously by flow rate.

The calculated stack resistance was under-estimated in general compared to experimentally measured resistance. The deviation could stem from the detrimental effect of spacer in the stack [12, 72]. Non-conductive spacer material inevitably blocked ion transport pathways and resulted in a resistance due to transport limitation. Nonetheless, resistance model calculation supported that dilute compartments had a significant contribution to the overall resistance. Membrane resistance and resistance of the concentrated solution were consistent under different circumstances, leaving the conductivity of the dilute compartments critical to the overall resistance. In the regular stack and the glass-bead-filled stack, dilute compartments counted for more than half of the overall resistance. When IERB was filled in the dilute compartments, resistance of these compartments decreased significantly to the same order of the concentrated compartments. Consequently, overall stack resistance was lowered. On the other hand, glass-bead-filled compartments were detrimental to conductivity, and thus, resulted in a much higher stack resistance. As expected, a change of resistance in dilute compartments could explain most, if not all, the changes in overall stack resistance. The effect of IERB filling has proven to be beneficial to the ionic conductivity of the system. Results of power density measurement in the following section demonstrated this effect.

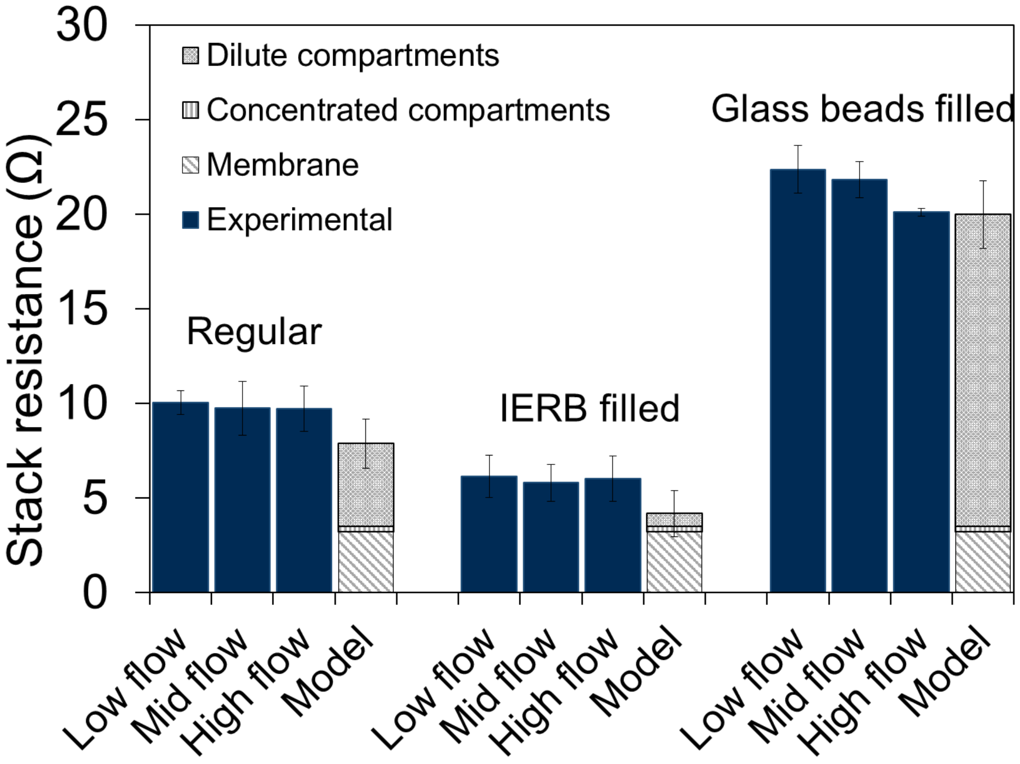

Figure 7 – Stack resistance under low flow rate (23 mL·min^{-1}), mid flow rate (38 mL·min^{-1}), and high flow rate (76 mL·min^{-1}) compared to model prediction for regular stack, IERB-filled stack, and glass-bead-filled stack, respectively. Calculated resistance includes three parts: dilute compartments, concentrated compartments, and ion exchange membranes as indicated by the fourth bars in each group.

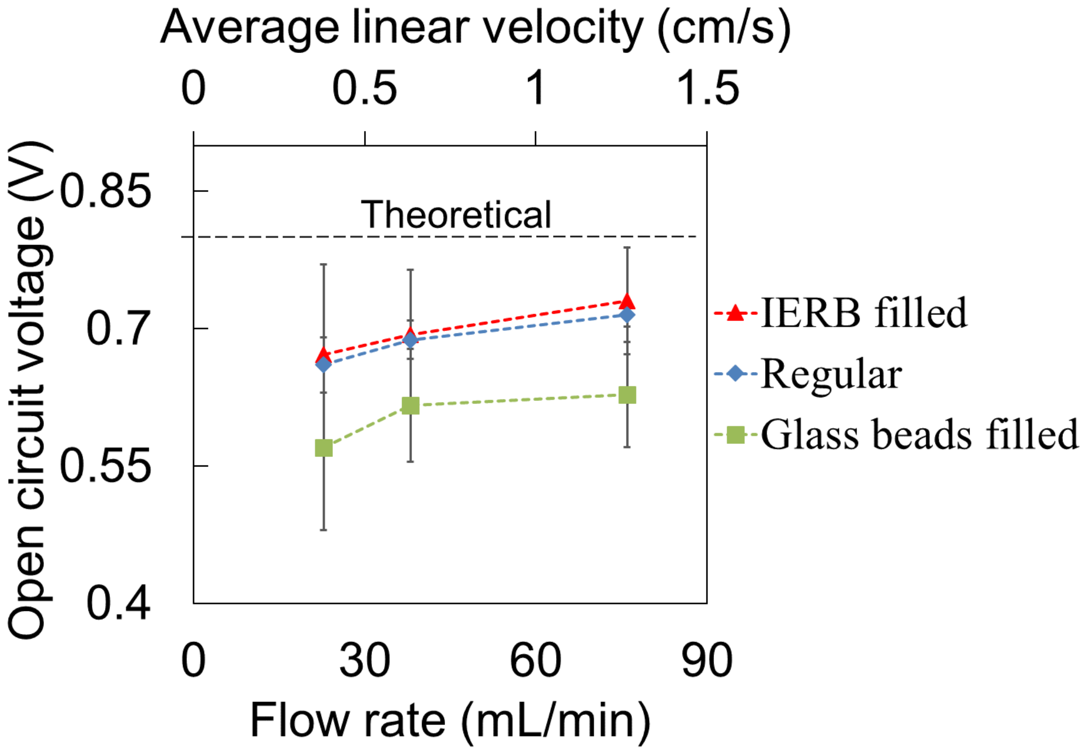

Figure 8 – Open circuit voltage measured in regular stack, a stack with IERB filling the dilute compartments, and a stack with glass beads filling the dilute compartments, respectively. Dashed line indicates that the theoretical open circuit voltage of a stack with 5 cells is 0.80 V. Dashed lines were added to guide the eyes.

The OCV measured in IERB-filled stacks was comparable to the voltage measured in a regular stack (Figure 8). However, the glass-bead-filled stack showed significantly lower OCVs. Flow rate affected the OCV. This phenomenon is usually explained that higher flow rate usually diminishes the diffusion boundary layer and reduces concentration polarization [11, 72]. However, those concentration polarizations may not have significant impact on the OCV measurements under no current flow. Instead, osmosis effect and co-ion leakage may have important contributions to the concentration polarization near membrane surface. Firstly, a small amount of water can transport through membrane due to the osmotic pressure could dilute solution on one side and concentrate solution on the other side near membrane surface making the concentration polarization possible. Secondly, imperfect permselectivity membrane leaks co-ions through membrane which results in net salt transport. As a result, the concentration right at the membrane-solution interface in the concentrated side is lower than that in bulk solution while the concentration right at the membrane-solution interface in the dilute side is higher than that in bulk solution. Those types of concentration polarizations can still happen. Consequently, the aforementioned concentration polarization phenomena would impact the changes of OCV caused by different flow rates. An IERB-filled stack maintained the same level of OCV compared to the regular stack at different flow rates and achieved the highest OCV of 0.73 V, which translated to an apparent permselectivity of over 90%. Therefore, IERB packed in between membrane did not alter the membrane potential even though local concentration of ions near each resin bead was higher than the bulk solution.

4.4.4. Gross Power Density of RED Stacks

Gross power density is a direct measure of power performance of a RED system. The absolute value of gross power density various from system to system depending on the number of cells in a stack, the salinity gradient, ion exchange membranes used, effective area of these membranes, and the intermembrane distance [99]. In the current setup, the regular stack achieved a gross power density of 0.27 $W \cdot m^{-2}$ at an average flow velocity of 0.38 $cm \cdot s^{-1}$ as shown in Figure 9. When 6 g IERB was filled in dilute compartments, the power density was improved to 0.47 $W \cdot m^{-2}$ at the same flow rate, or improved by 74%. As the flow rate increased, the gross power density increased in all three cases but at different rates. When the average linear velocity increased to 1.3 $cm \cdot s^{-1}$, the gross power density of the regular and the IERB-filled stacks raised to 0.32 $W \cdot m^{-2}$ and 0.59 $W \cdot m^{-2}$, respectively, implying an increase of 84%. On the other hand, the gross power density of stacks filled with glass beads was never higher than 0.14 $W \cdot m^{-2}$ at all flow rates.

The gross power density obtained experimentally correlated well with stack resistance and OCV data. The flow rate effect on resistance and OCV was manifested comprehensively on the power density values. An IERB-filled stack showed the highest OCV and the best conductivity with the help of resin beads as well as the highest gross power density. Even though the regular stack maintained the same level of OCV, the resistance in the regular stack almost doubled, which caused a power density slightly over half of the power density of the IERB-filled stack. The gross power density achieved in the glass-bead-filled stack ruled out that improved power density in the IERB-filled stack was caused merely by different hydrodynamic environment within compartments. Observed low OCV in addition to the highest stack resistance explained the lower power density in the glass-bead-filled stack.

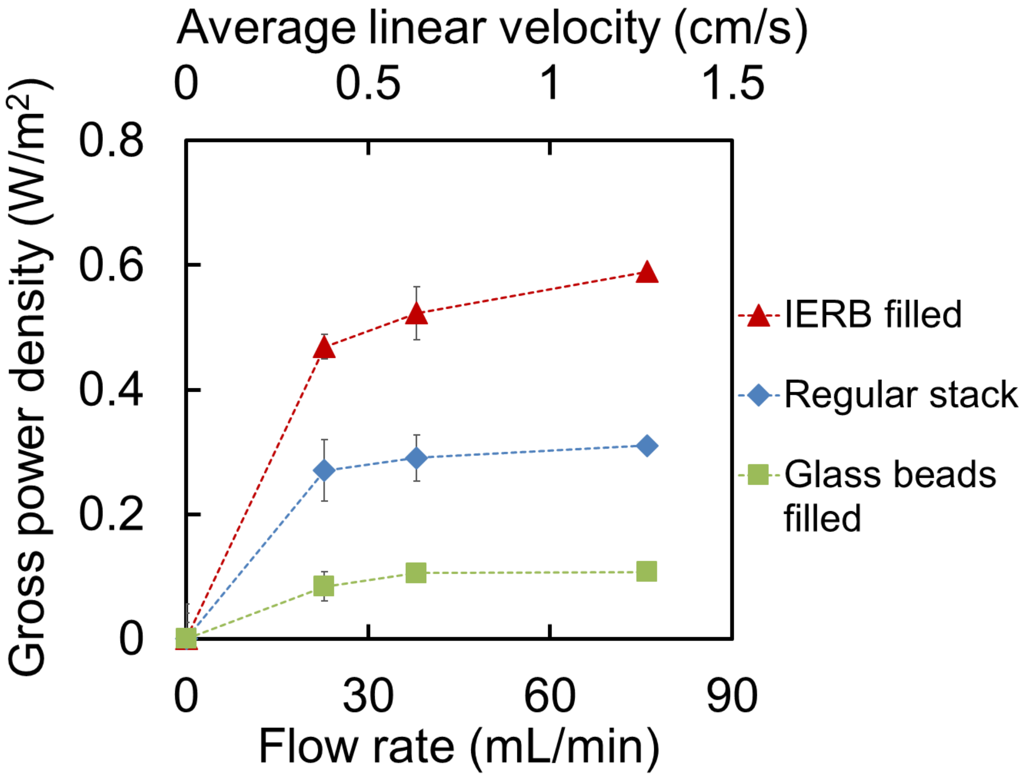

Figure 9 – The maximum power density achieved as a function of different flow rates. Dashed lines were added as a directional visual aid.

4.4.5. *Pressure Drop and Net Power Density*

Pumping energy, estimated directly from pressure drop and flow rate, is a major energy consumption in a RED system.[95] The effect of flow rate on the pressure drop was measured for all three stacks as shown in Figure 10. When the average linear velocity of feed solution was increased, the pressure drop increased rapidly. In the regular stack, the flow rate increased from 23 mL·min^{-1} to 76 mL·min^{-1}, while the pressure drop increased from 11.3 mBar to 39.5 mBar. I measured the pressure drop in the IERB-filled and glass-bead-filled stacks separately so that the difference of hydraulic environment in dilute and concentrated compartments was properly evaluated. Compartments filled with either IERB or glass beads resulted in a higher pressure drop compared to regular compartments at all flow rates. At low flow rate (23 mL·min^{-1}), the pressure drop in either IERB or glass beads-filled compartment was higher than a regular compartment. At higher flow rate, the pressure drop in the IERB-filled and glass-bead-filled compartments increased even faster compared to the increase of pressure drop in a regular compartment. The unambiguous conclusion was that pumping water through these filled compartments was more difficult than through spacers. Concentrated compartments in all three stacks showed comparable pressure drops. This result served as an indirect prove that the filling of IERB and glass beads did not affect these concentrated compartments significantly.

The net power density was calculated based on Equation 4 to eliminate the pumping energy consumption (Figure 11). Pumping power was not substantial at a flow rate of 23 mL·min^{-1} (0.02 to 0.03 W·m^{-2}) in all three stacks, but increased radically to obviously detrimental at a flow rate of 38 mL·min^{-1} (0.06 W·m^{-2} in the regular stack and 0.09 W·m^{-2} in the IERB-filled stack). At the highest flow rate (76 mL·min^{-1}), pumping power was 0.28

$W·m^{-2}$ in the regular stack and 0.31 $W·m^{-2}$ in the IERB-filled stack. The net power density was dragged down to nearly 0 $W·m^{-2}$ in the regular stack and to 0.28 $W·m^{-2}$ in the IERB-filled stack. The best net power density achieved in the IERB-filled stack was 0.44 $W·m^{-2}$ at a flow rate of 38 $mL·min^{-1}$.

A rapid increase of gross power density with increasing flow rate was shown in Figure 9 in the IERB-filled stack compared to the regular stack. However, this increase was immediately smoothed by an even faster increase of pumping power and caused a turning point on the net power density curve at around 30 $mL·min^{-1}$ in all three stacks. Consequently, the optimum operating condition of an IERB-filled stack was still in the low flow rate range. This phenomenon has also been reported and set the limitation of net power output from a RED system.[42, 45, 59, 81]

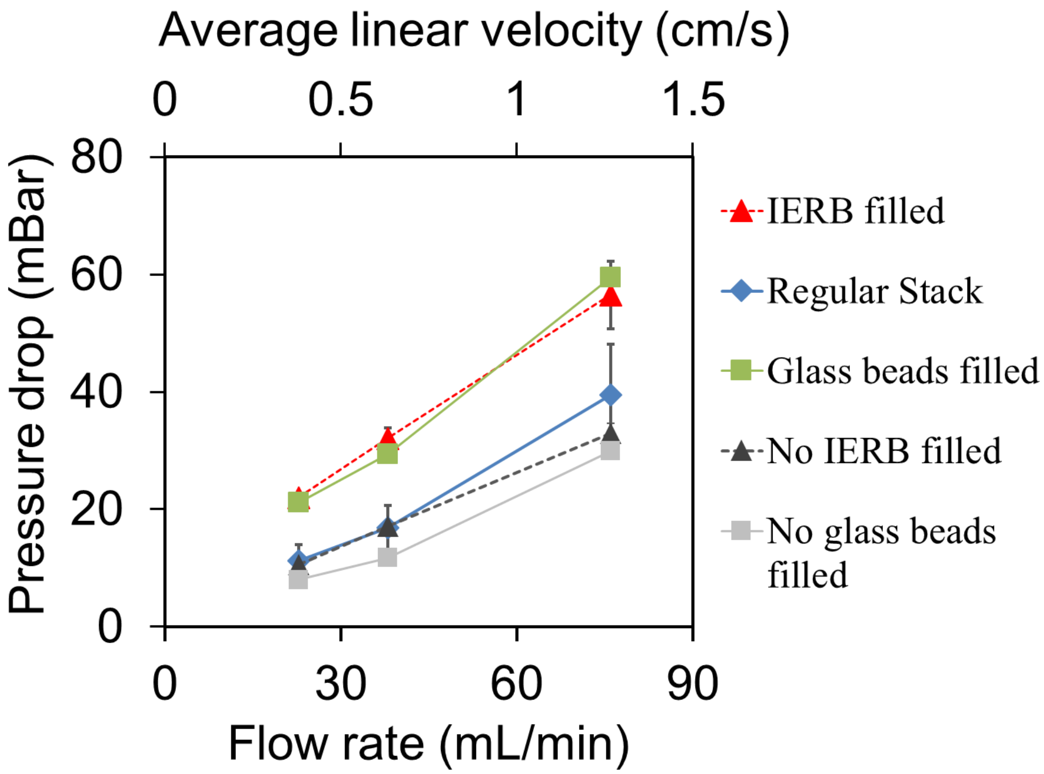

Figure 10 – Pressure drop between the inlet and outlet of the RED stack. Notice that the pressure drop in compartments filled with IERB or glass beads (the dilute compartments) and in regular compartments (the concentrated compartments) were measured separately and notified in the legend. "No IERB-filled" represents the concentrated compartments in the IERB-filled stack and "No glass-bead-filled" represents the concentrated compartments in the glass-filled stack. Dashed lines were added as a directional visual aid.

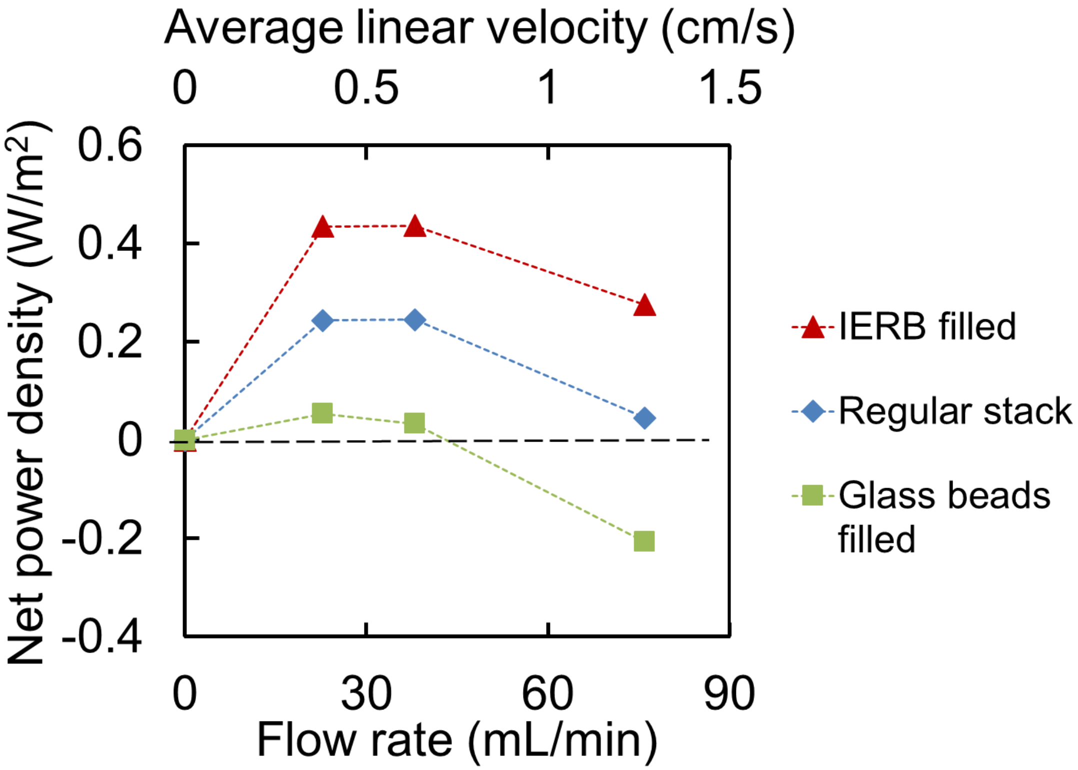

Figure 11 – Net power density calculated based on Equation 4 for IERB-filled, regular, and glass-bead-filled stacks, respectively. A horizontal dashed line marks the boundary of net positive and net negative power density. Dashed lines connecting data points were added as a directional visual aid.

4.5. Conclusions

I significantly improved the conductivity of the dilute compartments in a RED stack by using IERB to replace conventional non-conductive spacer materials. Both gross and net power densities were improved by over 75% at higher flow rate compared to a regular stack. IERB filling is therefore a novel approach to resolving the transport limitation caused by low salinity and enhancing power output of a RED system. In addition, IERB is beneficial to a RED stack because this system potentially suffers less from the concentration polarization effect. Supplying feed solution at a lower flow rate in the IERB-filled stack could be enough to achieve a comparable power output that a regular stack could achieve at higher flow rate. Effects of different resin type and size could also reveal more potential of this novel approach.

CHAPTER 5. AN INTEGRATED MODELING AND EXPERIMENTAL STUDY ON THE IONIC RESISTANCE OF ION EXCHANGE MEMBRANES

In the previous chapters, I have focused on the environmental factors that affect overall conductivity and performance of the RED system. In this chapter, I will focus on the properties of the key component of the system, ion exchange membranes, and potential improvements through an integrated experimental and modeling approach.

5.1. Abstract

In many applications, the ionic resistance of an ion-exchange membrane shows a strong dependency on the external solution concentration and hydrodynamic environment. It is critical to understand the insights of ion exchange membrane process if its ionic resistance can be simulated accurately. In this paper, I have developed a new model by taking into account both the membrane properties that affect the membrane bulk resistance and hydrodynamic environment that affects the non-ohmic behavior of membrane resistance. The new model not only explains external solution concentration dependency, but also explicitly establishes a relationship between the measured membrane resistance and current density. The modeling results on the direct current (DC) and alternating current (AC) resistance of membranes are compared with experimental data measured under different external solution concentrations and applied to current densities. I demonstrate that the model accurately predicts the behaviors of sulfonated PPO (SPPO) and fumasep®-FKS and FAS membranes in all cases. The integrative modeling and experimental study

provides insights into the ion-exchange membrane synthesis as well as reverse and conventional electrodialysis (ED) processes.

5.2. Introduction

IEMs are widely used in various electrochemical systems [7, 27, 39, 88, 100, 101]. Key membrane properties, such as electrical resistance and permselectivity, usually maintain the functionality and determine the efficiency of these systems. The selectivity of ion-exchange membranes enables the separation of cations and anions in a solution thereby making ED and deionization processes possible. The efficiency of system operation depends on the overall electrical resistance of the system which is significantly determined by membrane resistance. For example, salinity gradient energy generated through reverse electrodialysis (RED), has been a hot topic for researchers who see ion-exchange membranes as the key component of RED conversion [34, 65, 66]. In this application, Membrane resistance is critical in this application since the output power density is directly affected by energy lost from electrical resistance.

The ionic resistance of an ion-exchange membrane is commonly determined by experimental methods using direct current (DC) or by electrical impedance spectrometry (EIS) using alternating current (AC) while the membrane is immersed in a NaCl or KCl solution [6, 8, 9, 11, 13, 19, 83, 102, 103]. Because concentration polarization occurs due to ionic current flow, diffusion boundary layers (DBLs) evolve on both sides of the membrane and are characterized by a change in the electrolyte concentration near the solution-membrane interface. As a result, the measured membrane resistance varies significantly when the measurement is taken under different operating conditions (i.e., different external solution concentrations or applied current densities) [10, 13, 104].

Previous studies treated this complexity as the overpotential and modeled using EIS, while the overall system resistance was estimated using experimental values [10, 13, 15, 101]. The boundary layer effects near the solution-membrane interface have also been investigated in several reported studies [20, 53, 69, 102, 105].

However, reliable information on the concentration-dependency of membrane resistance is lacking, and the effect of electrical current density has not been explored in detail [105, 106]. For applications such as RED and ED, each membrane is not in contact with electrolyte solution of same concentration on both sides and the electrical current in the system may vary. Consequently, the commonly used value of membrane resistance measured under these conditions does not represent the apparent resistance of a membrane in these systems. An RED system model using this approach is not fully applicable if the internal resistance is determined on the basis of the summation of the separately measured resistances of the membrane and other components [13, 33, 39, 102, 107, 108].

Furthermore, the electrochemical properties of membrane material and its relationship to resistance is important to the synthesis of the membrane. The extent of improvement attainable through optimization of membrane properties can be limited by the environment of membrane application. The results of this limitation have led to a need for further research on how the membrane properties can be better managed so as to benefit from the environment. Therefore, this article aims to develop a novel membrane resistance model that provides a comprehensive description of the apparent resistance of both cation-exchange membranes (CEMs) and anion-exchange membranes (AEMs). The model is derived directly from the membrane's electrochemical properties under different operating conditions.

5.3. Model Development

According to the classical electrochemical analysis of a solution with diffusion limiting transport, the solution-membrane interface concentration of salt varies with the density of the electrical current flowing through the solution [33, 53]. In a sodium chloride solution, Na^+ and Cl^- ions carry the electrical current equally. However, in the membrane phase, only counter-ions are the major carriers of current. The difference in the counter-ion transport numbers in the solution and in the membrane phase causes a gradient of concentration perpendicular to the membrane plane that is usually called "concentration polarization" [27]. As a result, on one side of the membrane, the counter-ion (ions having opposite charge compared to membrane bulk material) is approaching the membrane-solution interface. Because of a faster transport of counter-ion across the membrane and the migration of co-ion (ions with the same charge as membrane bulk material), electroneutrality is maintained and generates a depletion of salt concentration. On the other side accumulation of counter-ion due to a sudden decrease of transport accompanied with migration of co-ion maintains the electroneutrality and generates an accumulation of salt concentration. The concentration obeys a linear decrease while approaching the membrane surface at a steady state when transport is stabilized.

5.3.1. Non-ohmic Resistance in DBLs

As shown in Figure 12, the salt concentration at the solution-membrane interface is a function of the applied current density (i) and limiting current density (i_{lim}). Eq. 34 describes the concentration variation on the depleting side of DBL and Eq. 35 on the accumulating side [43, 53].

$$C_1^b\left(i\right) = C_0\left(1 - \frac{i}{i_{\text{lim}}}\right) \tag{34}$$

$$C_2^b\left(i\right) = C_0\left(1 + \frac{i}{i_{\text{lim}}}\right) \tag{35}$$

where C is the concentration of salt (mol·L^{-1}), the subscripts 1 and 2 indicate the depleting and accumulating sides, respectively, and C_0 is the concentration of the bulk solution. The superscript b indicates that the concentrations concerned at the solution-membrane interface.

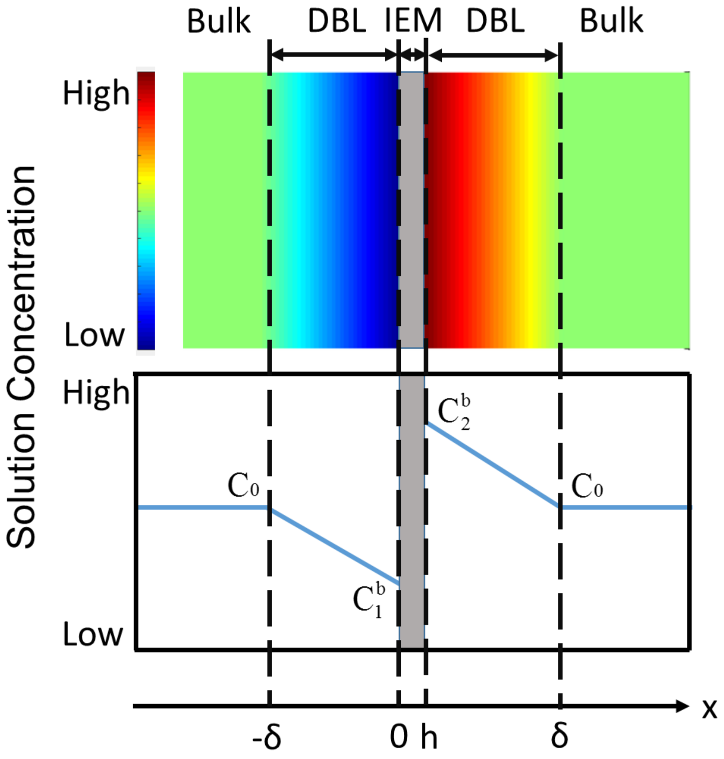

Figure 12 – DBL near the surface of a cation-exchange membrane and the salt concentration distribution in different layers at steady state. Current direction is to the right. This illustrates the common situation in which the membrane resistance is measured with the same bulk solution concentration on both sides of the membrane using direct current. The left side shows a depleting side of DBL and the right side shows an accumulating side of DBL. (The schematic is not drawn to scale.)

At steady state, the concentration gradient in the DBL is assumed to be constant [43, 49]. From Figure 12, the concentration in the DBL as a function of distance (x; m) to the interface can be expressed as:

$$C_1\left(x\right)=C_1^b+\frac{C_1^b-C_0}{\delta}x \tag{36}$$

$$C_2\left(x\right)=C_2^b-\frac{C_2^b-C_0}{\delta}\left(x-h\right) \tag{37}$$

where h is the thickness (m) of the membrane and δ is the thickness (m) of the DBLs as shown in Figure 12. Because the flow rate and dimension of equipment are kept the same for different situations studied in this work, the thickness of DBLs on both sides are assumed to be the same as determined by flow rate [109-111]. Then, the resistances of the electrolyte (R_{L1} and R_{L2} in $\Omega\cdot\text{m}^2$) from the DBLs on each side of the membrane are given by the integral over the thickness of each DBL [53]:

$$R_{L1}=\int_{-\delta}^{0}\frac{1}{\kappa_1}dx=\int_{-\delta}^{0}\frac{1}{\Lambda\cdot C_1\left(x\right)}dx=\frac{\delta}{\Lambda\cdot\left(C_0-C_1^b\right)}\ln\frac{C_0}{C_1^b} \tag{38}$$

$$R_{L2}=\int_{h}^{h+\delta}\frac{1}{\kappa_2}dx=\int_{h}^{h+\delta}\frac{1}{\Lambda\cdot C_2\left(x\right)}dx=\frac{\delta}{\Lambda\cdot\left(C_0-C_2^b\right)}\ln\frac{C_0}{C_2^b} \tag{39}$$

where κ_1 and κ_2 are the conductivities ($\text{S}\cdot\text{m}^{-1}$) of the DBLs, and Λ is the molar conductivity of the salt solution ($\text{S}\cdot\text{m}^3\cdot\text{mol}^{-1}$). The x-axis is the direction perpendicular to the membrane surface. Substituting Eqs. 34 and 35 into Eqs. 38 and 39, and combining them, I obtain:

$$R_L = \left(\frac{\delta}{r \cdot \Lambda} \ln \frac{1+r}{1-r} \right) \cdot \frac{1}{C_0} \tag{40}$$

$$r = \frac{i}{i_{\lim}} \tag{41}$$

The above equation represents a change in the electrolyte conductivity as a result of concentration polarization. If the transport numbers of cations and anions are different in the solution phase (e.g., NaCl solution), a diffusion potential exists, and are denoted as E_{d1} and E_{d2} indicating depleting and accumulating sides, respectively. The resultant resistances can be expressed as:

$$R_{d1} = \frac{E_{d1}}{i} = -\frac{RT}{iF} \Delta t \ln \frac{a_0}{a_1^b} \tag{42}$$

$$R_{d2} = \frac{E_{d2}}{i} = -\frac{RT}{iF} \Delta t \ln \frac{a_2^b}{a_0} \tag{43}$$

Here, Δt is the difference of ion transport numbers in the solution phase. Adding Eqs. 42 and 43 together and substituting Eqs. 34 and 35 to replace the concentration term, I can obtain Eq. 44.

$$R_d = \frac{RT}{iF} \Delta t \cdot \ln \frac{a_2^b}{a_1^b} = \frac{RT}{iF} \Delta t \cdot \ln \frac{\gamma_2 C_2^b}{\gamma_1 C_1^b} = \frac{RT}{iF} \Delta t \left(\ln \frac{1+r}{1-r} + \ln \frac{\gamma_2}{\gamma_1} \right) \tag{44}$$

Here, γ indicates the activity coefficient. The minus sign, which indicates that the direction of the potential is opposite to that of the direct of current, is dropped for resistance calculation. While the concentration on both sides are not the same, as in the case of concentration polarization, a membrane potential E_m^{DBL} is generated. The potential is reflected as a resistance that can be expressed in Eq. 45 [112]. The minus sign is dropped here as well as in resistance calculation.

$$R_m^{DBL} = \frac{E_m^{DBL}}{i} = \frac{RT}{iF}\Delta\bar{t}\cdot\ln\frac{a_2^b}{a_1^b} = \frac{RT}{iF}\Delta\bar{t}\cdot\ln\frac{\gamma_2 C_2^b}{\gamma_1 C_1^b} = \frac{RT}{iF}\Delta\bar{t}\left(\ln\frac{1+r}{1-r}+\ln\frac{\gamma_2}{\gamma_1}\right) \tag{45}$$

where $\Delta\bar{t}$ represents the difference of transport numbers of counter-ions and co-ions in the membrane phase.

5.3.2. Resistance of Membrane Bulk Material

Because only the solution phase in the membrane structure is conductive, the transport properties considered here concern only the membrane-phase solution and salt ions inside the solution. Also, the electrochemical properties of the membrane are treated as being homogeneous.

Using the 1-D Nernst-Planck equation, I only deal with the case where the valence of the ions is unity (because sodium chloride is the only salt used here). Also, I assume a steady-state convection; thus, the DBL is stable near the membrane solution interface. Finally, the diffusion and migration can be described using the Nernst-Einstein equation (Eq. 46), for a species *k*:

$$u_k = \frac{D_k F}{RT} \tag{46}$$

$$J_k = -D_k\frac{dC_k}{dx} - u_k C_k\frac{d\varphi}{dx} = -D_k\frac{dC_k}{dx} - D_k\frac{C_k F}{RT}\frac{d\varphi}{dx} \tag{47}$$

where J_k is the flux of ions (mol· m^{-2}·s^{-1})) in the solution, D_k is the diffusivity of an ion species (m^2·s^{-1}), φ is the external electrical potential applied to the system (V), u_k is the mobility of ions (m^2·V^{-1}·s^{-1})), R is the gas constant, F is the Faraday constant, and T is the temperature (K). Moreover, the diffusion term can be further defined such that the current density is [33]:

$$i = F\sum_k J_k = -F^2 \sum_k \frac{C_k D_k}{RT}\left(\frac{RT}{C_k F}\frac{dC_k}{dx} + \frac{d\varphi}{dx}\right) = -F^2 \sum_k \frac{C_k D_k}{RT}\left[\frac{d}{dx}\left(\frac{RT}{F}\ln C_k\right) + \frac{d\varphi}{dx}\right] \quad (48)$$

Both terms in the bracket have the dimension of potential gradient and thus can further be expressed in a combined form (the electrochemical potential gradient if the pressure components are neglected). Let the combined potential be Φ (V), then,

$$i = -F^2 \sum_k \frac{C_k D_k}{RT}\frac{d\Phi}{dx} \quad (49)$$

However, Ohm's law states that the conductivity κ (S·m^{-1}) is:

$$i = \kappa \frac{d\Phi}{dx} \quad (50)$$

Thus, by comparing Eq. 49 into Eq. 50, the conductivity of the membrane phase solution is:

$$\kappa = F^2 \sum_k \frac{C_k^m D_k^m}{RT} \quad (51)$$

The superscript m indicates that the value is for the membrane phase. Note that the minus sign only indicates the direction of the current in Eq. 49 and is neglected in Eq. 50. Finally, if I assume the concentration is uniform within the membrane phase for both counter- and co-ions, I can conclude that the ionic resistance of the solution in the membrane phase (R_m) is:

$$R_m = \int_0^h \frac{dx}{\kappa^m} = \int_0^h \frac{RT}{F^2 \cdot \left(D_{ct}^m C_{ct}^m + D_{co}^m C_{co}^m\right)} dx = \frac{hRT}{F^2 \cdot \left(D_{ct}^m C_{ct}^m + D_{co}^m C_{co}^m\right)} \tag{52}$$

The subscripts *ct* and *co* indicate counter-ion and co-ion, respectively. The counter- and co-ion concentrations in the membrane phase can be derived from the Donnan equilibrium [14]:

$$C_{ct}^m = \frac{C_{fix}}{2} + \sqrt{\left(\frac{C_{fix}}{2}\right)^2 + \left(C_i^\delta\right)^2} \tag{53}$$

$$C_{co}^m = -\frac{C_{fix}}{2} + \sqrt{\left(\frac{C_{fix}}{2}\right)^2 + \left(C_i^\delta\right)^2} \tag{54}$$

where C_{fix} is the fixed charge density (FCD) (eq.$\cdot$L^{-1}) in the ion-exchange membrane. It is calculated as the ratio of ion exchange capacity (IEC) to swelling degree (SD):

$$C_{fix} = \frac{IEC}{SD} \tag{55}$$

The co-ion concentration can be assumed to be negligible in the membrane due to Donnan exclusion. In the concentration range concerned in this study, co-ion concentration is two orders of magnitude lower than counter-ion concentration in the membrane [112]. Furthermore, from Eq. 53, if the concentration at the solution-membrane interface C^b is relatively small compared to C_{fix}, the counter-ion concentration is very close to C_{fix}. Then Eq. 52 becomes:

$$R_m = \frac{hRT}{F^2 \cdot \left(D_{ct}^m C_{ct}^m + D_{co}^m C_{co}^m \right)} \cong \frac{hRT}{F^2 D_{ct}^m C_{fix}} \tag{56}$$

The assumption here is well justified with a typical membrane used in this study. For example, the SPPO membrane has a fixed charge density of 5.15 mol·L^{-1} using Eq. 55, which results in a counter-ion concentration of 5.20 mol·L^{-1} in the NaCl solution of 0.5 mol·L^{-1} as indicated in Eq. 53. This result is in agreement with the model used in the ED field [69, 103]. Furthermore, because the counter-ion considered can be different in CEMs and AEMs, the derivation is valid to either type of IEM. For simplicity, the membrane-property-related parameters D_{ct}^m and C_{fix} are denoted as a single parameter M.

5.3.3. The Measurement of Resistance Under DC Conditions

The common measurement of membrane resistance using the DC method is severely affected by the DBL; in fact, the resulting resistance is partly caused by the DBL even under vigorous stirring [10]. If the resistance is measured with the same concentration of solution on both sides of the membrane, the reported result (R_0) is the difference between the experimental (R_E') and blank (R_{BL}) resistances compensated by the solution resistance that has the same resistance of solution with thickness h [113]:

$$R_0 = R_E - R_{BL} + \frac{h}{\Lambda \cdot C_0} \tag{57}$$

I neglect all resistances other than the resistance raised due to the formation of DBL because subtraction of the blank removes such resistances from the result. During DC measurement of membrane resistance with the same bulk solution concentration on both sides of the membrane, the combination of the four resistances from Eqs. 40, 44, 45 and

56 gives the total resistance of the membrane as it adds up the change of resistance in DBL, the diffusion generated resistance, and the membrane-potential-related resistance:

$$R_E = R_L + R_d + R_m^{DBL} + R_m \tag{58}$$

The blank resistance to be subtracted is calculated as the resistance of the solution that replaces the two DBLs and the membrane bulk in thickness:

$$R_{BL} = \frac{2\delta + h}{\Lambda \cdot C_0} \tag{59}$$

Thus, Eq. 57 becomes:

$$R_0 = a \cdot \frac{1}{C_0} + b \tag{60}$$

$$a = \frac{\delta}{r \cdot \Lambda} \ln \frac{1+r}{1-r} - \frac{2\delta}{\Lambda} \tag{61}$$

$$b = \frac{hRT}{F^2 M} + \frac{RT\left(\Delta t + \Delta \bar{t}\right)}{r i_{lim} F} \cdot \left(\ln \frac{1+r}{1-r} + \ln \frac{\gamma_2}{\gamma_1} \right) \tag{62}$$

As a result, the resistance measured by the DC method is dependent on the external solution concentration C_0. The linear relationship between the measured resistances and the reciprocal of the bulk solution concentration is expected. Furthermore, it can be proved using L'Hôpital's rule that the "*a*" term in front of the reciprocal of concentration approaches to two when r approaches zero (i.e., no electrical current flow).

5.4. Materials and Methods

5.4.1. Synthesis of SPPO membrane

Poly (2,6-dimethyl-1,4-phenylene oxide) (PPO), analytical standard grade, was purchased from Sigma Aldrich. The PPO sulfonation was carried out according to the procedure described in the literature [65, 99]. Chloroform (Sigma Aldrich, anhydrous, 99 %) and methanol (Sigma Aldrich, anhydrous, 99.8 %) were used as solvents, and chlorosulfonic acid (VWR, 99%) was used as the sulfonating agent.

5.4.2. Membrane resistance measurement using DC

Membrane samples were placed between two PMMA (poly(methyl 2-methacrylate)) cells each with a volume of 460 ml (7.6 cm × 7.6 cm × 8 cm) (Figure 13). Sodium chloride solution was supplied at a flow rate of 60 $ml \cdot min^{-1}$ by a Masterflex® peristaltic pump (Cole-Parmer, USA). The membrane had an effective area of 7.9 cm^2. Before the measurement, membranes were equilibrated with the corresponding solution (0.01 $mol \cdot L^{-1}$ and 0.5 $mol \cdot L^{-1}$ NaCl) for at least 24 h. On each end of the cell, two titanium mesh electrodes coated with iridium were used as working and counter electrodes; two silver/silver chloride electrodes were used as reference electrode and placed in Luggin capillaries at fixed positions near the membrane surface. Direct electrical current was applied to the system in a galvanostatic mode with six current steps using an Ivium potentiostat (Vortex®, Ivium Technologies, the Netherlands). Each step was maintained for at least 30 seconds to reach a stable reading. The measured current-voltage curve was used to obtain membrane resistance based on the slope of the curve [9]. Because the limiting current density is a function of solution concentration, I used different current steps for different solution concentrations. For 0.01 $mol \cdot L^{-1}$ solution, the maximum current density of 3.79 $A \cdot m^{-2}$ was achieved after six equal steps; for 0.017 mol·L^{-1} solution, the maximum current density was 7.59 A·m^{-2} in six steps; for 0.05 mol·L^{-1} and 0.1 mol·L^{-1} solutions, the maximum current density was 26.5 A·m^{-2} in six steps; and for 0.5 mol·L^{-1} solution, the maximum current density was 75.8 A·m^{-2} in six steps. The current density used was kept far below the limiting current density so that the current density effect was not obvious during the measurement except for the cases of 0.01 mol·L^{-1} and 0.017 mol·L^{-1} solutions. In these two situations, the current density ratio r reached 0.55. Three pieces of membranes of the same kind were measured as replicates in all following measurements.

5.4.3. Membrane resistance measured by varying current density using DC

To study the effect of applied current density on the resistance measurement, a method has been developed to measure the resistance at a certain applied current density instead of using the slope of I-V curve at different current densities. A similar method has been reported in the literature [114]. The resistance is derived from the potential drop after a single current jump. Sufficient time was allowed to reach a steady voltage state to reach the steady-state (Figure 14). Multiple steps were applied to obtain resistance under different current density ratios. In this approach, the resistance at a constant current density ratio can be obtained.

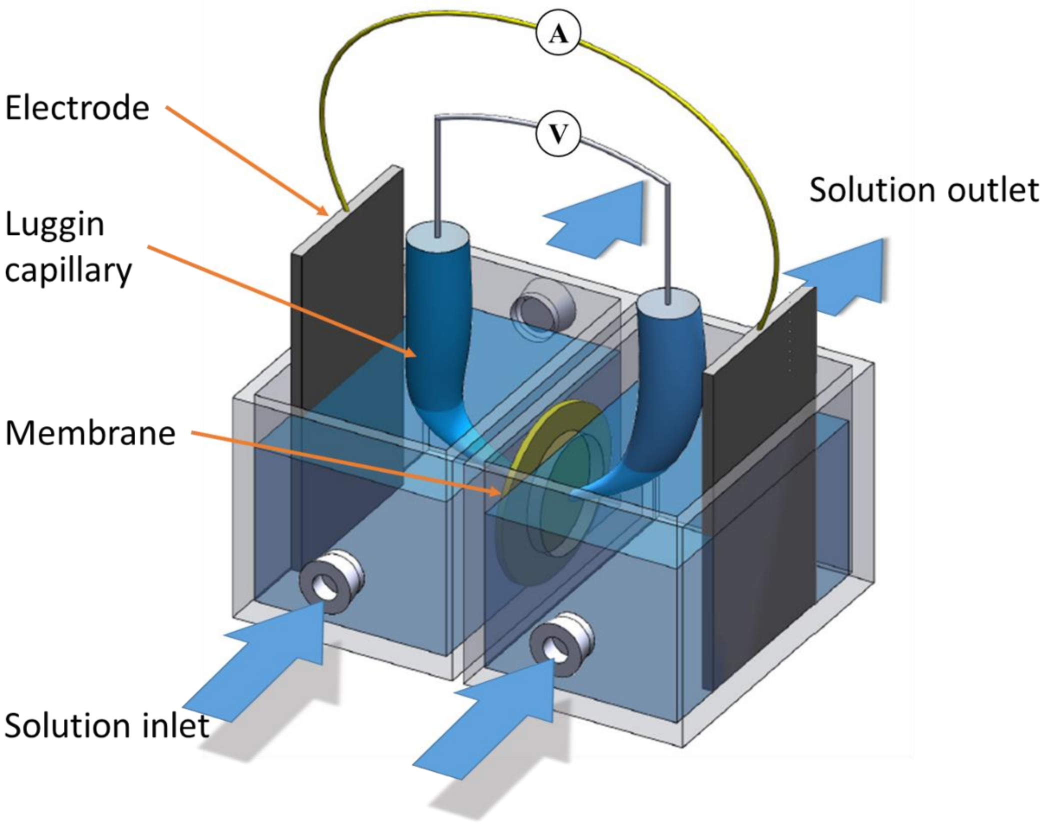

Figure 13 – Experimental setup for DC and AC measurements. Titanium electrodes coated with Iridium are pointed as ‘Electrode’; Ag/AgCl electrodes are placed in the ‘Luggin capillary’.

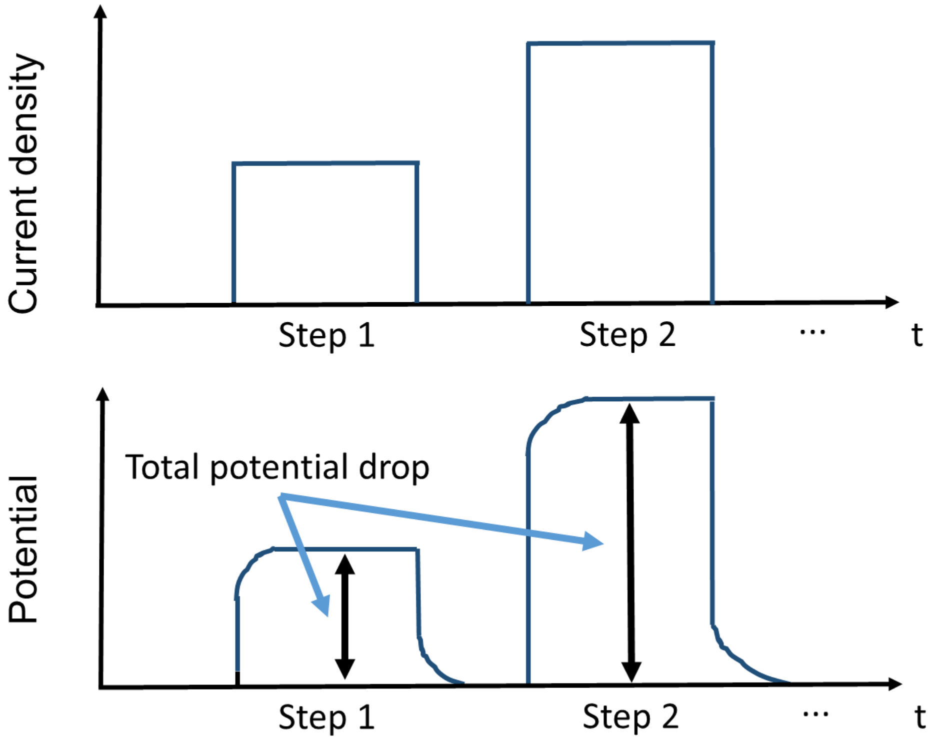

Figure 14 – Schematic representation of method used to study the effect of current density. Potentiostat controls the time and height of each current density step, and the total potential drop is measured until the steady state is reached. Used current density values depend on the limiting current density of each membrane to obtain different current density ratios *r*.

5.4.4. Membrane resistance measurement using AC

With the same setup, alternating current (AC) was applied to the system. Electrical impedance spectroscopy was used to analyze results based on the model. Applied frequency was set to 1000 Hz with five different current amplitudes from 1.8 $A{\cdot}m^{-2}$ to 35.5 $A{\cdot}m^{-2}$ with a step of 7 $A{\cdot}m^{-2}$. When the AC frequency was in this range, the membrane bulk resistance along with solution resistance was measured [12, 15, 21]. A following experiment without membrane was performed as a blank run. The pure membrane resistance was calculated as the difference between the impedances obtained in these two experiments.

5.4.5. Modelling methodology

The constants used in the model are listed in Table 7. The molar conductivity of NaCl is assumed to be constant in the concentration range discussed in this paper. The activity coefficients were calculated based on the Debye–Hückel equation and the Davies equation within their ranges of applicability, respectively. Simulation and graph generation were conducted using MATLAB® R2013a (MathWorks, Natick, MA, USA) and Microsoft Excel®. The area resistance is calculated based on Eq. 57. The NaCl concentration range is between 0.010 $mol{\cdot}L^{-1}$ and 0.500 $mol{\cdot}L^{-1}$ to fall within the conditions practically encountered during RED power generation. The temperature used in the calculation is assumed to be 298±1 K (25±1 °C). Membrane properties (except resistance) were taken as reported for frequently used IEMs in RED studies: CMX and AMX membranes were reported in the study by Dlugolecki *et al.* (2010) [11], and FKS cation and FAS anion (FuMA-Tech, Bietigheim-Bissingen, Germany) membrane properties along with SELEMION™ (AGC Engineering, Japan) according to manufacturer's specifications [115]. These properties are listed in Table 6.

Table 6 – Properties of Related Ion Exchange Membranes

	IEC (meq·g^{-1} dry membrane)	Permselectivity (%)	SD (%)	Thickness (µm)	References
FKS	1.47	98.3	33-41	20 - 63	
FAS	> 1	94.6	22-25	20 - 54	
CMX	1.64	92.5	21.5	181	[11]
AMX	1.30	91.0	16.4	138	[11]
SPPO	1.90	89.9	36.9	16 - 94	

Table 7 – Nomenclature in the model simulation

Parameter	Description	Value/Notes
$\boldsymbol{F}$	Faraday constant (s·A·mol^{-1})	96485
$\boldsymbol{R}$	Gas constant (J·mol·K^{-1})	8.314
$\boldsymbol{T}$	Temperature (K)	298
$\boldsymbol{\Lambda}$	Molar Conductivity of NaCl Solution (298 K) (S·m^2·mol^{-1})	0.01265 *
$\boldsymbol{\Delta t}$	Difference of transport numbers of sodium ion and chloride ion in water solution	-0.22 for CEM and 0.22 for AEM
$\boldsymbol{\delta}$	Thickness of DBL (m)	1.0E-3 (fit value from FKS membrane, used for other membranes)
$\boldsymbol{h}$	Thickness of membrane (m)	-
$\boldsymbol{D_{ct}^{m}}$	Diffusivity of counter ion in membrane phase (m^2·s^{-1})	-
$\boldsymbol{C_{fix}}$	Fixed charge density of membrane (eq.·L^{-1})	-
$\boldsymbol{M}$	Membrane property parameter (m^2·eq.·L^{-1}·s^{-1})	The product of $\boldsymbol{D_{ct}^{m}}$ and $\boldsymbol{C_{fix}}$
$\boldsymbol{i}$	Applied current density (A·m^{-2})	-
$\boldsymbol{i_{lim}}$	Limiting current density (A·m^{-2})	-
$\boldsymbol{r}$	Ratio of applied current density to limiting current density	Within the range of 0 to 1
$\boldsymbol{C_o}$	Bulk solution concentration (mol·L^{-1})	-
$\boldsymbol{\gamma}$	Activity coefficient	-
$\boldsymbol{R_L}$	Resistance due to the change of electrolyte concentration in diffusion boundary layer (Ω·m^2)	-
$\boldsymbol{R_d}$	Resistance due to diffusion potential formed in diffusion boundary layer (Ω·m^2)	-
$\boldsymbol{R_m^{DBL}}$	Resistance due to membrane potential formed across membrane (Ω·m^2)	-
$\boldsymbol{R_0}$	Measure membrane resistance (Ω·m^2)	-
$\boldsymbol{R_m}$	Membrane bulk resistance; assumed to be the AC measurement result (Ω·m^2)	-
$\boldsymbol{R_E}$	Experimental resistance result (before subtracting control run) (Ω·m^2)	-
$\boldsymbol{R_{BL}}$	Control run of resistance measurement (Ω·m^2)	-

5.5. Results and Discussion

5.5.1. Membrane resistance measured using AC

FKS, FAS, and SPPO membranes of different thicknesses were measured using the AC method. A linear relationship of area resistance to thickness is clearly illustrated in Figure 15. From Eq. 60, only the bulk resistance (term in value b) dominates when an alternating electrical field with high frequency (1000 Hz in this case) exists, because the polarization effect is not evident when there is no net migration of ions in any direction. Therefore, the membrane property parameter M (combined indicator of fixed charge density and interaction of counter-ions with membrane bulk material) is the only property that affects the membrane resistance. For a certain type of membranes (e.g., SPPO membrane made from the same batch of source material), M remains constant regardless of the thickness of the membrane. Consequently, the membrane resistance measured using the AC method should exhibit a linear relationship against the thickness of the membrane. The same assumption can be applied to commercial FKS and FAS membranes to evidence the observed phenomena. In Figure 15, the interceptions on the y axis are all relatively small (i.e., 0.09 for FKS, 0.07 for FAS, and 0.04 for SPPO). When the thickness of the membrane approaches zero, the bulk resistance is also approaching zero (Eq. 56). The slopes of these lines are different, indicating different membrane property parameters M.

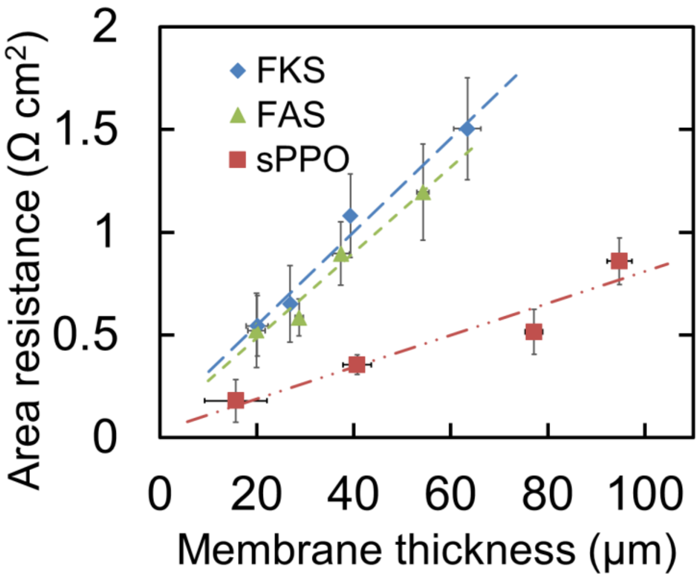

Figure 15 – Membrane resistance measured using AC against membrane thickness. For each kind of membrane, four different thicknesses were tested. Error bars show the 95% confidence interval of replicates during resistance and thickness measurements.

This linear relationship has been implied in the literature, but not specifically proved because different membrane properties were compared [39]. If the membrane property parameter (M) is constant with a given membrane material, thinner membranes should be advantageous as long as mechanical strength permits. However, as will be discussed later, resistance measured using AC without significant boundary layer effect presents the membrane bulk resistance and is, therefore, not a proper indicator of membrane resistance in a system with DC current flow. By using this AC resistance to represent membrane bulk resistance, term b in Eq. 60 can be further evaluated in DC studies.

5.5.2. External concentration effect

Membrane resistance was measured when the membrane was in contact with NaCl solution of different concentrations. The resistance obtained from AC studies was used as bulk resistance $\frac{hRT}{F^2M}$ (as in term b of Eq. 60) for each membrane. An optimized hydrodynamic parameter (DBL thickness δ) and current density ratio r were obtained from fitting FKS membrane measurement results as 1.0 mm and 0.54, respectively. Results were not significantly different if FAS or SPPO data was used as the fitting data (Appendix B). The current density ratio is relative to the limiting current density of FKS here. The current density ratio for different membrane varied with respect to different limiting current densities (Table 7). Therefore, even the current applied during the measurement was kept the same for different membrane, the resulting r values were different for different membranes. The same δ was used in all cases. As shown in Figure 16, simulation results using the model correlate well with experimental data for the FKS membrane, and the prediction matches well for FAS and SPPO data. The coefficients of variance (R^2) are 0.951, 0.938, and 0.998 for FKS, FAS, and SPPO membranes, respectively.

The assumption of the same DBL thickness for different membranes is appropriate because both the solution flow rate and the distance between the two Luggin capillaries were fixed in this study. Therefore, only the local flow pattern near the membrane surface would affect the hydrodynamic environment [110, 116]. Since the same testing cell was used in all experiments (Figure 13), local variations should not be a significant concern. The current density ratio r used in the simulation and prediction was well justified for low concentration situations (0.01 $mol \cdot L^{-1}$ and 0.017 $mol \cdot L^{-1}$) as the current density used during the measurement could reach over half of the limiting current density. According to Eq. 60, when the bulk solution concentration (C_0) increases, the effect of current density diminishes rapidly. In fact, the current density ratio r varying under 0.55 did not result in a significant difference of predicted resistance.

To further validate the model, the simulation of resistances was fit to data reported in Dlugolecki *et al*. (2010) for the commercially available CMX and AMX equilibrated in different concentrations of NaCl solution [11]. The simulation curves matched well with the measured resistances at various NaCl concentrations as seen in Figure 17. Note, however, that a different value of $r = 0.36$ (i/i_{lim}) (Eq. 41) was used for best fit. The difference in applied current density (i) is reasonable since the measuring current density does not exceed the limiting current density ($r < 1$) [10, 11]. The coefficients of variance (R^2) are 0.993 and 0.985 for CMX and AMX membrane fittings, respectively.

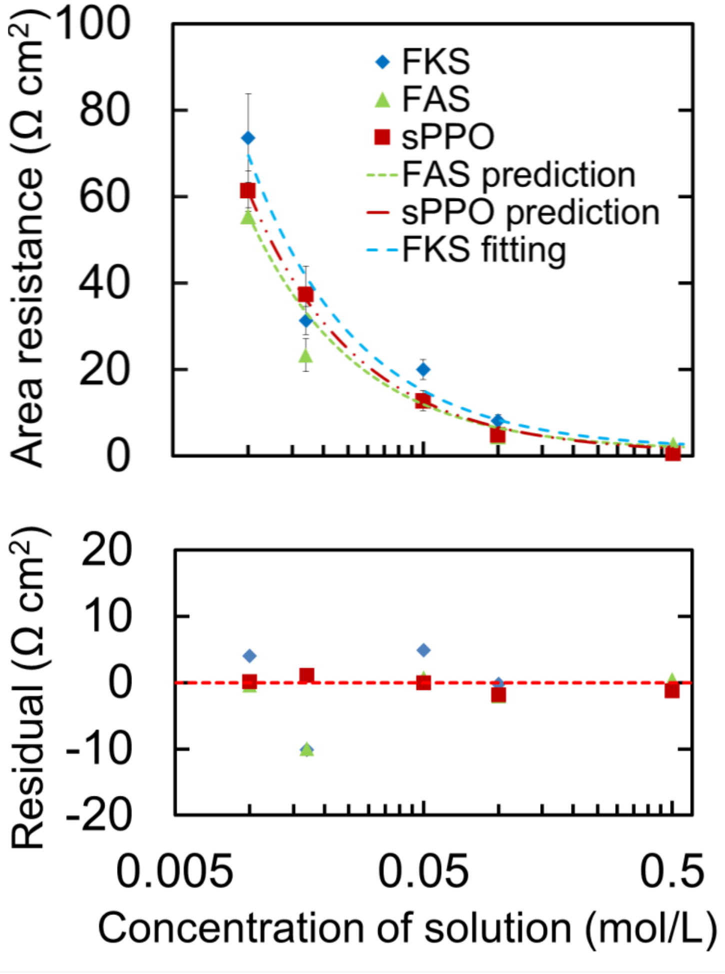

Figure 16 – Concentration dependency of the membrane resistance is measured using DC on FKS, FAS, and SPPO membranes. Simulation curve and experimental data are compared and residues are presented.

The increase of measured resistance along with the decrease of external solution concentration has also been shown in other studies. For example, in the model developed by Kim *et al*., (2013) [117], the membrane resistance has a linear relationship with the reciprocal of external solution concentration. Their model was not able to explain the situation when the membrane resistance plateaus at a certain level under sufficiently high salt concentration instead of approaching zero. On the other hand, the model presented in this work treats the term a in Eq. 60 containing $1/C_0$ as the term affected by external concentration, which decreases rapidly as the bulk concentration increases. However, the last term in Eq. 60, $\frac{hRT}{F^2M}$ (membrane bulk resistance) stays almost the same, which explains the plateaus. Galama *et al*. (2014) also fit the resistance trend using a similar form, but no physical meanings associated with the fitting parameters were proved [15].

The strength of the presented model lies on the prediction of apparent resistance of membrane when the current density varies. Obviously, the DBL thickness as an indicator of hydrodynamic environment and membrane property M and limiting current density in a given concentration have to be given as inputs. Generally, M may change according to external concentration. However, because of the Donnan equilibrium, the assumption that the counter-ion concentration in the membrane phase is relatively stable over a wide concentration range is valid, especially when the concentration concerned is significantly lower than the fixed charge density as shown in Eq. 53 [14].

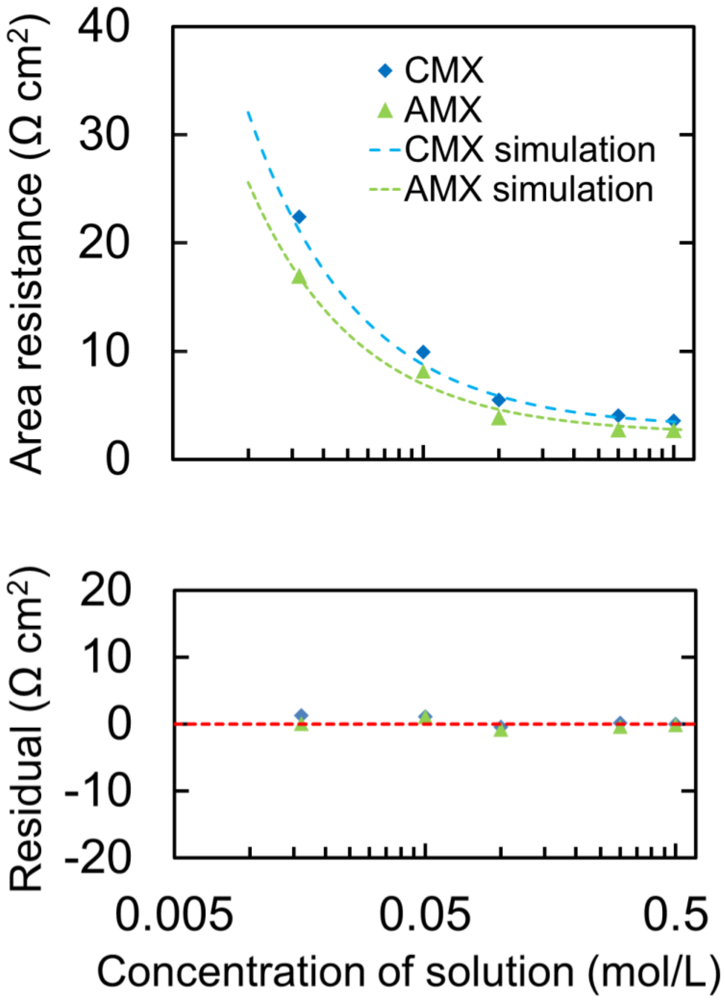

Figure 17 – Simulation of the concentration dependency of CMX and AMX membrane resistance compared to the data reported in [9]. Residues of the data to the model simulation values are also presented.

5.5.3. Current density and its effect on DC measurement

Membrane resistance measured using different current densities in 0.1 mol·L^{-1} NaCl solution are compared with the model prediction of resistance at different current densities in Figure 18. Using the same δ, the current density ratio r was calculated based on different limiting current densities for FKS and FAS membranes as measured in this study (Table 6). The model shows a relatively good prediction at r values studied with R^2 of 0.930 for FKS and 0.844 for FAS. Variation of resistance with respect to the r value showed an apparent increasing trend when higher r values were applied. As depicted in Eq. 60, current density applied to the system directly affects the concentration distribution within the DBL which alters the resistance of the DBL and results in a non-ohmic resistance.

Concentration polarization has been well studied, but the effect of applied current density on the membrane resistance measurement is rarely researched in literature [8, 10, 11, 105]. A common practice of resistance measurement applies DC at different current densities to a membrane equilibrated in a solution of certain concentrations [11, 13, 53]. Under this condition, even though the DBL thickness can be controlled hydrodynamically, the resistance resulting from the DBL would vary because different current densities are applied. The extent of concentration polarization under various current densities causes inaccuracies in the results in applications of ED and RED. Barragan and Ruiz-Bauza (1998) reported a model simulating the change in resistance due to the concentration polarization near the solution-membrane interface for ED application [25]. However, not all non-ohmic resistance was considered in their model, and the membrane bulk resistance was not associated with membrane properties. In an ED system, high current ratio situations are common. As indicated in this study, membrane resistance behavior is considerably different from measurements [27].

5.5.4. Implication to Membrane Synthesis and IEM Applications

Because of the dependency of resistance to membrane thickness, a high performance ion-exchange membrane should have the least thickness possible in a specific application, as long as the mechanical strength permits. Given a fixed membrane thickness, electrochemical properties characterized by M determines the resistance. However, as simulated in Figure 19, improvement of membrane properties can be easily diminished when the system is applied under low electrolyte concentration or at high current density ratio. The resistance from the DBLs, as a combination of resistance due to change of electrolyte concentration and resistance generated from diffusion potential and membrane potential, is more pronounced when the external solution concentration is lower, whereas the resistance of the membrane bulk stays the same over the full concentration range examined. Similarly, experimental data from RED stack design studies indicate that the diluted solution compartment contributes the most to the internal resistance [10, 45].

Therefore, improvement of performance for a system such as RED (usually concentration level of fresh water encountered) requires not only superb membrane properties, but also practical approaches to decreasing concentration polarization. In an ED system for desalination, the situation is even worse because the applied current density could easily be close to the limiting current density.

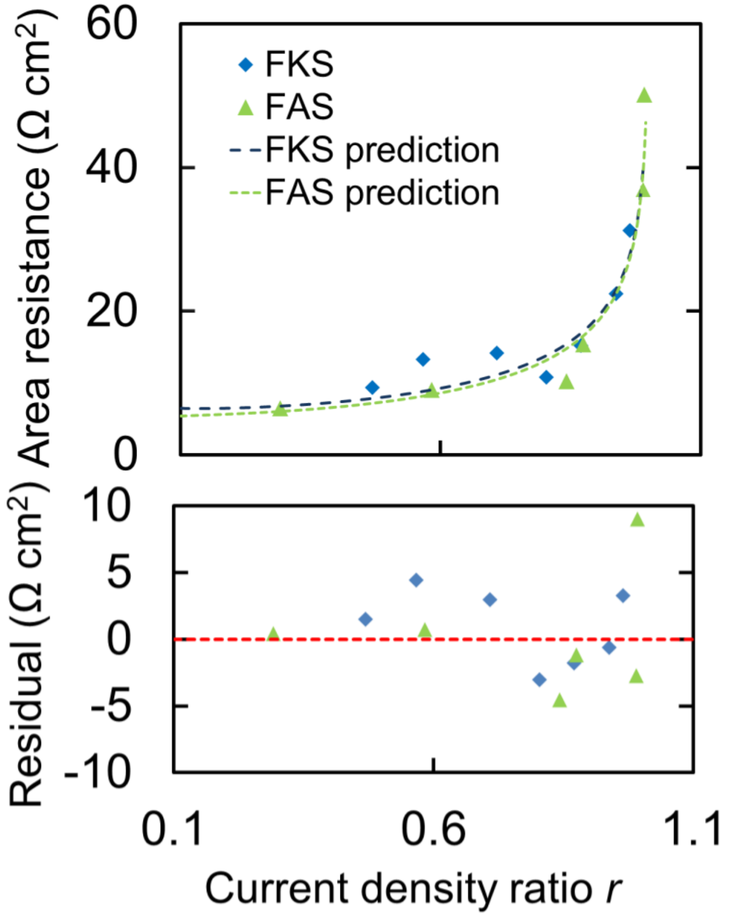

Figure 18 – The effect of applied current density on the measured membrane resistance. Predictive curve and experimental data are compared and residues are presented.

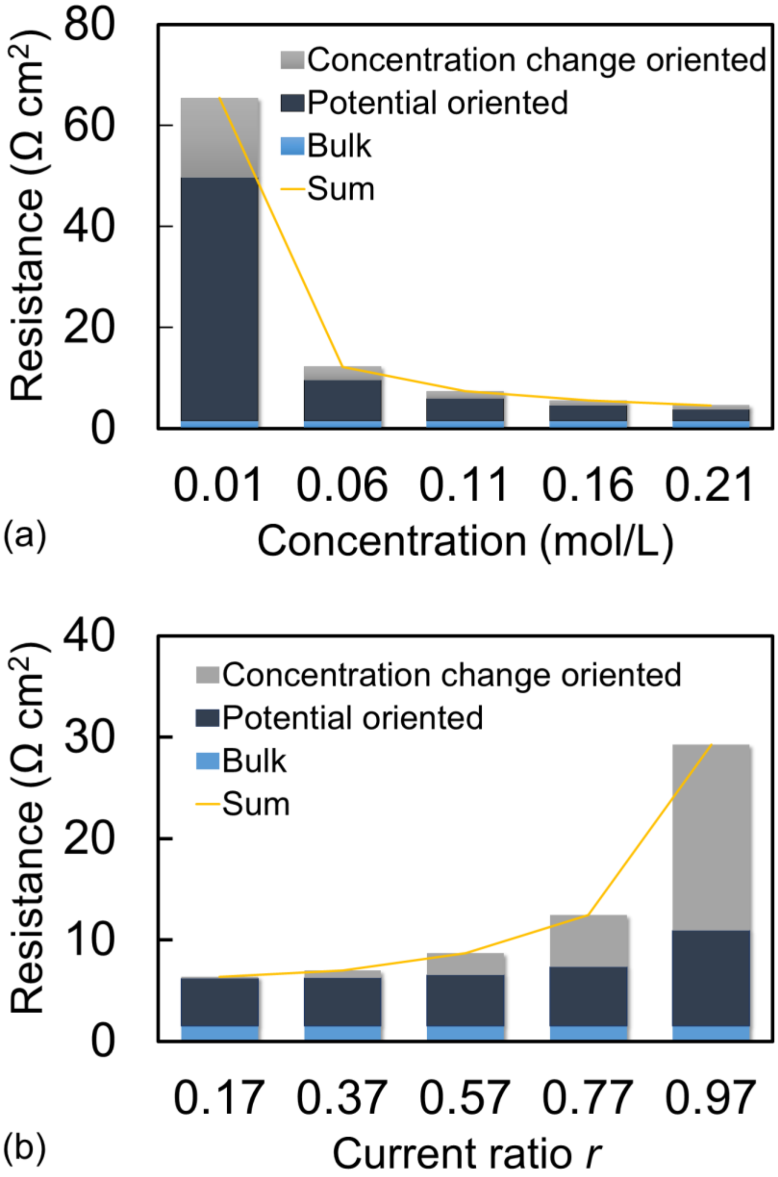

Figure 19 – Simulation of contributions to the apparent resistance of a FKS membrane. DBL thickness is set to 1.0 mm. "Bulk" denotes the resistance from membrane material (first term in Eq. 22c); "Concentration change oriented" denotes the resistance calculated from Eq. 22b; and "Potential oriented" denotes the resistance calculated from the second term in Eq. 22c. (a) With the same r = 0.5, the simulated membrane resistance in NaCl solution of a concentration varies from 0.01 mol·L^{-1} to 0.21 mol·L^{-1}. (b) With the same NaCl solution concentration of 0.1 mol·L^{-1}, the simulated membrane resistance when applied has a current density ratio that can vary from 0.17 to 0.97.

5.6. Conclusions

A model of internal ionic resistance in a RED system has been developed by considering the DBL and IEM bulk properties. The model explains the widely reported phenomena theoretically and verifies them with experimental and reported data. Prediction of membrane resistance matched well with experimental data on commercial FKS and FAS membranes, as well as in-house fabricated SPPO membranes.

The increase in membrane resistance in a solution with decreased concentration is well explained by the contribution of the DBL to the overall membrane resistance. The model also reveals a linear relationship between the measured membrane resistance and the reciprocal of the external solution concentration when using the DC method. Moreover, the model considers the influence of applied current density, which may affect the resistance of an IEM, especially when the salt concentration is relatively low (<0.1 mol·L^{-1}) and the applied current density is higher than 90% of the limiting current density ($r > 0.9$).

To the best of our knowledge, few studies have focused on quantifying the contributions of the DBL and membranes in terms of their ionic resistance with respect to the current density in a RED system. Using the model presented here, a practical estimation of the resistance of a RED stack is more realistic, and the resulting power density prediction may be more accurate.

CHAPTER 6. MECHANISM EXPLORATION OF ION TRANSPORT IN NANOCOMPOSITE CATION EXCHANGE MEMBRANES

Nanocomposite IEM is one type of nanostructured membrane fabricated by incorporating inorganic nanomaterials into polymer [118-123]. It has been reported that many nanocomposite IEMs have enhanced physicochemical and electrochemical properties comparing to their pristine counterparts [65, 124-129]. However, the origin of property enhancement of nanocomposite IEMs is far from being fully understood. Therefore, I present here a mechanism exploration of nanocomposite CEMs and simulation of nanoparticle behaviors upon aggregation within the polymer matrix to explain the observed transport phenomenon.

6.1. Abstract

By combining experimental work and computational modeling analysis, I study the influence of nanomaterials on the ion transport properties of nanocomposite CEMs. I synthesize and characterize a series of nanocomposite CEMs by using SPPO as polymer materials and silica NPs as nanomaterials. I observe that with the increase of the NP loading, the measured CEM permselectivity and swelling degree first increase and then decrease. Modeling analysis suggests that the change of membrane properties is related to the change of membrane micro-structure. With the addition of silica NPs, membrane porosity (volume fraction of inter gel phase) increases, so that membrane can absorb more water. Also, volume fraction of sulfonated polymer segments increases, which might allow

membrane to retain more counter-ions, and thus membrane IEC increases. By calculating the effective ion diffusion coefficients and membrane tortuosity factors of all the silica NP based CEMs that synthesized in this study, along with nanocomposite CEMs from other two studies, I conclude that membrane ion transport efficiency tends to increase with the incorporation of nanomaterials. In addition, a simulation model has been built to explain the membrane property change nanomaterial upon nanomaterial aggregation. The simulation results are in good agreement with the experimental data. According to the simulation results, membrane properties are related to nanomaterial number concentration in the membrane matrices; nanomaterial aggregation deteriorates the membrane performance by decreasing the nanomaterial real number concentration.

6.2. Introduction

As key components, IEMs largely influence the effectiveness and efficiency of RED system. Plenty of research has been conducted to optimize electrochemical system performance; but little research has focused on the desired properties IEMs and the important roles they can play in optimizing system performance. IEMs are ion containing polymer electrolytes, which can be classified as part of both cation exchange membranes (CEMs) and anion exchange membranes (AEMs). CEMs contain negatively charged functional groups, which allow the transport of cations but repel anions. Meanwhile, AEMs contain positively charged functional groups and have the inverse ability regrading ion permeation.

In order to get IEMs with desired performance, the nanoscale design of ion exchange channels has been extensively studied in recent years [123]. A nanocomposite

IEM is one type of nanostructured membrane, which incorporates inorganic nanomaterials into polymer materials [118-123]. It has been reported that many nanocomposite IEMs have enhanced physicochemical and electrochemical properties compared to their pristine counterparts [65, 124-129]. On the one hand, nanocomposite IEMs have superior overall electrochemical properties compared to the pristine polymeric membranes; on the other hand, they are also excellent candidates for solving problems in specific electrochemical systems.

Regarding the synthesis of nanocomposite CEMs, different synthesizing methods have been developed, among which the physical blending method and sol-gel method are most commonly used [118]. In physical blending, the prepared nanoparticles are dispersed into the polymer matrix by solution blending or melt blending, followed by the solidification of the membrane. This method is simple and easy to combine multi-components for hybrid formation. The polymeric solution and the nanofiller are independently prepared and then mixed. In this way, physical blending has good flexibility. Multiple types of polymers and nanofillers can be employed to make nanocomposite CEMs through this method. There exist no fussy restrictions on the use of certain polymers and nanofiller materials caused by physical and intrinsic properties such as chemical structure, composition, size, shape, etc. However, it is often challenging to have uniform distribution of nanoparticles on the polymeric matrix. In situation like this, the nanofillers tend to aggregate, leading to the uneven distribution of nanoparticles in the membrane matrix, change of membrane morphology and properties, and defects. The dosage of nanofillers needs to be carefully optimized to mitigate the aggregation problem and to ensure the best membrane performance. Sol-gel method is a classical *in situ* process to attach nanoparticles onto the polymeric membrane. The precursors of the desired nanoparticle are suspended in a solution that is deposited on the polymer substrate by coating, dipping, or spinning. Then the precursors condense into the nanoparticles through chemical reactions initiated by heating, addition of initiators, etc. Gel is formed in the condensation process. The main disadvantage of sol-gel method is the small range of available types of membrane materials, concentrating on silicon and metal materials. However, this method provides good dispersion of nanofillers in the membrane matrix, which brings better contact of nanoparticles and polymer than physical blending method does [118, 120].

Different hypotheses have been proposed to explain the origin of the property enhancement for nanocomposite IEMs. Many researchers think that the functionalized nanomaterials can introduce extra ion exchange functional groups, which act as additional ion exchange sites. With more active ion exchange sites present in membrane matrices, ion transport could be facilitated. Consequently, both the ion exchange capacity (IEC) and ionic (proton) conductivity increase, which means the ionic resistance decreases [65, 128, 130]. Other researchers claim that the nanomaterials will change the structure of the ion exchange membranes [121]; the addition of nanomaterials favors the formation of both continuous ion channel networks inside the membrane matrices and the interconnection of channels inside nanocomposite membranes [124]. Ion channels could also be formed at the interfaces of nanomaterials and polymer materials as a result of the interaction of those two [123]. The second hypothesis was tested by detecting membrane structures at the nanoscale level using electron microscopy techniques [131, 132]. Many unanswered (or only partially answered) questions remain, which prevent more detailed understanding of ion transport in nanocomposite CEMs. Our hypotheses are that the interactions among nanomaterials and polymers change the membrane micro scale structure upon the addition of nanomaterials; thus, the transport of ions could potentially be influenced by the membrane structure change.

Although it is widely recognized that membrane properties would be affected by the chosen materials as well as the selected fabrication method, I have found that a certain mechanism is followed regarding membrane property change when nanomaterials are added. A physical blending method was chosen to ensure the nanoparticle (NP) properties remain unchanged during the whole membrane fabrication process. Also, the physical blending method allowed analysis of the NPs before mixing with polymer solution. The influence of NP loadings on the membrane properties (IEC, permselectivity, swelling degree, and ionic resistance) was comprehensively investigated. In addition, numerical model analysis was conducted to quantify the membrane structure change and the influence on ion transport. The origin of membrane property enhancement was discussed and related to the change in membrane structure. Furthermore, a numerical simulation was used to quantify the influence of nanomaterial aggregation on the real number concentration of nanomaterial in the membrane matrices. The tendency of membrane ion transport efficiency to change after nanomaterial aggregation was also discussed.

6.3. Methods

6.3.1. Materials

Poly (2, 6-dimethyl-1, 4-phenyleneoxide) (PPO) (Aldrich, Mw 30000, Mn 20000) was used as the polymer material. Chloroform (Aldrich, anhydrous, 99%) was chosen for dissolving PPO. Silica (SiO_2, silicon dioxide) (US Research Nanomaterials, 99.5%) NPs with diameters of 15–20 nm was used as nanomaterial fillers. Chlorosulfuric acid (Aldrich, 98%) was applied for the sulfonation reactions. Glycidyl phenyl ether (GPE) and dimethyl sulfoxide (DMSO) (ACS grade, 99.9%) were obtained from Sigma-Aldrich and VWR, respectively.

6.3.2. Sulfonation of PPO

Sulfonation of PPO materials have been described in Section 5.4.1 and is re-stated here. 9.6 grams of PPO was dissolved into 100 mL of chloroform, and the solution was stirred for 1 hour. Further, 4.4 mL of chlorosulfonic acid dissolved in 50 mL of chloroform was slowly added into PPO solution while stirring. The precipitate was filtered and then washed several times with deionized (DI) water, until the pH became approximately neutral. The resulting SPPO was dissolved again into methanol, and the solution was then poured into a Pyrex glass tray to form a thin 1-2 mm layer. The layer was then air dried under a fume hood at room temperature for 48 hours. At last, the dried SPPO was cut into small pieces and kept for future use.

6.3.3. Fabrication of nanocomposite membranes

In this study, I synthesized and characterized nanocomposite CEMs using solution casting and phase inversion methods. Each batch of polymer solution was prepared by first dispersing silica NPs into 20 grams of DMSO, then dissolving 5 grams of SPPO into the suspension. Ultrasonic bath (B3500 A-MT, 50/ 60 Hz, VWR) was applied for obtaining well dispersed NP suspension. After SPPO was added, the solution was stirred for 48 hours at room temperature. The resulting polymer solution was cast on glass plate by using a doctor blade. Then the membrane together with glass plate were vacuumed in an oven at

50°C for 36 hours. The membrane was then peeled off from the glass plate. The peeled membrane was first soaked into 1 M of HCl solution for one day, and then stored in 0.5 M of NaCl solution for future characterization. All the synthesized membranes are listed in Table 8.

Table 8 – List of materials for synthesizing a series of nanocomposite CEMs

Name	Feeding NP loadings (wt %)	SPPO (g)	DMSO (g)
Membrane 1	−	5	20
Membrane 2	0.2	5	20
Membrane 3	0.5	5	20
Membrane 4	0.8	5	20
Membrane 5	1.0	5	20

6.3.4. Characterization of silica NPs and IEMs

Fourier transform infrared (FTIR) spectra of silica NPs and membrane samples were obtained by using a FTIR spectrometer (Digilab FTS 7000). SEM images were taken by a field emission scanning electron microscopy (FE-SEM, Hitachi SU8230). Energy dispersive X-ray spectroscopy (EDX) (Hitachi SU8230) was applied to get information about cross-sectional elemental information for chosen membrane samples. Atomic force microscope (AFM) (Agilent 5500, Agilent Technologies, Inc., US) was used to obtain the tapping mode phase images of wet membrane (in Na^+ form) surfaces. The membrane thickness was obtained by using a micrometer, and at least three measurements were conducted for each sample. For all these tests (except for those implemented to obtain AFM phase images), the membrane samples were dried in a vacuum oven at 50 °C for 24 hours.

The IEC of NPs and membrane samples was measured by a back titration method [99, 133]. Membrane swelling degree (SD), membrane porosity, apparent permselectivity, and membrane ionic resistance were also measured. All the measurements were conducted at least three times. A detailed description of membrane properties measurement procedures is listed in the Appendix C.1 Characterization of IEMs.

6.4. Model Development

6.4.1. Three-phase model and effective diffusion coefficient calculation

In the sulfonic acid group containing CEMs, the sulfonated polymer segments aggregate into ionic clusters, and randomly distribute inside the bulk inert polymer matrices. Counter-ions transport through the sulfonated hydrophilic ionic clusters in hydrated membranes, and co-ions are repelled. From a three-phase model point of view, a membrane can be treated as heterogeneous at the microscale [134, 135]. A total of four different membrane micro phases are considered: the inert polymer phase (non-sulfonated polymer segments), the polymer chain phase (sulfonated polymer segments), the active hydrated functional groups' phase, and the inter gel (neutral electrolyte solution) phase

[135, 136]. Also, Figure 20 shows a way of grouping different membrane phases based on the model [135]. Both the pure gel phase and neutral electrolyte solution (inter gel phase) are considered ionic conductive, but with different conductivities [135]. When dealing with nanocomposite membranes, the volume of nanomaterials is neglected, since it is extremely small compared with that of polymer materials. According to the micro-heterogeneous theory, the total membrane conductivity could be deduced as [134, 135]:

$$k_m = {k_{11}}^{f_{11}} {k_2}^{f_2} \tag{63}$$

where k_m is the membrane conductivity, f_{11} and f_2 are volume fractions of the pure gel phase and the electrolyte solution phase, respectively, and k_{11} and k_2 are conductivities of the pure gel phase and the electrolyte solution phase, respectively.

6.4.2. Ionic diffusivity and tortuosity of membrane

Further, to get insight into the ion transport process inside membranes, the Nernst-Einstein equation was applied to calculate the (effective) ionic diffusion coefficient by using membrane ionic conductivity data [137]:

$$D = \frac{\Lambda RT}{z^2 F^2} \tag{64}$$

where D is the ionic diffusion coefficient (in solution or in membrane)(mol·m^{-2}·s^{-1}), Λ is the molar conductivity (S·m^{-1}·mol^{-1}), R is the ideal gas constant, T is the temperature (K), z is the ion charge, and F is the Faraday constant (C·mol^{-1}). I employed D_{eff} to represent the effective ionic diffusion coefficient (mol·m^{-2}·s^{-1}) in membrane (and D the effective ionic diffusion coefficient in bulk solution).

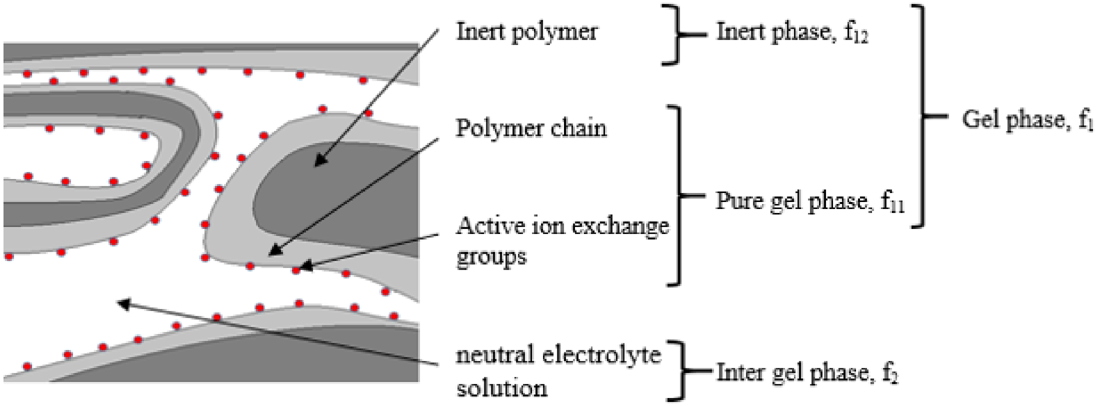

Figure 20 – Schematic illustration of micro phases of ion exchange membrane and grouping of membrane phases based on three-phase model.

In addition, to account for how the change of volume and the arrangement of different membrane phases influence ion transport, I introduced the apparent tortuosity factor (τ) [138]:

$$\tau = \frac{D_{eff}}{D} \times f_2 \tag{65}$$

where τ is a parameter that influences the transport path of ions. The value of τ should always be equal to or larger than 1, where the value 1 represents ions diffuse in bulk solution. As the value increases, ions diffuse through longer and more tortuous pathways, and ion transport efficiency decreases.

6.4.3. *Numerical simulation of nanomaterial aggregation effect*

To investigate the aggregation of NPs, a numerical simulation has been applied to explain the observed optimal NP loading. The concentration of NPs added to the casting solution needs to be estimated before being compared to the diffusivity. For large spherical nanoparticles, it can be assumed that the volume of the particle (V_p) is the overall volume of basic unit (V_{unit})

$$V_p = NV_{unit} \tag{66}$$

The number of basic unit in a particle is denoted N. If the diameter of nanoparticles (D_p: m) is deduced from TEM images, then, the and estimation of unit diameter (D_{unit}) is possible as, we have:

$$D_p = N^{1/3} D_{unit} \tag{67}$$

Therefore, the number of units (molecules) N in a nanoparticle is [139]:

$$N = \left(\frac{D_p}{D_{unit}}\right)^3 \tag{68}$$

For silica and iron oxide nanoparticles studied in the simulation, the molar weight is summarized in Table 9.

Table 9 – Characteristics of studied nanoparticles

Nanoparticles	Diameter (nm) of single unit	Molar weight ($g\cdot mol^{-1}$) of single unit	Molar weight of single nanoparticles	Reference
SiO_2 (17 nm)	0.342	60	4.05E+7	This study
SiO_2 (30 nm)	0.342	60	7.37E+6	[140]
SiO_2 (420 nm)	0.342	60	1.11E+11	[141]
SiO_2 (30 nm)	0.342	60	7.37E+6	[121]
Fe_2O_3 (30 nm)	0.830	160	7.56E+6	[99]

Assumedly, the effective diffusivity is determined by the number density concentration of nanoparticles incorporated into the polymer structure and the size of the nanocomposite structure:

$$D_{eff} = a + b \cdot \rho_n \tag{69}$$

The number density concentration of nanomaterial groups, ρ_n, is calculated as the nanomaterial numbers in each volume (m^{-3}); a and b here are fitting constants for linear regression. To obtain the true number of nanoparticle groups after the aggregation of individual particles, I also need to know the resulted number of groups given the number of nanoparticles I introduce to the casting solution. The characteristic relationship between the amount of nanoparticle added and the effective diffusivity can be simulated by a statistical model considering the aggregation of nanoparticles in the casting solution matrices.

The model assumes that at the micro-scale, Van der Waals force is the dominating form of interactions between nanoparticles [121, 141]. The interaction energies between two similar particles was can be calculated using van der Waals energy equation from DLVO theory expressed as:

$$V_A = -\frac{Aa_1a_2}{12h(a_1 + a_2)(1 + 11.12h/\lambda_c)} \tag{70}$$

where a_1 and a_2 are radius (m) of two nanoparticles, A is the Hamaker constant, nonetheless different from the value used in common aqueous environment. However, the constant is equivalently adjusted as the threshold energy is fit to experimental data as explained in the following: h is the distance between two surfaces of particles (m), λ_c is the character wavelength (taken as 100 nm generally) [121]. By applying the model, I can get pairwise binding energy of every two particles, assuming only two-body interactions. Because of high viscosity of casting solution, the nanoparticle groups would be stable after formation, especially considering the membrane forming after casting of blend solution on a glass plate surface. Therefore, formed groups will not dissociate into single particles. An energy cut-off threshold value has been chosen as a cutoff because the aggregation can only progress within a limited time before solvent evaporation which leads to the drying-out.

6.5. Results and Discussion

6.5.1. Nanocomposite membrane characterization

Surface SEM images of selected IEMs are shown in Figure 21. The pristine SPPO membrane (Figure 21 (a)) has smooth surface. The surface morphologies of nanocomposite membranes (Figure 21 (b)) are quite similar with that of the pristine SPPO membranes; however, obvious nanomaterial aggregations could be identified in membrane 3. The diameters of the largest aggregated particles exceed 1 μm.

Membrane thickness, IEC, SD, permselectivity and ionic resistance of all synthesized membranes are listed in Table 10. All the measurements were carried out at least three times, and the average values were recorded. Table 10 presents the IEC of all the synthesized membranes. The IEC of membranes first increases and then decreases with the incorporation of NPs. As the NP loadings increase, the IEC of membranes increases and reaches maximum values in Membranes 4 (2.20 $\text{meq}\cdot\text{g}^{-1}$); then, decreases as NP loadings continue to increase. The SD of synthesized membranes increases with the increase of NP loading. When NPs are first added, the SD has a sharp increase; as the loading becomes relatively high (above 0.5 wt%), there is only a small increment of SD with further adding of NPs. Compared with other membrane properties, the relatively large uncertainty (standard derivation) of the measurement might explain the weaker regularity of the SD data. The incorporation of NPs also affects membrane permselectivity with an optimal loading of 0.5 wt% NPs. By incorporating NPs, membrane ionic resistance sharply decreases, as shown in Figure 22 (A). The membrane intrinsic resistance (Figure 22 (B)), which is the membrane ionic resistance over membrane thickness [83, 142], shows a similar trend.

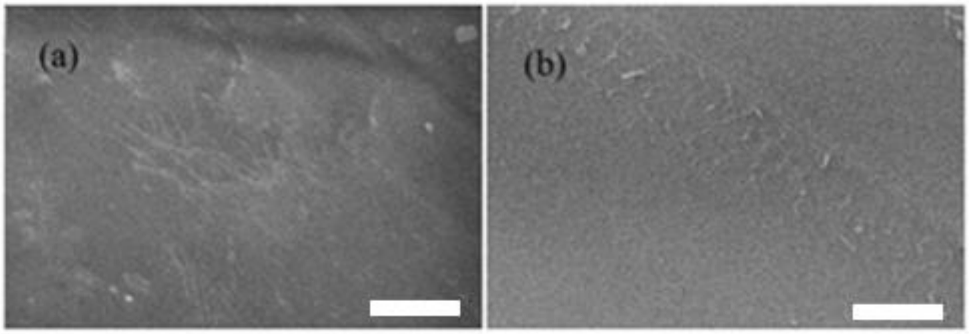

Figure 21 – Surface SEM images of (a) membrane 1, (b) membrane 3. The white scale bars at the bottom right are equal to 10 μm.

Table 10 – Properties of synthesized CEMs

Membranes	Thickness (μm)	IEC [meq·g dry]	SD [%]	Permselectivity [%]	Resistance [Ω·cm^2]
Membrane 1	78±6	1.76±0.07	34.4±8.9	87.4±0.8	1.38±0.09
Membrane 2	93±4	1.95±0.03	36.3±0.9	92.4±0.9	0.81±0.08
Membrane 3	98±2	1.93±0.05	42.0±1.4	92.3±0.8	0.84±0.04
Membrane 4	91±3	2.20±0.06	43.3±2.5	88.1±0.1	0.75±0.02
Membrane 5	88±4	1.85±0.01	49.3±1.3	80.0±1.8	0.81±0.16

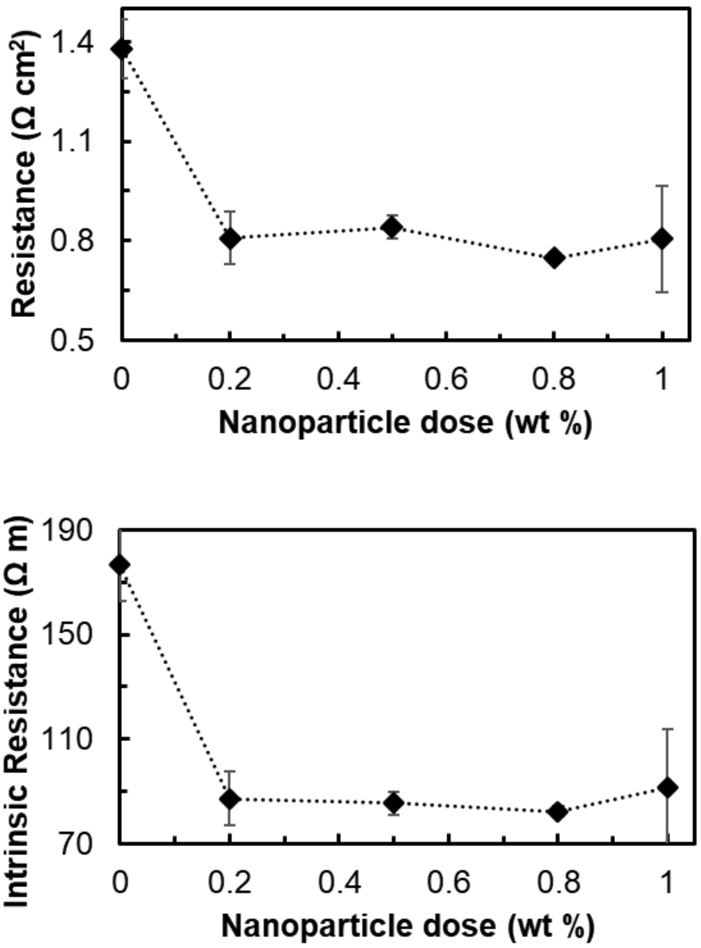

Figure 22 – Ionic resistance of nanocomposite CEMs with silica NPs (a); and the intrinsic resistance of nanocomposite CEMs (b) (error bars are ±1 standard deviations).

6.5.2. Three-phase model analysis of membrane conductivity

One possibility is that upon the addition of silica NPs, the membrane microscale structure becomes different from the pristine polymeric membrane; thus, the structure change influences the ion transport inside the membrane. To get information about structural properties of membranes, a three-phase model has been utilized [135, 136, 143]. First, membrane ionic resistance under different NaCl solution concentrations (from 0.01M to 0.1 M) was measured, then the measured ionic resistance was converted to ionic conductivity by:

$$k_m = \frac{d}{R} \tag{71}$$

where k_m is the membrane conductivity, d is the membrane thickness, and R is the membrane ionic resistance. To fit the model, a series of membrane conductivity measurements has been conducted within different concentration of NaCl solutions. The ionic conductivity values of all the synthesized membranes are listed in Table 14 in Appendix C.2 Membrane degree of sulfonation and conductivity. In order to get volume fractions of different phases, I established a simple linear regression model between ln k_m and ln k_2 [135], based on the relation in Eq. 72:

$$ln\, k_m = f_2\, lnk_2 + f_{11} lnk_{11} \tag{72}$$

Figure 23 presents a log-log plot of the relation between conductivities of electrolyte solution and membrane 1. According to Eq. 72, the slope of the fitted curve is the volume fraction of inter gel phase (f_2); the volume fraction of total gel phase (f_1) could also be obtained (f_1=1−f_2). Since the sulfonated polymer segments and unsulfonated polymer segments are distinct in terms of ion conduction, the polymer gel phase (f_1) could be further divided into two different phases: pure gel phase (f_{11}) and inert polymer phase (f_{12}). By calculating the degree of sulfonation (DS) of the polymer, the volume fractions of both phases can be obtained (Table 15 in Appendix C). Phase volume fractions of the other synthesized membranes can also be calculated by repeating the procedure. Theoretically, membrane pores are the space in membrane matrices that are not occupied by polymer chains (and nanomaterials); thus, they equal the volume fraction of neutral electrolyte solution upon hydration. Furthermore, by substituting membrane conductivity data into Eqs. 64 and 65, I could get insight into ion transport in membranes. The obtained effective ionic diffusion coefficient (presented as D_{eff}/D) and tortuosity factor (τ) reveal how effective the membranes can transport ions and how tortuous the membrane ion channels are, respectively. Since molar conductivity of ions (sodium ions in this case) in a membrane changes with the concentration [137], ionic conduction of 0.5 M sodium chloride was chosen to calculate the molar conductivity. All the calculated parameters are listed in Table 11.

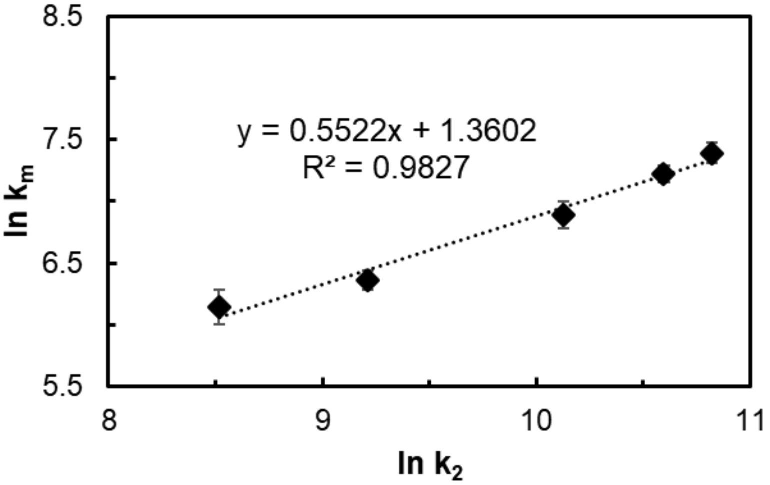

Figure 23 – Plot of log-log relation between conductivities of electrolyte solution and membrane 1 (error bars are ± 1 standard deviation)

Table 11 – Membrane structural and ion transport parameters

Membranes	f_1 [%]	f_2 [%]	f_{11} [%]	f_{12} [%]	D_{eff}/D	τ
Membrane 1	44.8	55.2	13.8	31.0	0.023±0.8	24.42±2.82
Membrane 2	40.1	59.9	13.5	26.6	0.046±0.8	13.04±2.15
Membrane 3	41.2	58.8	13.8	27.4	0.047±0.8	12.60±1.10
Membrane 4	36.8	63.2	13.8	23.0	0.049±0.8	13.02±0.66
Membrane 5	41.5	58.5	13.4	28.1	0.043±0.8	13.46±3.81

6.5.3. *Membrane micro-structure and ion transport*

Regarding different membrane phases, the change of volume fraction of membrane inter gel phase (f_2) has the same tendency as that of membrane IEC; Membranes 4, membrane with the highest IEC, also have the highest f_2 values. Inversely, as membrane IEC increases, volume fraction of gel phase (f_1) decreases. As the membrane SD increases with the increase of NP loading, it turns out that NPs help increase the membrane total volume by absorbing more water. As the total volume of water increases in the membrane, the volume fraction of the inter gel phase (f_2) also increases. When adding NPs, the volume fraction of the membrane gel phase (f_1) decreases, which can be explained by the NP-polymer interaction leading to a compression of polymer chain. However, NPs can affect different types of polymer chain segments in different ways: 1) sulfonated polymer chains can undergo swelling since the volume fraction of pure gel phase (f_{11}) remains almost unchanged for all the membranes, and membrane total volume increases by absorbing more water and 2) the unsulfonated polymer chains, which are the inert part of the polymer (f_{12}), can show a decrease in volume. Furthermore, the swelling of sulfonated polymer segments might explain the increase of membrane IEC: as the volume of hydrophilic polymer segments increase, ions (Na^+) could have more chances to interact with those segments and thus are easier to retain in the membrane matrices. The increase of membrane surface mean hydrophilicity might also attribute to the swelling of sulfonated polymer segments; thus, the volume increase of sulfonated part also affects the membrane surface hydrophilicity, since the density of the more hydrophilic sulfonated part also increases on or near the membrane surface. As a net effect of the membrane micro-structure change upon the addition of silica NPs, the effective ionic diffusion coefficient (represented as D_{eff}/D)

increased and the tortuosity factor (τ) decreased. Both parameters refer to ion transport efficiency in membranes by taking bulk solution as a reference.

6.5.4. Membrane ion transport properties upon nanomaterial aggregation

As discussed, optimal nanoparticle loadings exist for nanocomposite CEMs, beyond which no further increase of ion transport efficiency occurs. In this study, Membranes 5 showed decreased IEC and increased intrinsic resistance compared to Membranes 4, which indicates that Membranes 5 contain silica NPs that have exceeded or gone past the optimal loading point. As pointed out in previous studies [65, 133, 142], the existence of optimal loadings is related to the aggregation of NPs; hence, aggregation of nanomaterials severely influences the membrane micro-structure, and may even deteriorate membrane ion transport properties. The existence of an optimal loading implies a relationship between the intensity of nanomaterial aggregation and nanomaterial-polymer interaction. An explanation of the phenomenon can be established assuming:

1. Membrane ionic conductivity is linearly related to the number concentration of nanomaterials;

2. Aggregation of nanomaterials in the casting solution is irreversible during the process of membrane forming, and the aggregation driving force has a form similar to the van der Waals force of nanoparticles in aquatic environment [144].

Considering that when aggregation happens, the real number concentration of nanomaterials in the membrane is smaller than that added; thus, the nanomaterial aggregation diminishes the membrane ionic conductivity by decreasing the nanomaterial real number concentration. A simulation of membrane transport efficiency (as D_{eff}/D) against nanomaterial loading successfully reproduces the trend of observed membrane diffusion coefficient ratios in the experiments using silica nanoparticles. In Figure 24, all the experimental data are within two standard deviations of the model results. In the simulation, as the added nanomaterial concentration increases, nanomaterials have a higher chance to undergo aggregation (Supporting Information, S9). According to the simulation results, the plateau of D_{eff}/D is attributed to the aggregation of silica NPs. Although the added number concentration of silica NPs increases as the loading increases, the real number concentration does not increase proportionally because of aggregation at higher loadings. Iron oxide (100 µm) based nanocomposite CEMs [99] and silica (30 nm and 420 nm) [121, 141] based nanocomposite CEMs also show good accordance between experimental data and simulation results (Figure 24). In addition, the conclusion could also be extended to AEMs; a series of silica based AEMs [140] yielded similar results. The simulation algorithm is provided in detail in APPENDIX C. SUPPORTING INFORMATION FOR CHAPTER 5, C.3 Simulation Algorithm and Matlab Code.

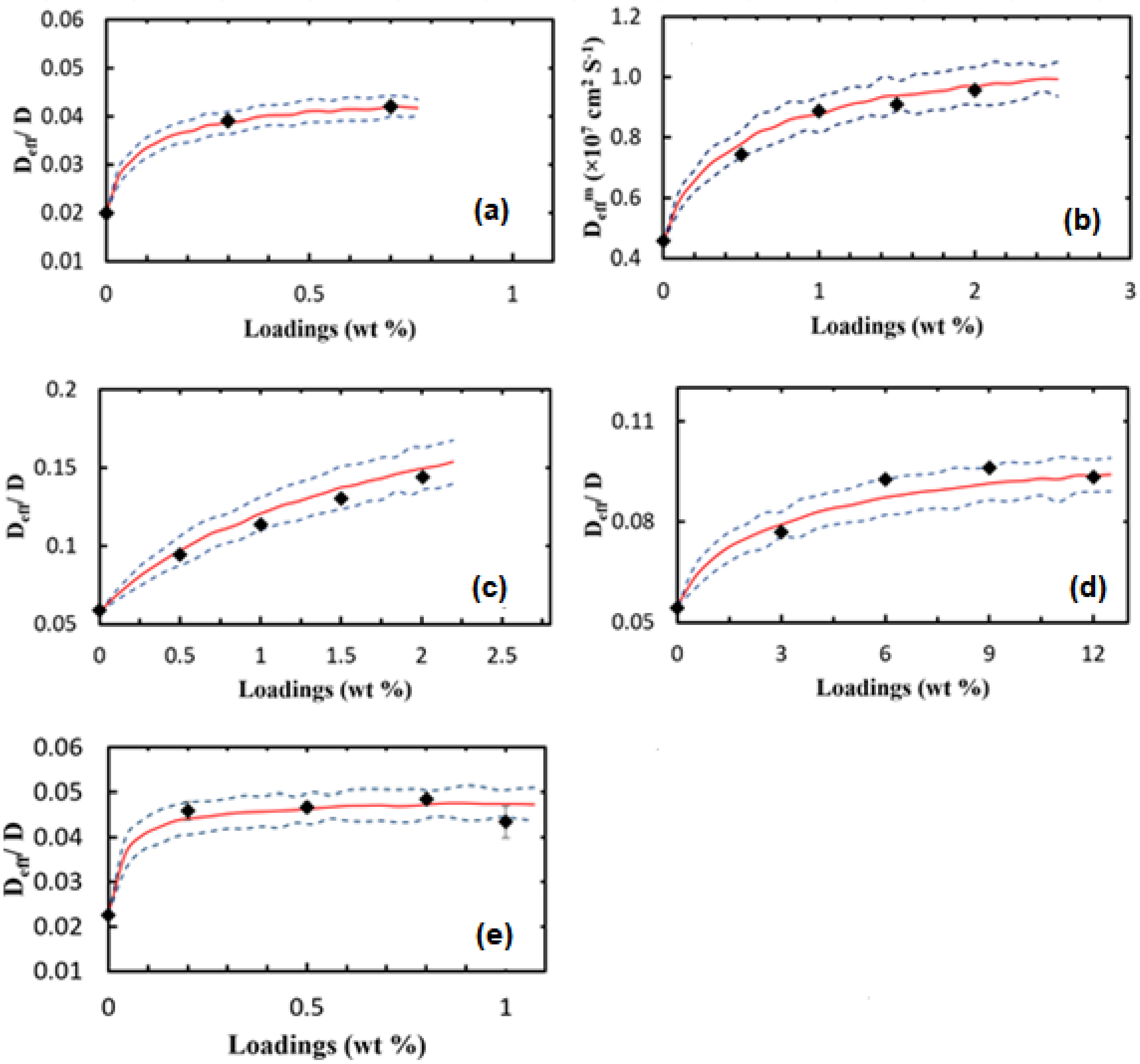

Figure 24 – (a) D_{eff}/ D of sulfonated iron oxide based, (b) D_{eff}^{m} of silica (30 nm) based (c) D_{eff}/ D of silica (30 nm) based, and (d) D_{eff}/ D of silica (420 nm) based, and (e) silica based (17 nm in this study) nanocomposite IEMs as function of loadings (black dots are the experimental results, red lines are the average values of simulation, and blue dash lines are two standard deviations ($\mu \pm 2\sigma$)).

6.6. Conclusions

Membrane micro-structure change and the influence on ion transport was explored for nanocomposite CEMs. A series of nanocomposite CEMs were synthesized by using SPPO as polymer material and silica NP as nanomaterial. SEM images indicated that the membrane surface morphology did not change much by adding silica NPs. Both membrane permselectivity and swelling degree (SD) first increased upon addition of silica NPs, then decreased when loading went beyond the optimal value. Membrane IEC and ionic resistance measurements showed that the enhancement of membrane properties also reached an optimal point with increasing NPs loadings.

By analyzing the measured data with a computational model, I found that the membrane property change is closely related to the change of membrane micro-structure. With the adding of silica NPs, the interaction between a NP and the polymer chain leads to an increase of membrane free volume (inter gel phase), allowing the membrane to absorb more water upon hydration. Also, at the presence of NPs, the sulfonated polymer segments tend to expand, while the unsulfonated segments tend to depress. The increase of sulfonated polymer segments (pure gel phase) volume might explain the increase of membrane IEC: Counter-ions have more opportunities to be trapped inside the membranes. The computational model revealed that, for both nanocomposite CEMs synthesized in this study, and nanocomposite CEMs from previous studies [99, 142], the effective ion diffusion coefficient increased and the membrane tortuosity factor decreased after adding nanomaterials. Generally, by the incorporation of nanomaterials, ion transport inside CEMs becomes more efficient. Nanomaterials with different shapes and/or surface functionality have different nanomaterial and polymer interactions, and influence membrane structure and properties differently, but they all increase membrane ion transport efficiency. The developed simulation model can explain membrane property change upon nanomaterial aggregation. Based on the simulation results, I determined that membrane ion transport property increases with the increase of nanomaterial number concentration, and the membrane ion transport performance reaches a plateau since the increase of nanomaterial real number concentration is influenced by aggregation. The results of this study can contribute to the value of future designs of new nanocomposite IEMs.

CHAPTER 7. PERCOLATION SIMULATION STUDY OF MASS TRANSPORT IN ION EXCHANGE MEMBRANES

7.1. Abstract

Two of the most important membrane properties, ionic conductivity and permselectivity, can be successfully modelled on a set of SPPO membranes prepared using NMP as solvent. The resulting simulation can provide good agreement with experimental observations. Especially, the decrease in permselectivity upon decreasing membrane thickness has been explained by the model considering combined effects resulting from water uptake and the percolation states of the lattice structure. Using open- and closed-sites to represent the polymeric phase and the interstitial electrolyte phases within the membrane matrix, simulation can also provide structural information for membrane conductivity analysis.

7.2. Introduction

The core components for membrane-dependent techniques such as electrodialysis, reverse electrodialysis (RED), flow batteries, etc. are ion exchange membranes. The IEMs have been intensely investigated to achieve desired membrane performance in the above-mentioned processes [4, 11, 24, 145]. Membrane performance is determined by the physicochemical (e.g. thickness, water content and hydrophilicity) and electrochemical properties (e.g. permselectivity, area resistance, and ion exchange capacity (IEC)) of the membrane. Among these properties, permselectivity and area resistance have emerged as two essential ion transport properties [67, 146].

Not surprisingly, these key membrane properties are inherently related to the microstructure of IEMs. Typical IEMs consist of a polymeric matrix impregnated with negatively charged or positively charged functional groups. Such a charged membrane has traditionally been treated as a micro-heterogeneous system consisting of three phases (i.e. a hydrophobic inert polymer, an active ion exchange zone, and an interstitial zone) [134, 135]. The ionic conductivity of a membrane is mainly governed by the active ion exchange phase and the interstitial phase, whereas the permselectivity is related to the relative transport number of counter- and co-ions. Many studies have focused on membrane conductivity [147, 148]. However, an interesting phenomenon resulting in lower permselectivities in thin-film IEMs or swelling membranes have remained not well understood [28].

Modern percolation theory has been widely used in modeling continuous macroscopic objects. Randomly distributed sites or bonds are studied in their two- or three-dimensional connectivity. If different types of sites in the percolation lattice represent different phases in the membrane matrix, a natural combination of the three-phase model with percolation theory emerges, and in fact, has been reported in the study of IEMs [135, 143]. These studies focused primarily on the percolative behavior of membrane conductivity: when conductive site ratio in the lattice surpasses a threshold, the membrane conductivity dramatically changes. However, plentiful structural information implied by percolation modeling is often omitted or untraceable.

In this study, computational simulation of the percolation lattice has been implemented and therefore, the structural information generated was able to be retrieved and analyzed. Multiple experimental trials based on the Monte Carlo approach ensured statistically valid results. With the aid of simulation, various parameters involved in membrane transport phenomena can be obtained. From this perspective, membrane transport properties are modelled to both explain the mechanisms of observed trends in conductivity and permselectivity with respect to membrane thickness and water uptake.

7.3. Model Development

7.3.1. Three-phase model

I have visited the three-phase model in Section 6.4.1, but re-stated, it is a theoretical approach to model IEMs emphasizing different phases within the membrane matrix. Assuming a typical polymeric IEM, one would find the micro-structure can be categorized into three regions: 1) active functional sites on the surface composed of polymer chains (pure-gel phase, f_{11}); 2) gel-resin regions consisting of polymer molecular backbones that do not have contact with electrolyte (inert phase, f_{12}); and 3) electroneutral electrolyte solution, filling the voids between the polymer backbones (inter-gel phase, f_2) (Figure 20) [134, 135]. The pure-gel phase and inert phase can be collectively assigned as f_1. In the case of SPPO CEM, the pure gel phase is mapped to the functionalized SO_3^- groups on the PPO polymer backbones. Applying this model, several transport properties of the membrane can be derived. Because membrane permselectivity and conductivity in a salt solution is of concern, I will focus only on these two properties.

The membrane permselectivity is defined as the ratio of the flux of counter-ions to the total ionic flux (i.e. current density) through the membrane under a given driving force. This driving force can be either salinity gradient or electrical potential gradient. In the case of permselectivity measurement, salinity gradient (0.1 M to 0.5 M NaCl solution) is the driving force. Therefore, the transport number of counter-ions and co-ions of a CEM (mainly cations) must have the relationship in Eq. 73 [134]:

$$\frac{t_+}{t_-} = \frac{A_1 J_+^G + A_2 J_+^S}{A_1 J_-^G + A_2 J_-^S} \tag{73}$$

where *J* indicates flux (mol·m^{-2}·s^{-1}); superscript *G* denotes gel-phase (f_1) parameters, and *S* denotes the electrolyte phase filling the interstitial voids within the membrane matrix (f_2); *A* denotes cross-sectional area of different phases on the membrane surface; positive (+) and negative (-) signs denote counter-ion and co-ion, respectively. Substituting the definition of flux as seen in a similar format in Eq. 47 and following the same derivation through to Eq. 51, we have:

$$\frac{t_+}{t_-} = \frac{A_1 D_+^G c_+^G + A_2 D_+^S c_+^S}{A_1 D_-^G c_-^G + A_2 D_-^S c_-^S} \tag{74}$$

where *D* and *c* denote the diffusivity and concentration of different ions in different phases, respectively. Ion valence has been omitted assuming I use sodium chloride as the model electrolyte with a 1:1 charge ratio. Then, an approximation is made that leakage of co-ions is mainly through interstitial electrolyte (f_2), because of significantly lower concentration of co-ions on the inter-gel phase surface. Therefore, Eq. 74 can be simplified.

$$\frac{t_+}{t_-} = \frac{A_1 \frac{D_+^G c_+^G}{D_-^S c_-^S} + A_2 \frac{D_+^S c_+^S}{D_-^S c_-^S}}{A_2} \tag{75}$$

Furthermore, in the NaCl solution of concern in this study, I can assume

$$D_+^s c_+^s \cong D_-^s c_-^s \tag{76}$$

Also, considering the definition of permselectivity (P) and the relationship between counter-ion and co-ion

$$P = 2t_+ - 1 \tag{77}$$

$$t_+ + t_- = 1 \tag{78}$$

Then, I have determined a linear relationship between the reciprocal of permselectivity and surface area of different phases as in Eq. 79.

$$\frac{1}{P} \cong \frac{2D_-^s c_-^s}{D_+^G c_+^G} \cdot \frac{A_2}{A_1} + 1 \tag{79}$$

7.3.2. Percolation theory and simulation

Percolation theory originates from the study of flow through porous media [149]. Mathematically, given a lattice of side length, *L*, let randomly chosen sites be of conductivity, *b* (or open) with a probability, *p*. Accordingly, the probability of a site having conductivity of *a* (or closed) is 1 - *p*. If *b* >> *a*, the observed system conductivity characteristics change abruptly (or an infinite connected cluster appears) when *p* is larger than a critical threshold. A similar definition applies to opening the bond of adjacent lattice cells, namely “bond” percolation. In this research, however, I am limited to study the “site” percolation problem only. In the context of ion transport through the membrane, the percolation threshold is a statistically defined minimum fraction of open volume (or ratio of sites open), to allow for the desired transport. Table 12 summarizes percolation thresholds from other studies.

There is another interesting property arising from percolation theory. If I define percolation as occurring when a connection of upper- and bottom-layer sites exists, then, the number of sites on the length and width dimensions is also essential in determining the threshold [150]. As seen in Figure 25, the threshold increases with increasing lattice thickness. This property renders variations in membrane phase distribution near the threshold. Because the sharp increase of percolation probability would result in trivial solutions (i.e. no matter what thickness of lattice, a small change in open site probability near the threshold would result in either all sites belonging to the percolate cluster or no percolation at all).

Table 12 – Reported percolation threshold from literature

Dimensionality	**Bond**	**Site**	**References**
2D squares	0.500	0.593	[151]
3D cubes	0.249	0.312	[150, 152]

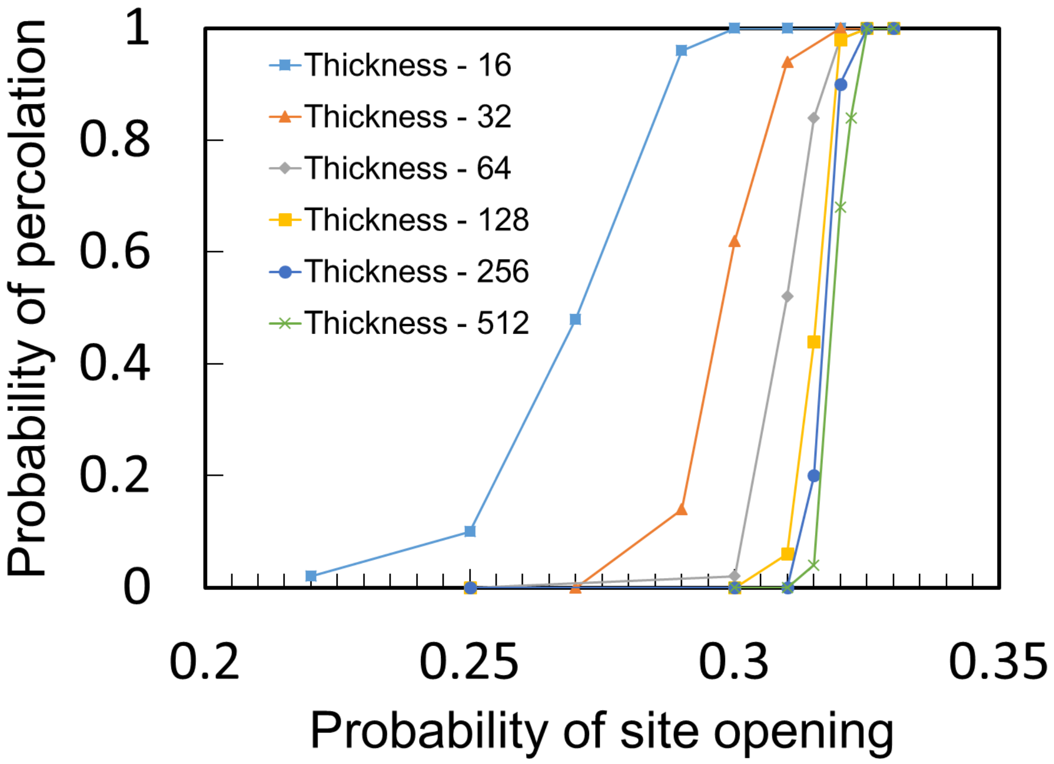

Figure 25 – Simulation of percolation probability as a function of lattice thickness. In the studied lattice, width and length are set to 64, but the thickness varies from 16 to 512. The threshold moves from 0.22 to 0.31, close to the theoretical value of infinite lattice size.

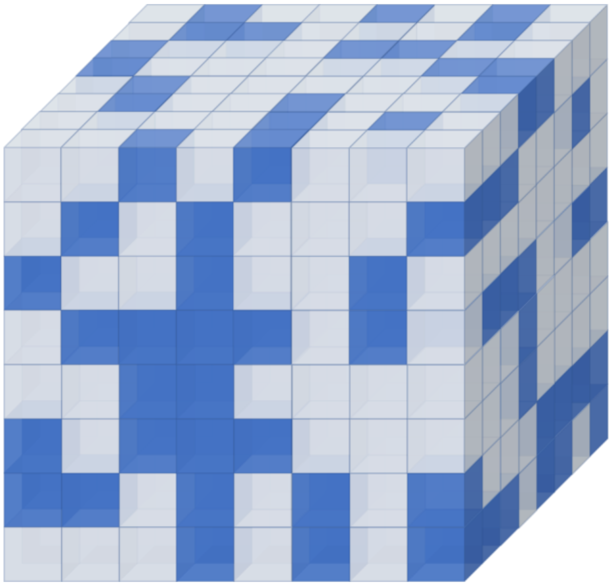

Figure 26 – Schematic of a 3-D lattice for the study of site percolation. Blue sites are defined as open sites and blank sites are closed to ion transport, so total volume of blues sites is the inter-gel phase volume.

Percolation theory is used not only to study the transport behavior of membranes near the threshold, but also to simulate the distribution of gel- (f_1) and inter-gel phases (f_2). The spatial distribution of sites provides additional information that can be used to derive membrane properties in combination with the three-phase model. For example, the surface area of the membrane (i.e. upper and lower layer of the 3-D lattice) that are part of percolation clusters can be obtained from the simulation. Therefore, area calculations with Eq. 79 are made possible.

Moreover, detailed differentiation of site- and cluster-type is also enabled. For example, there are randomly distributed sites or clusters that make contact with upper or lower surfaces, but are not part of the percolated clusters (i.e. “dead ends”). There exist also inert open sites surrounded by closed sites that are usually counted toward f_2 in conventional percolation studies. Because transport properties are of concern in this study, these differentiations are reflected in the simulation and are treated accordingly. In the permselectivity analysis, because a percolating cluster is assumed to enable ion transport, only open sites on both surfaces belonging to percolating clusters were counted towards A_2. However, in the conductance analysis, alternating current was applied. Then, explicit calculation of conductance is made possible by considering the in-series connection of sites in the depth dimension and in-parallel conducting pathways in the other two dimensions.

7.3.3. Simulation methodology

Simulation of 3-D lattice has been implemented in Java (jdk1.8.0_141) on IntelliJ IDEA 2017.2.3 on a personal computer with 16 GB memory and Intel i7 – 6700HQ processor. A three-dimensional multi-layer of cubes are generated with all sites set to closed initially. To model the membrane, the depth dimension was explicitly layered in accordance with real sample thickness with 1 cube representing 15 nm x 15 nm x 15 nm of volume. Due to limitations in computational capacity, periodic boundary conditions were applied on the width and length dimensions with 128 sites representing each dimension. Simple algorithm implementation of sets unification and testing operation were efficient in processing open- or close-site information (source code in Appendix D). A Monte Carlo approach was adopted to tackle statistical variation among different experiments. At least 100 simulations were run representing different slices of membrane pillars and reflecting the effect of average percolation probability over the larger membrane area. Randomly selected sites were opened until desired open site number was reached. The resulting open and closed sites represent a membrane layer with electrolytes as open sites and inert phase (polymeric backbone) as closed sites. In addition to spatial information, the number of sites that were in the cluster connecting upper and lower surfaces was also obtained and considered as inter-gel phase. Conductance of the membrane was also calculated based on the conductance of each single site.

7.4. Experiments

7.4.1. Materials

Poly (2, 6-dimethyl-1, 4-phenyleneoxide) (PPO) (Aldrich, Mw 30000, Mn 20000) was used as the polymer material. Chloroform (Aldrich, anhydrous, 99%) was chosen for dissolving PPO. Chlorosulfuric acid (Aldrich, 98%) was applied for the sulfonation reactions. N-Methyl-2-pyrrolidone (NMP) (ACS grade, 99.9%) were obtained from VWR.

7.4.2. Membrane preparation

Sulfonation of PPO materials have been described in Section 5.4.1 and is re-stated here for convenience. 9.6 grams of PPO was dissolved into 100 mL of chloroform, and the solution was stirred for 1 hour. Next, 4.4 mL of chlorosulfonic acid was dissolved in 50 mL of chloroform and was slowly added into the PPO solution while stirring. The precipitate was filtered and washed several times with deionized (DI) water, until the pH became approximately neutral. The resulting SPPO was again dissolved into methanol, and the solution was then poured into a Pyrex glass tray to form a thin 1-2 mm layer. The layer was then air-dried under a fume hood at room temperature for 48 hours. Finally, the dried SPPO was cut into small pieces and retained for future use.

Next, solution casting and phase inversion methods were used to synthesize SPPO CEMs. Each batch of polymer solution was prepared by dissolving 5 grams of SPPO into 12.5 g NMP. The solution was stirred for 48 hours at room temperature. The resulting polymer solution was cast onto a glass plate by use of a doctor's blade with precise control of thickness. Then, the casted membranes were dried in a vacuum oven at 50°C for 36 hours together with the glass plate. While the membrane was still on the glass plate, a direct contact with 1 M HCl solution facilitated removal. Soaking in HCl solution lasted for a day, then the membrane sheets were stored in 0.5 M NaCl solution for future use.

7.4.3. Membrane characterization

The experimental setup and membrane measurement procedures (i.e. swelling degree, apparent permselectivity, and conductance (reciprocal of area resistance) using AC) have been described in Appendix C.1. and Section 5.4.4, respectively. The membrane apparent permselectivity was measured using a static potential method with at least three replicates [65, 142]. For the conductance measurement, resistance readings at AC frequency 1000 Hz and amplitude of 1.8 A·m^{-2} was used with at least 6 replicates.

7.5. Results and Discussion

7.5.1. Model validation

The simulation of 3D percolation lattice has been validated on different cubic lattice of side lengths *L* from 32, 64, 128, and 256. The critical probability obtained was 0.311 ± 0.002, which matched well with literature.

Table 13 – Variation of membrane apparent permselectivity with thickness

Membrane thickness (μm)	Apparent permselectivity (%)	Water uptake (%)	Membrane conductance (S cm^{-2})	Simulated percolated surface area ratio	Simulated non-percolated surface area
12.9	71.5	0.507	11.3	0.481	0.519
23.1	86.1	0.332	6.69	0.113	0.887
34.0	88.1	0.326	-	0.084	0.916
45.0	94.8	0.320	3.22	0.015	0.984
58.9	95.3	0.320	2.22	0.004	0.996

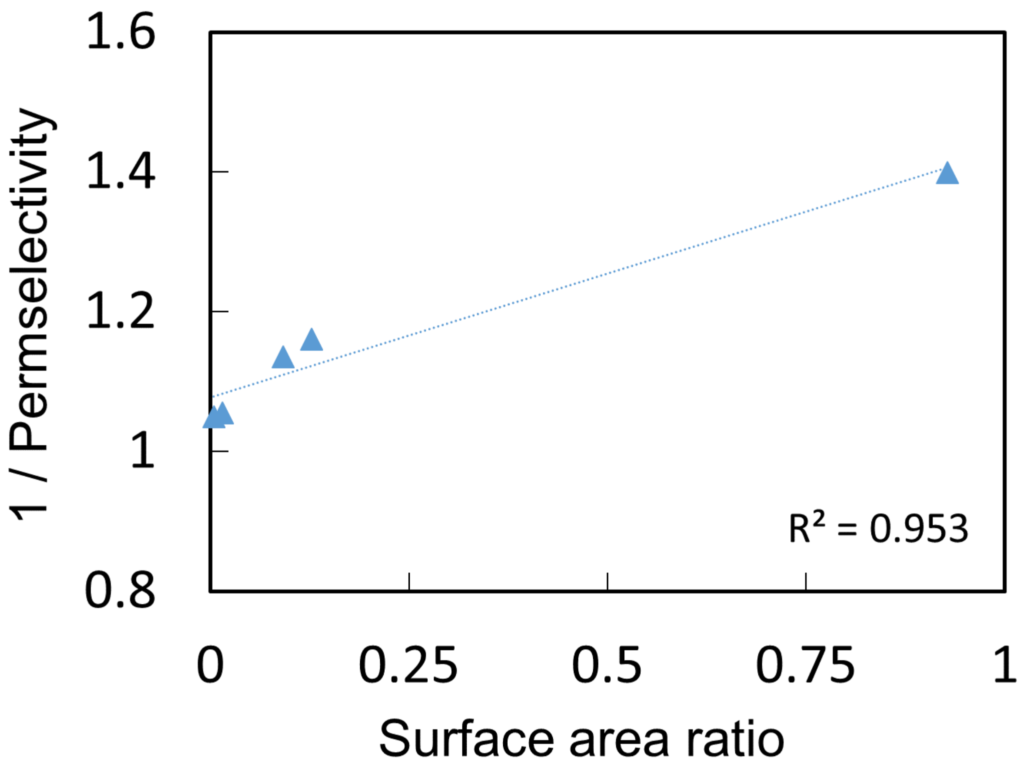

Figure 27 – As derived in Eq. 79, a linear relationship of the reciprocal of membrane permselectivity as measured and simulated surface area ratio based on water uptake of membranes of different thickness. The surface area ratio is defined as the ratio of the number of sites in percolating clusters to the number of sites in the rest of the surface.

7.5.2. Simulation of the effect of membrane thickness on permselectivity

The permselectivity of membranes with various thickness and swelling degree was measured. Plotting the inverse of permselectivity against surface area ratio (Figure 27) has revealed a linear trend as predicted in Eq. 79. The surface area ratio is defined as the ratio of number of sites in percolating clusters to the number of sites on the rest of the surface as derived in Eq. 79. The water uptake was used as the ratio of open sites in the simulation [28]. Note that in Table 13, water uptake alone is not able to explain the drop in permselectivity of thinner membranes. The water uptake of thicker membranes was slightly higher than than 3-D infinite site percolation threshold, therefore, in this range, the membrane thickness played a role in determining the number of percolated site on the surface as illustrated in the simulation results (Figure 25). From this result, the observed permselectivity variation is well explained as percolative cluster pathways through the membrane surface change along with changes in water uptake and membrane thickness. As water uptake increases over the percolation threshold significantly, the effect of different membrane thickness does not respond to the same degree as when water uptake is near the percolation threshold.

7.5.3. Membrane conductance and thickness

Using the same set of thickness and water uptake data, the simulated membrane conductance was fit to the experimentally measured data. Total membrane conductivity was explicitly calculated using two different conductivities of two types of sites, and applying conductance-in-series along the depth dimension and conductance-in-parallel along the length and width dimensions. Good agreement has been achieved by comparing conductance measurement as shown in Figure 28. This result is also in agreement with theoretical derivations from previous studies (Eq. 56 in CHAPTER 4).

One may notice that the membrane resistance (the reciprocal of conductance) varied almost linearly with membrane thickness. However, a slight change of slope was observed due to changes in water uptake (i.e. the number ratio of different types of sites). A significantly different conductivity of two site types contributed to this effect. Note that this effect was not affected by percolation states as much as those seen in the permselectivity case - when close to the percolation threshold, water uptake created a significant change in percolated site number. In the case of conductance measurements, because I have used AC, even ion transport pathways are not manifested through the membrane thickness, because alternating potential drives ions to migrate locally. So, both totally enwrapped inert sites as well as “dead end” sites (i.e. sites connecting both membrane surfaces but not thorough), contributed to the conductance from interstitial electrolytes. Therefore, abrupt changes due to percolation states were not as pronounced.

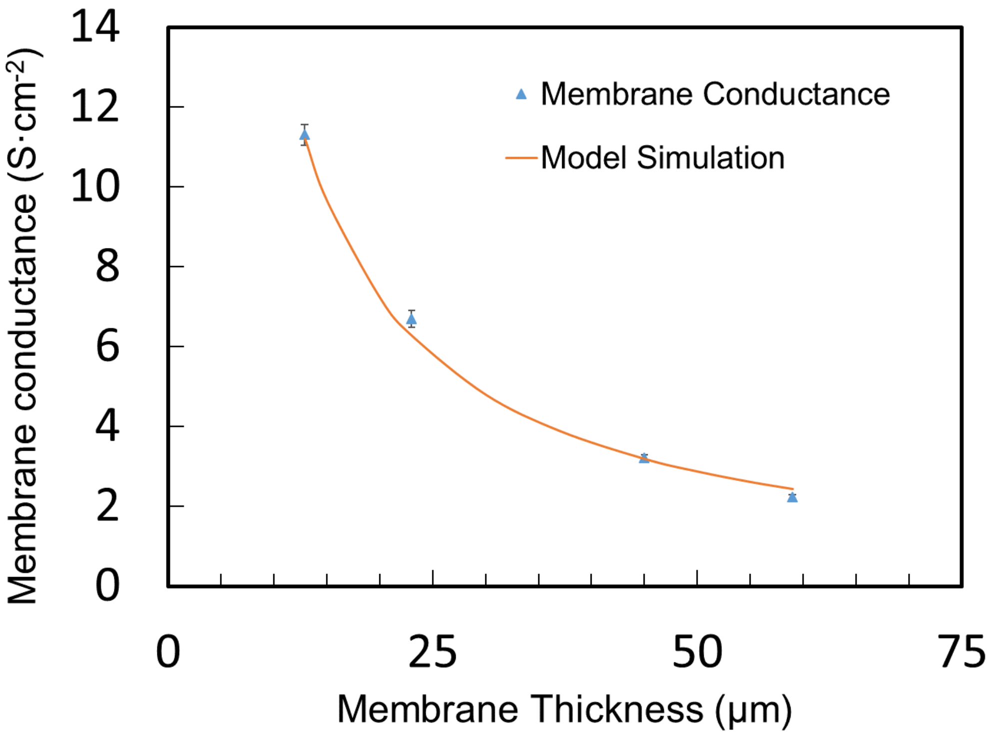

Figure 28 – Membrane conductance as a function of thickness. The orange line is the simulation fitting value from the model.

7.6. Conclusion

Two of the most important membrane properties, ionic conductivity and permselectivity, have been successfully modelled on a set of SPPO membranes of varying thickness. The membrane matrix was analyzed as a simple 3-D cube lattice. Combining the three-phase model and percolation properties of the lattice, the graduate loss of permselectivity was well explained and validated by experimental data. In addition, membrane conductance can be fitted with spatial information from simulation to appropriately describe conductivity in different phases. With the help of simulation and modeling results, a deeper understanding of membrane permselectivity and conductance will facilitate future membrane synthesis.

CHAPTER 8. MAJOR CONCLUSIONS AND FUTURE WORK

8.1. Major Conclusions

The key conclusions from my study are:

- Membrane properties of concern in RED applications have been refined to two key optimization parameters: 1) the overall ionic conductance, and 2) stack electrical potential from accumulated membrane potential.
- The conductivity of the dilute compartments in a RED stack has been significantly improved by using IERB to replace conventional non-conductive spacer materials. Gross and net power density were improved by as high as 75% compared to a regular stack. IERB filling was also proven to mitigate the concentration polarization effect.
- A model of internal ionic resistance in a RED system has been developed by considering the DBL and IEM bulk properties, and validated with experimental and reported data. A well-observed but less explained phenomenon, that the measured membrane resistance increases with decreased solution concentration, is well explained by the contribution of the DBL to the overall membrane resistance. Moreover, the model considers the influence of applied current density, which may affect the resistance of an IEM, especially when the salt concentration is relatively low ($<0.1\ \text{mol}\cdot\text{L}^{-1}$) and the applied current density is higher than 90% of the limiting current density ($r > 0.9$).
- Membrane micro-structural changes and their influence on ion transport was explored for nanocomposite CEMs. By analyzing the measured data with a

computational three-phase model, I found that the membrane property change is closely related to the change of membrane microstructure. With the addition of silica NPs, the interaction between a NP and the polymer chain leads to an increase in membrane free volume (inter gel phase), and ion transport inside CEMs becomes more efficient. The developed simulation model can explain membrane property changes upon nanomaterial aggregation. Based on the simulation results, I determined that membrane ion transport increases with the increase of nanomaterial number concentration, and the membrane ion transport performance reaches a plateau since the increase of nanomaterial real number concentration is influenced by aggregation.

- With the help of a statistical model of membrane microstructure combining the three-phase model and percolation theory, the dependency of membrane permselectivity has been successfully simulated and explained. Modeling results were an extension of previous model studies and validated by experimental data. With the computational simulation, other membrane properties such as conductance are also explicitly computable.

8.2. Future Work

Based on the current conclusions from studies, future work to advance the understanding of ion exchange membrane and the development of RED system in salinity gradient power generation may include the following:

- Further development of statistical simulation and modeling approaches to study ion exchange membrane properties and the effect of ion exchange material in ion transport. Powerful computational simulation enables more direct analysis of physical and chemical membrane properties considering the complexity of the system. Not only can the membrane matrix be modeled this way, ion exchange resin packed columns can also be modeled this way.

- Development of ion exchange membranes with well-balanced properties. Using model and simulation results, the trade-off between membrane ionic conductivity and permselectivity can be controlled and predicted to fit the best power generation efficiency in RED systems.
- Expansion of applicability of modeling and simulation results to other related fields. Many fundamental modeling frameworks and simulations are generic, and therefore applicable to similar systems using ion exchange membrane or ion exchange materials as components.

APPENDIX A. SUPPORTING INFORMATION FOR CHAPTER 3

This appendix provides supporting information for CHAPTER 4 - ENHANCED IONIC CONDUCTIVITY AND POWER GENERATION USING ION EXCHANGE RESIN BEADS IN A REVERSE ELECTRODIALYSIS STACK.

A.1 Measurement of Void Ratio and Density of Ion Exchange Resin Beads and Glass Beads

The void ratio was estimated to provide an indirect hydrodynamic characterization of resin bed in the application of this study. The bulk density and true density of ion exchange resin in bead form was estimated following the procedure as described in Bai and Li, 2006 [153]. Resin beads were fully hydrated and rid of excess moisture. Absorption of water within the resin material was not measured, as the porous properties of the bulk structure is not within the scope of this study. Only the voids between resin beads in a packed bed were measured. The void ratio was then calculated using equation:

$$n = 1 - \frac{\rho_b}{\rho} \tag{80}$$

where n is the void ratio (dimensionless); ρ_b is the bulk density ($g \cdot mL^{-1}$) and ρ is the true density of resin beads.

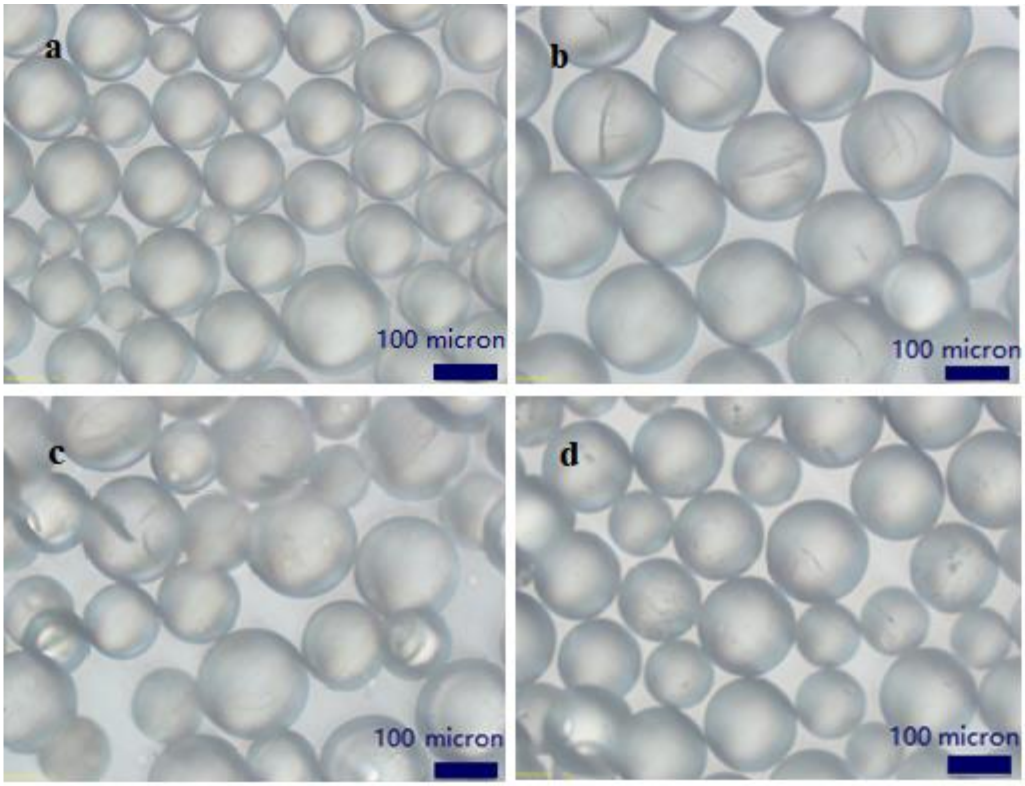

Figure 29 – Microscopic images of (a) cation exchange resin; (b) anion exchange resin; (c) equal-weight mixture of cation and anion exchange resin; (d) glass beads.

A.2 Measurement of Membrane Resistance and Permselectivity

Membrane resistance was measured using a DC method as described in literature [10]. Membranes were stocked in 0.5 M NaCl solution. Before measurement, membranes were transferred to a customer-built two-compartment measuring cell (Figure 13). Each compartment of the cell had a volume of 200 mL. Membrane area in contact with solution was 7.9 cm^2. Two customer-made Harber-Luggin capillaries were positioned close to membrane surface with a distance of 3.0 mm between two tips. Two Ag/AgCl electrodes (HI 5311, Hanna Instruments, US) were used as reference electrodes submerged in 3.0 M KCl solution in the capillaries to measure the potential drop across the membrane. Two plates of titanium electrode coated with iridium served as working and counter electrodes connected with an Ivium potentiostat (Vortex, Ivium Technologies, The Netherlands) to complete a four-electrode system. Before the measurement, the membrane was in equilibrium with NaCl solutions of required concentration on both sides for at least 100 minutes. For the measurement with a salinity gradient across the membrane (0.017 M NaCl on one side and 0.5 M NaCl on the other side), solutions were refreshed constantly for 100 minutes at a flow rate of 10 $mL\cdot min^{-1}$. During the measurement, the potential drop was recorded as a function of current density swept from 0 $A\cdot m^{-2}$ to 17.92 $A\cdot m^{-2}$. The area resistance of membrane was determined as the slope of the potential versus current density chart. Solution resistance without membrane in between as a blank run was subtracted to obtain the final resistance value. For the case with a salinity gradient across the membrane, the blank resistance was calculated based on the sum of one half of the 0.017 M NaCl solution resistance and one half of the 0.5 M NaCl solution resistance. Average value from three replicates was reported as membrane resistance.

Permselectivity of membranes were measured using a similar cell. The potential across membrane was measured when the salinity gradient was over 0.1 M to 0.5 M NaCl solutions. Details of this methodology has been reported in literature [65].

A.3 Measurement of Power Density and Stack Resistance

Power density measurement was carried out in a four-electrode system as shown in Figure 30. In these case, two titanium mesh electrodes integrated with the electrodialysis stack (Module FT-ED40, Fumatech, Germany) served as working and counter electrodes at both ends of the stack, while two silver wires (GF02315247, 99.99%, Aldrich) were used as reference and sense electrodes placed at end compartments between the two titanium mesh electrodes.

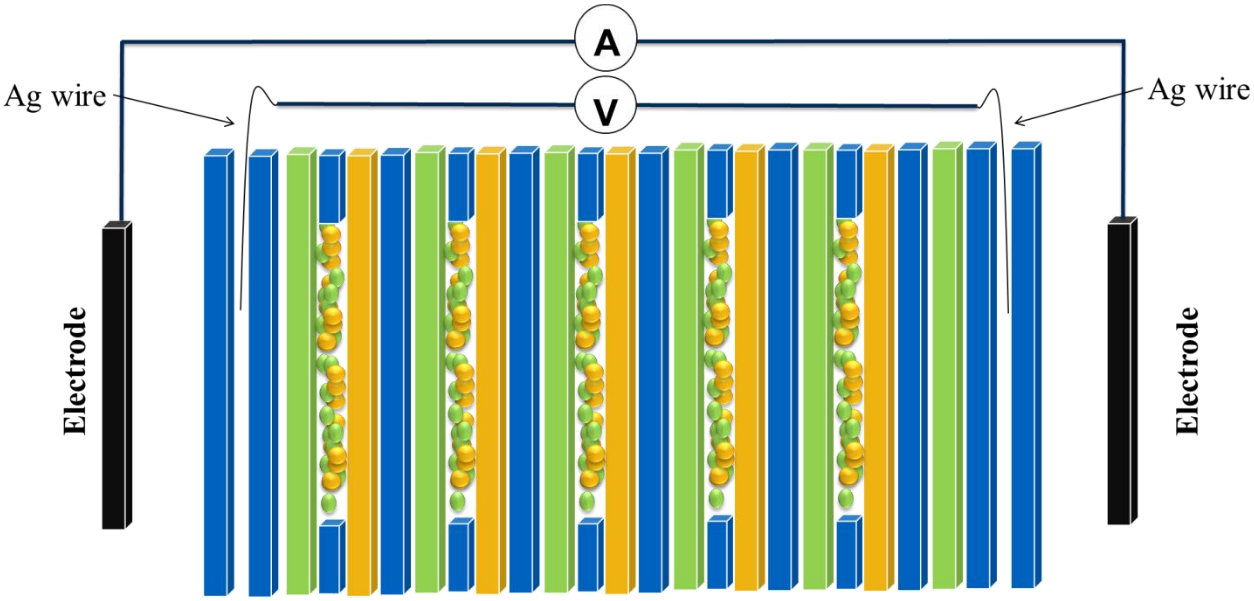

Figure 30 – Schematic representing the setup for power density and stack resistance measurement.

During the measurement, current density increased from 0 $A\cdot m^{-2}$ to 17.92 $A\cdot m^{-2}$ in 44 steps. In each step, the potentiostat maintained the current density for 15 seconds and took four potential measurements. Average potential values at each current level were plotted against the current density. The slope of the linear regression line was recorded as the ohmic stack resistance under direct current as shown in Figure 31a. The resulting voltage-current curves were used to calculate their product as power as shown in Figure 31b. The same measurement was conducted on a stack with only one cation-exchange membrane serving as a background value and was subtracted later [34]. The maximum product of voltage and current (adjusted after background run) was divided by all membrane area used in a stack and reported as the maximum gross power density.

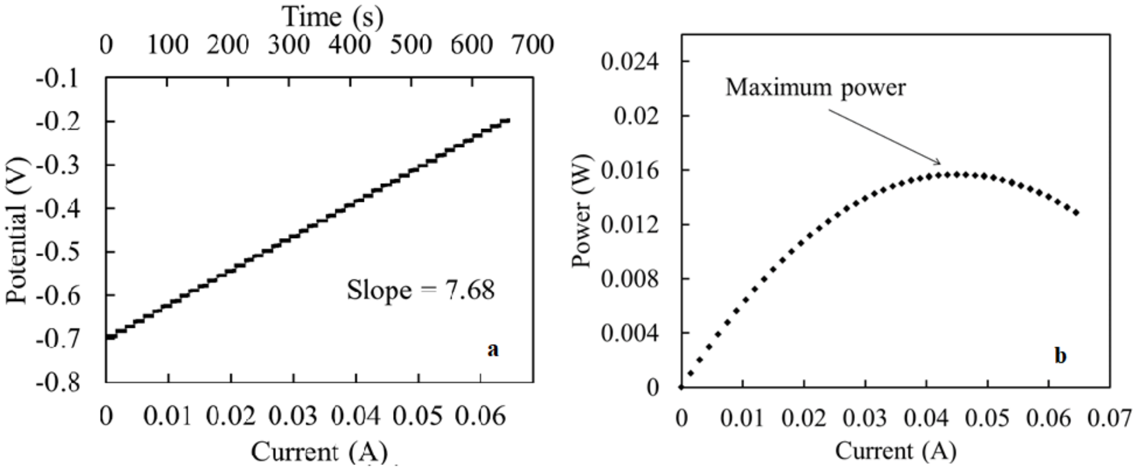

Figure 31 – (a) Representative data of stack resistance measurement. The negative value of measured potential only indicates polarity. (b) Representative data of power density measurement.

APPENDIX B. SUPPORTING INFORMATION FOR CHAPTER 4

This appendix provides supporting information for CHAPTER 5 - MECHANISM EXPLORATION OF ION TRANSPORT IN NANOCOMPOSITE CATION EXCHANGE MEMBRANES

FKS data were chosen to fit because of a relatively high variance of data points. If FAS or SPPO were used to fit the parameters, results were not significantly different but the correlation of corresponding fitting membrane would be better. If I fit using FAS, the error for FAS data would be less than the error from predictions made using parameters fit from other membranes. The figures using FAS and SPPO as fitting membranes are shown in the Supporting Information for your reference.

In Figure 32, using data of FAS resistance for fitting, the FKS and SPPO membrane resistance are predicted by the model. Concentration dependency of the membrane resistance is measured using DC on FKS, FAS, and SPPO membranes. Simulation curve and experimental data are compared and residues are presented. Current ratio is $r = 0.30$ of FAS limiting current density, and DBL thickness δ is 1.2 mm.

In Figure 33, using data of SPPO resistance for fitting, the FKS and SPPO membrane resistance are predicted by the model. Concentration dependency of the membrane resistance is measured using DC on FKS, FAS, and SPPO membranes. Simulation curve and experimental data are compared and residues are presented. Current ratio is $r = 0.56$ of SPPO limiting current density, and DBL thickness δ is 1.0 mm.

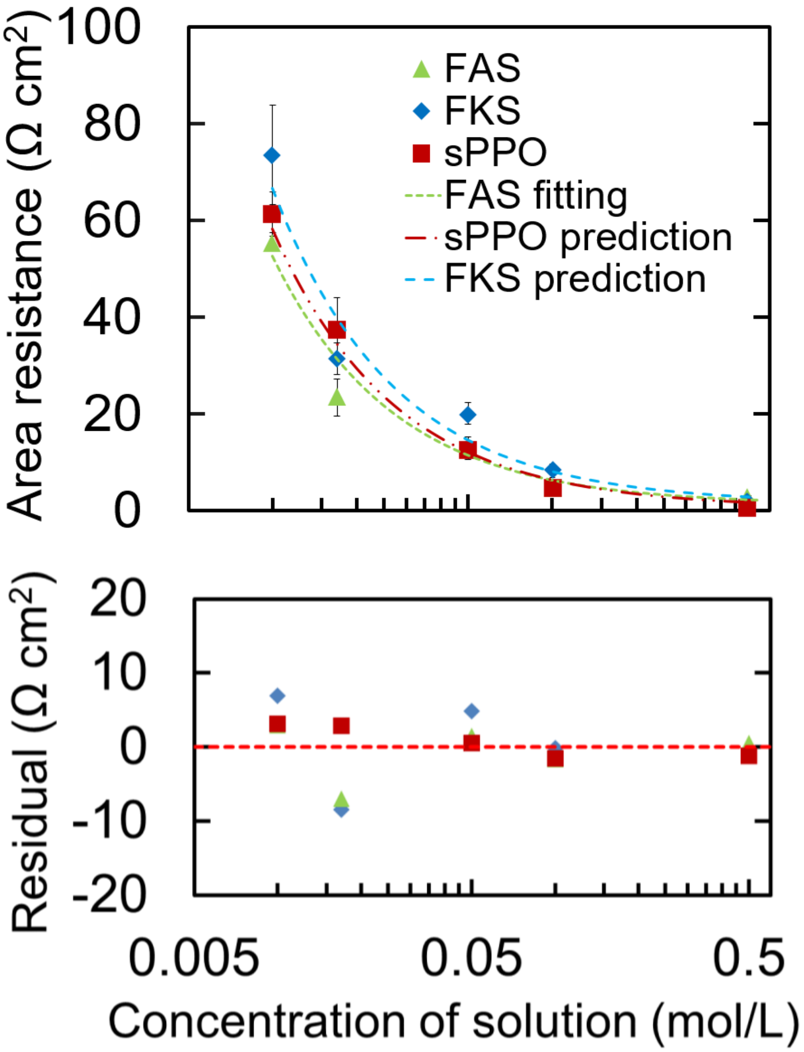

Figure 32 – Using data of FAS resistance for fitting, the FKS and SPPO membrane resistance are predicted by the model.

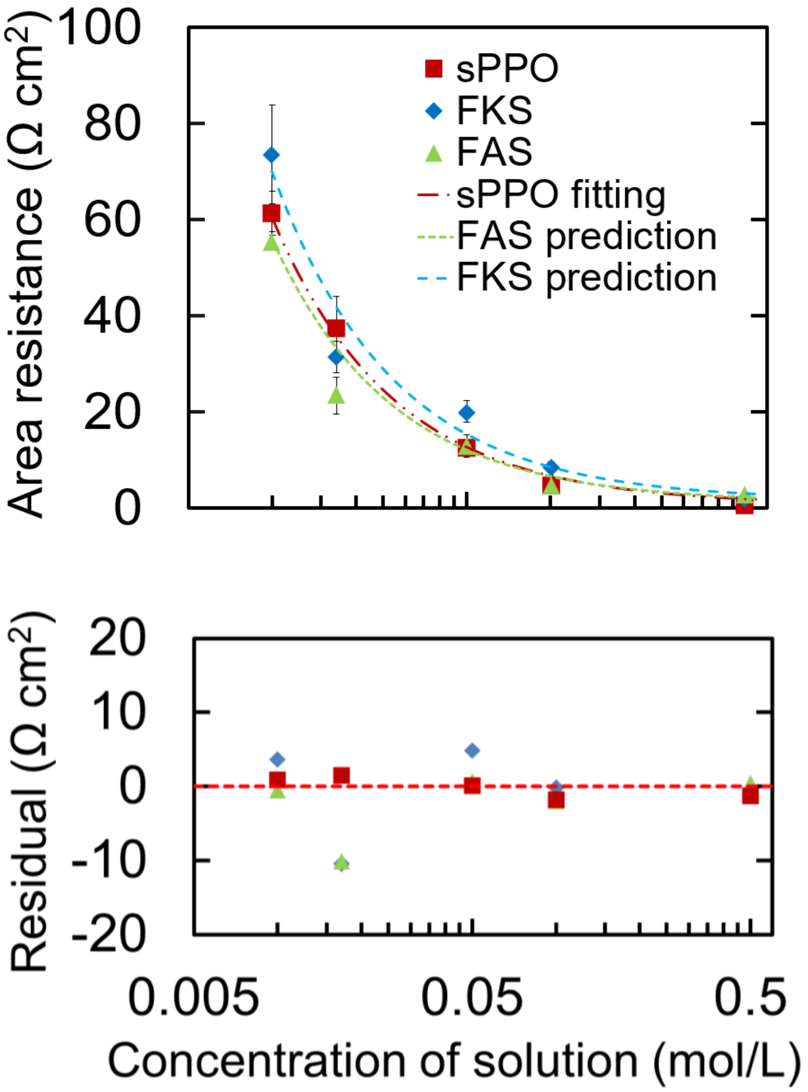

Figure 33 – Using data of SPPO resistance for fitting, the FKS and SPPO membrane resistance are predicted by the model.

APPENDIX C. SUPPORTING INFORMATION FOR CHAPTER 5

This appendix lists supporting information for CHAPTER 6 - MECHANISM EXPLORATION OF ION TRANSPORT IN NANOCOMPOSITE CATION EXCHANGE MEMBRANES.

C.1 Characterization of IEMs

The membrane sample in the acid form (H^+) was immersed into 1 M of NaCl for 6 hours. The resulting NaCl solution containing released protons was then titrated with 0.01 M of NaOH solution by using phenolphthalein as an indicator. Then the membrane sample was immersed in DI water for one day. After that, the wet membrane sample was weighted immediately after mopping with filter paper. The membrane sample was then dried in the oven at 50 °C until a constant weight (as dry weight) was obtained. The membrane IEC and swelling degree (SD) were then calculated by:

$$IEC = \frac{C_{NaOH} \times V_{NaOH}}{W_{dry}} \tag{81}$$

$$SD = \frac{W_{wet} - W_{dry}}{W_{dry}} \times 100\% \tag{82}$$

where C_{NaOH} is the concentration (M) of NaOH solution used, V_{NaOH} is the volume (L) of the NaOH solution, and W_{wet} and W_{dry} are the mass (g) of wet and dried membrane samples, respectively. All the measurements were conducted for at least three times.

Membrane porosity was calculated by using measured membrane weight data [32, 99]:

$$Porosity = \frac{W_{wet} - W_{dry}}{A\delta\rho_w} \times 100\% \tag{83}$$

where A is area of wet membrane sample (m^{-2}), δ is the thickness (m) of wet membrane sample, and ρ_w is the density of water ($kg \cdot m^3$).

Membrane apparent permselectivity was determined by calculating the ratio of measured membrane potential and theoretical membrane potential derived from Nernst equation. The membrane potential was measured by using a static potential method [65, 142]. The test membrane was set in between two cells with an open area of 4.8 cm^2. NaCl solutions of 0.5 M and 0.1 M were filled in the two cells, respectively. Two Ag/AgCl reference electrodes (Hanna Instruments, USA) were used two measure the potential difference across the membrane. The solutions in the two cells were vigorously stirred by using magnetic stir bars during the process, to minimize diffusion boundary layer effect. The apparent permselectivity was then calculated by:

$$\alpha(\%) = \frac{\Delta V_{measured}}{\Delta V_{theoretical}} \times 100\% \tag{84}$$

Membrane ionic resistance was measured by using a four-compartment Plexiglas cell [65]. Totally three membranes were set inside the measuring system, the membrane in the center was the one under investigation, and the other two were commercial FKS (Fumasep®, Fumatech, Germany) CEMs. All membranes were stabilized and had effective area of 7.9 cm^2. All four compartments were filled with 0.5 M of NaCl solution, with two outer compartments having immobile solution, and two inner compartments having inflow and outflow. The water flows were managed by using two peristaltic pumps (Cole-Parmer, USA). Two titanium electrodes covered with platinum were placed at edges of the outer compartments, and were connected to a power supply. Different current densities were applied and corresponding potentials were recorded. The resistance was obtained by the slope of current density versus the potential drop. The final membrane ionic resistance was calculated by subtracting the measured blank resistance (solution resistance) from the measured resistance.

C.2 Membrane degree of sulfonation and conductivity

The degree of sulfonation (DS) of polymers could be calculated by:

$$DS = \frac{IEC}{1000 \times [\frac{(1 - M_{SPPO} \times \frac{IEC}{1000})}{M_{PPO}} + \frac{IEC}{1000}]} \times 100\% \tag{85}$$

where M_{SPPO} is the molar weight ($g \cdot mol^{-1}$) of sulfonated PPO, and M_{PPO} is the molar weight ($g \cdot mol^{-1}$) of PPO. Theoretically, all the SPPO in this study should have the same DS, since all the PPO were sulfonated from the same batch. However, it is obvious that the addition of NPs increased the IEC of membranes, thus I rationalized the fact by assuming that the NPs change the DS of membrane polymeric material. So that different membranes could be treated as they were synthesized by using polymer of different DS.

By assuming that all the monomers, whether sulfonated or not, occupy the same volume in the matrices, volume fraction of pure gel phase (f_{11}) could be obtained as the product of DS and polymer gel phase (f_1), and the rest of the gel phase is occupied by inert polymer phase (f_{12}):

$$f_{11} = DS \times f_1 \tag{86}$$

$$f_{12} = f_1 - f_{11} \tag{87}$$

Table 14 – Membrane conductivity (k_m) in different solution concentrations

Membranes	Membrane conductivity [µS cm^{-1}] in different solution concentrations				
	0.01M	0.02M	0.05M	0.08M	0.1M
Membrane 1	464.0	578.2	984.9	1370.8	1621.6
Membrane 2	570.9	717.0	1293.5	1819.9	2230.2
Membrane 3	597.9	766.8	1348.0	1818.2	2350.1
Membrane 4	571.6	747.1	1344.2	1884.1	2513.8
Membrane 5	538.6	691.8	1197.3	1673.0	2070.6

Table 15 – Degree of sulfonation and different membrane gel phases

Membranes	f_1 [%]	DS [%]	f_{11} [%]	f_{12} [%]
Membrane 1	44.8	30.9	13.8	31.0
Membrane 2	40.1	33.7	13.5	26.6
Membrane 3	41.2	33.4	13.8	27.4
Membrane 4	36.8	37.4	13.8	23.0
Membrane 5	41.5	32.2	13.4	28.1

C.3 Simulation Algorithm and Matlab Code

The input of the model is added particle numbers; the output is resulted number concentration of nanomaterial groups and fit to linear model to D_{eff}/D. The program is coded in Matlab 2016b (education edition, MathWorks®). A certain number of particles are initialized randomly with radius and position coordinates in 3-D space. For each pair of particles, the van der Waals energy is calculated and the inverse of these values are saved as matrix *A*. *A* is then used in the agglomerative hieratical clustering algorithm with a threshold as the implementation of energy cut-off , and 'average' method was used for clustering [36]. The resulted group numbers can be obtained by counting cluster numbers given the threshold.

The added particle values are varied and at each value, 50 replicates are recorded. The results are shown the following figure indicating the simulation in 1 μm^3 space with initial particles ranging from 0 to 2500. Particle diameter is normally distributed with mean of 20 nm and standard deviation of 1 nm. Fitted values is obtained by minimize the root mean square error of averaged simulated values with respect to experimental data. Energy threshold and fitting constants are summarized in Table 16.

Table 16 – Simulation parameters of studied nanoparticles

Nanoparticles	***a***	***b***	**Energy threshold (J)**	**References**
Iron oxide (100 nm)	0.200	0.0083	1.00E-23	[99]
Silica NPs (30 nm)	0.451	0.0119	1.12E-23	[140]
Silica NPs (30 nm)	0.579	0.0074	5.05E-23	[121]
Silica NPs (420 nm)	0.550	0.0042	3.61E-24	[141]
Silica NPs (17 nm)	0.233	0.0117	2.86E-24	This study

```
%% Author: Bopeng Zhang; December 30, 2016
% this script takes the best energy threshold and generates the simulated
% diffusivity (or effective diffusivity)
clear variables;
list = 1:25;
observed = zeros(50,length(list));
for j = 1:50
    for i = list
        NUMBER = i*27; THRESHOLD = 2.77E23; RADIUM = 210E-9;

        % first data store radius of particle; three coordinates later
        radius = normrnd(RADIUM, 1E-9, [NUMBER, 1]);
        radius(radius<0) = RADIUM;
        points = [radius 10E-6*rand([NUMBER,3])]; % random initialization in 1 um^3

        energy_distance = 1./pdist(points,@VDW);

        Z = linkage(energy_distance, 'average');
        T = cluster(Z, 'cutoff', THRESHOLD, 'criterion','distance');
        observed(j,i) = max(T);
    end
    plot(list*15, observed(j,:),'.');
    hold on;
    display(j);
end

xlabel('Added particle number');
ylabel('Resulted group number');

%%%%%%%%%%%%%%%%%%%%%%%%%%%%%%%%%%%%%%%%%%%%%%%%%%%%%%%%%%%%%%%%%%%%%%%%%%%

function energy = VDW(single, whole)

% taking as arguments a 1-by-N vector <single> containing a single observation
% from points, an M2-by-N matrix <whole> containing multiple observations from
% points, and returning an M2-by-1 vector of distances D2, whose Jth
% element is the force between the observations single and whole(J,:).

% Hamaker coefficient
A = 1E-20;


dist = pdist2(single(2:end), whole(:, 2:end));

%% The following calculation citing Abu-Lail et al. 2003 and Schenkel et al.
% 1960 in Supporting Information

% inter surface distance D = r - R1 - R2
D = dist' - single(1) - whole(:,1);
% avoid the negative value if two points are initialized closer then their radius
combined
D(D<0) = min(D(D>0));
```

```
function energy = VDW(single, whole)

% taking as arguments a 1-by-N vector <single> containing a single observation
% from points, an M2-by-N matrix <whole> containing multiple observations from
% points, and returning an M2-by-1 vector of distances D2, whose Jth
% element is the force between the observations single and whole(J,:).

% Hamaker coefficient
A = 1E-20;


dist = pdist2(single(2:end), whole(:, 2:end));

%% The following calculation citing Abu-Lail et al. 2003 and Schenkel et al.
% 1960 in Supporting Information

% inter surface distance D = r - R1 - R2
D = dist' - single(1) - whole(:,1);
% avoid the negative value if two points are initilized closer then their radius
combined
D(D<0) = min(D(D>0));
energy = A * single(1)*whole(:,1)./(single(1)+whole(:,1)) ./ D ./ (1 + 11.12*D / 1E-
7);

%}

end
```

APPENDIX D. SUPPORTING INFORMATION FOR CHAPTER 6

This appendix lists supporting information for CHAPTER 7 - PERCOLATION SIMULATION STUDY OF MASS TRANSPORT IN ION EXCHANGE MEMBRANES. An implementation of percolation theory simulation is provided in Java code. Additional functions are implemented to obtain number of site of different interest, which are well commented.

```
import java.io.*;
import java.util.Random;

public class Percolation3D {
    private final UnionFind matrix, full, fullBottom; // must be UnionFind data struc-
ture
    private final boolean [] opened; // record whether a site is open or not
    private final int nCol, nRow, nDep, size;
    private int openCount = 0;

    public Percolation3D(int row, int col, int dep) {
        // create row-by-col-by-dep grid, with all sites blocked
        nCol = col;
        nRow = row;
        nDep = dep;
        size = nCol * nRow * nDep;
        opened = new boolean[size];
        for (int i = 0; i < size; i++) {
            opened[i] = false;
        }
        matrix = new UnionFind(size+2);
        full = new UnionFind(size+1);
        fullBottom = new UnionFind(size+1);
    }

    public Percolation3D(int n) {
        // create n-by-n-by-n grid, with all sites blocked
        checkIndices(n);
        nCol = n;
        nRow = n;
        nDep = n;
        size = n * n * n;
        opened = new boolean[size];
        for (int i = 0; i < size; i++) {
            opened[i] = false;
        }
        matrix = new UnionFind(size+2);
        full = new UnionFind(size+1);
        fullBottom = new UnionFind(size+1);
    }

    private void printMatrix() {
        // visualization of matrix for debugging; only intuitive on 2-D
        for (int i = 0; i < size; i++) {
            if (opened[i]) {
                System.out.print(" o ");
            } else {
                System.out.print(" * ");
            }
            if ((i + 1) % nCol == 0) {
                System.out.println();
            }
        }
    }

    private void checkIndices(int row, int col, int dep) {
        if (row <= 0 || row > nRow) throw new IllegalArgumentException("row index i
out of bounds");
        if (col <= 0 || col > nCol) throw new IllegalArgumentException("column index i
out of bounds");
        if (dep <= 0 || dep > nDep) throw new IllegalArgumentException("depth index i
out of bounds");
```

```
    }

    private void checkIndices(int n) {
        if (n <= 0) throw new IllegalArgumentException();
    }

    private boolean isLegalSite(int row, int col, int dep)  {
        return dep > 0 && dep <= nDep;
    }

    private int indexing(int row, int col, int dep) {
        // given 3-D coordinates returns index with periodic boundary condition on row and col
        if (row == 0) row = nRow;
        if (row == nRow + 1) row = 1;
        if (col == 0) col = nCol;
        if (col == nCol + 1) col = 1;
        return nCol * nRow * (dep - 1) + nCol * (row - 1) + col;
    }

    private void connectSite(int current, int neighbor) {
        if (opened[neighbor-1]) {
            matrix.union(current, neighbor);
            full.union(current, neighbor);
            fullBottom.union(current, neighbor);
        }
    }

    public void open(int row, int col, int dep) {
        checkIndices(row, col, dep);
        int site = indexing(row, col, dep);
        if (!opened[site-1]) {
            opened[site-1] = true;  // mark this site as open
            openCount += 1; // count this open site
        }
        // connect to legal neighbor open sites; here periodic boundary ensure all legal sites on row and col dimensions
        connectSite(site, indexing(row + 1, col, dep));
        connectSite(site, indexing(row, col + 1, dep));
        connectSite(site, indexing(row - 1, col, dep));
        connectSite(site, indexing(row, col - 1, dep));
        if (isLegalSite(row, col, dep - 1))   connectSite(site, indexing(row, col, dep - 1));
        if (isLegalSite(row, col, dep + 1))   connectSite(site, indexing(row, col, dep + 1));

        // treat 0 as image site and connect with first row if opened
        if (site < nCol * nRow + 1) {
            matrix.union(0, site);
            full.union(0, site);
        }
        // treat size+1 as image site and connect with last row if opened
        if (site > indexing(1, 1, nDep) - 1){
            matrix.union(size+1, site);
            fullBottom.union(0, site);
        }
    }   // open site (row, col, dep) if it is not open already

    public boolean isOpen(int row, int col, int dep) {
        // check if a site is open or not given 3-D coordinates
        checkIndices(row, col, dep);
        return opened[indexing(row, col, dep)-1];
```

```
    }

    public int numberOfPercolatedSites() {
        // returns number of sites that are part of percolated pathway
        if (percolates()) {
            int fullOrPercolate = Math.max(matrix.numberInUnion(0), matrix.numberInUn-
ion(size+1)) - 2;
            int bottomDeadEnd = fullOrPercolate - numberOfTopFullSites();
            int topDeadEnd = fullOrPercolate - numberOfBottomFullSites();
            return fullOrPercolate - topDeadEnd - bottomDeadEnd;
        }
        else {return 0;}
    }

    protected int numberOfInertSites() {
        // returns number of sites that are part of percolated pathway
        if (percolates()) {
            return openCount - Math.max(matrix.numberInUnion(0), matrix.numberInUn-
ion(size+1)) + 2;
        } else return openCount - matrix.numberInUnion(0) - matrix.numberInUnion(size
+ 1) + 2;
    }

    int numberOfOpenSites() {
        // number of open sites
        return openCount;
    }

    boolean percolates() {
        return matrix.connected(0, size+1);
    }

    // used for calculation of different types of sites
    public int numberOfTopFullSites() { return full.numberInUnion(0) - 1; }
    // used for calculation of different types of sites
    public int numberOfBottomFullSites() { return fullBottom.numberInUnion(0) - 1; }

    public int getSize() {
        return size;
    }

    public void outputPercolation(String filename) {
        // output site array mark only sites belongs to percolation pathways
        try {
            File file = new File(filename);
            PrintWriter pw = new PrintWriter(file);
            pw.print(nCol);
            pw.print(",");
            pw.print(nRow);
            pw.print(",");
            pw.print(nDep);
            pw.print(",");
            for (int i=1; i<= size; i++) {
                if (full.connected(0, i) && fullBottom.connected(0, i)) {
                    pw.print(1);
                    pw.print(",");
                } else {
                    pw.print(0);
                    pw.print(",");
                }
            }
            pw.close();
```

```
        } catch (FileNotFoundException ex) {
            System.out.print(ex.fillInStackTrace());
        }
    }

    public int checkOpenType(int position) {
        // checks whether an open site is surrounded by all open sites (void) or not
        int[] pos = indexToPosition(position);
        int row = pos[0]; int col = pos[1]; int dep = pos[2];
        int openNeighbors = 0;
        // count the number of legal neighbor open sites
        if (opened[indexing(row + 1, col, dep) - 1]) { openNeighbors++;}
        if (opened[indexing(row, col + 1, dep) - 1]) { openNeighbors++;}
        if (opened[indexing(row - 1, col, dep) - 1]) { openNeighbors++;}
        if (opened[indexing(row, col - 1, dep) - 1]) { openNeighbors++;}
        if (isLegalSite(row, col, dep - 1)) {if (isOpen(row, col, dep - 1))
{ openNeighbors++;}}
        if (isLegalSite(row, col, dep + 1)) {if (isOpen(row, col, dep + 1))
{ openNeighbors++;}}

        return openNeighbors;
    }

    public int[] indexToPosition(int ind){
        // utility function to translate index to 3-D coordinates
        int[] position = new int[3];
        position[2] = (ind - 1) / (nRow*nCol) + 1; // depth
        int remainder = (ind - 1) % (nRow*nCol);
        position[0] = remainder / nCol + 1;  // row
        position[1] = remainder % nCol + 1;      // column

        return position;
    }

    public int getVoidSites(int voidNeighborNumber) {
        int countVoid = 0;
        // loop through all sites to find open sites with more than @voidNeighbor-
Number of open neighbors
        for (int i=1; i<= size; i++){
            if (full.connected(0, i) && fullBottom.connected(0, i)) {
                if(checkOpenType(i)>=voidNeighborNumber) countVoid++;
            }
        }

        return countVoid;
    }

    public int numberOfSurfacePercolatedSites() {
        int count = 0;
        // loop through all "surface" sites to find open sites belongs to percolation
pathways
        for (int i=1; i<= nRow*nCol; i++){
            if (full.connected(0, i) && fullBottom.connected(0, i)) {
                count ++;
            }
        }

        for (int i=(nDep-1)*nCol*nRow+1; i<=size; i++) {
            if (full.connected(0, i) && fullBottom.connected(0, i)) {
                count ++;
            }
        }
```

```
        return count / 2; // average surface area that belongs to percolated sites
    }

    public double normalConductivity(int membraneKappa, int solutionKappa) {
        // explicit calculation of conductivity along the dep dimension
        double conduc = 0, conducTemp = 0;
        for (int i = 1; i <= nRow * nCol; i++) {
            for (int d = 1; d <= nDep; d++) {
                int ind = (d - 1) * nRow * nCol + i;
                if (opened[ind - 1]) {
                    conducTemp += (double) 1 / solutionKappa;
                } else {
                    conducTemp += (double) 1 / membraneKappa;
                }
            }
            conduc += 1 / conducTemp;
        }

        return conduc;
    }

    public static void main(String[] args) {
        // test client (showing an exemplary usage
        int nRow = 256, nCol = 256, nDep =256;
        Percolation3D p = new Percolation3D(nRow, nCol, nDep);
        double freeRatio = 0.50;

        Random rand = new Random();
        while (!p.percolates()) {
            int row = rand.nextInt(nRow) + 1;
            int col = rand.nextInt(nCol) + 1;
            int dep = rand.nextInt(nDep) + 1;
            p.open(row, col, dep);
        }

        System.out.println((float)p.numberOfOpenSites()/p.size);
    }
}
```

```
public class UnionFind {
    private int[] root;     // root
    private int[] size;     // number of children rooted
    private int count;    // number of components
    /**
     * Initializes an empty union-find data structure with {@code n} sites
     * {@code 0} through {@code n-1}. Each site is initially in its own
     * component.
     * @param  n the number of sites
     */
    public UnionFind(int n) {
        count = n;
        root = new int[n];
        size = new int[n];
        for (int i = 0; i < n; i++) {
            root[i] = i;
            size[i] = 1;
        }
    }

    public int findRoot(int i) {
        validate(i);
        while(i != root[i]) {
            root[i] = root[root[i]];
            i = root[i];
        }
        return i;
    }

    // validate that p is a valid index
    private void validate(int p) {
        int n = root.length;
        if (p < 0 || p >= n) {
            throw new IllegalArgumentException("index " + p + " is not between 0 and "
+ (n-1));
        }
    }
    /**
     * Returns number of inter isolated unions
     */
    public int count() { return count; }

    /**
     * Returns true if two sites are in union
     */
    public boolean connected(int p, int q) { return findRoot(p) == findRoot(q); }

    public void union(int p, int q){
        int i = findRoot(p);
        int j = findRoot(q);
        if (i == j) return;
        if (size[i] <size[j]) {root[i] = j; size[j] += size[i]; }
        else                  {root[j] = i; size[i] += size[j]; }
        count--;
    }
    /**
     * Returns the number of unioned sites for special applications
     */
    public int numberInUnion(int element){
        return size[findRoot(element)];
    }

}
```

REFERENCES

[1] R.E. Pattle, Production of Electric Power by Mixing Fresh and Salt Water in the Hydroelectric Pile, Nature, 174 (1954) 660-660.

[2] J.N. Weinstein, F.B. Leitz, Electric-Power from Difference in Salinity - Dialytic Battery, Science, 191 (1976) 557-559.

[3] K.L. Lee, R.W. Baker, H.K. Lonsdale, Membranes for Power-Generation by Pressure-Retarded Osmosis, J Membrane Sci, 8 (1981) 141-171.

[4] B.E. Logan, M. Elimelech, Membrane-based processes for sustainable power generation using water, Nature, 488 (2012) 313-319.

[5] G.Z. Ramon, B.J. Feinberg, E.M.V. Hoek, Membrane-based production of salinity-gradient power, Energ Environ Sci, 4 (2011) 4423-4434.

[6] J.W. Post, H.V.M. Hamelers, C.J.N. Buisman, Energy recovery from controlled mixing salt and fresh water with a reverse electrodialysis system, Environ Sci Technol, 42 (2008) 5785-5790.

[7] J.W. Post, J. Veerman, H.V.M. Hamelers, G.J.W. Euverink, S.J. Metz, K. Nymeijer, C.J.N. Buisman, Salinity-gradient power: Evaluation of pressure-retarded osmosis and reverse electrodialysis, J Membrane Sci, 288 (2007) 218-230.

[8] S. Nouri, L. Dammak, G. Bulvestre, B. Auclair, Comparison of three methods for the determination of the electrical conductivity of ion-exchange polymers, Eur Polym J, 38 (2002) 1907-1913.

[9] P. Dlugolecki, K. Nymeijer, S. Metz, M. Wessling, Current status of ion exchange membranes for power generation from salinity gradients, J Membrane Sci, 319 (2008) 214-222.

[10] G.M. Geise, A.J. Curtis, M.C. Hatzell, M.A. Hickner, B.E. Logan, Salt Concentration Differences Alter Membrane Resistance in Reverse Electrodialysis Stacks, Environmental Science & Technology Letters, 1 (2013) 36-39.

[11] P. Dlugolecki, B. Anet, S.J. Metz, K. Nijmeijer, M. Wessling, Transport limitations in ion exchange membranes at low salt concentrations, J Membrane Sci, 346 (2010) 163-171.

[12] P. Dlugolecki, A. Gambier, K. Nijmeijer, M. Wessling, Practical Potential of Reverse Electrodialysis As Process for Sustainable Energy Generation, Environ Sci Technol, 43 (2009) 6888-6894.

[13] P. Dlugolecki, P. Ogonowski, S.J. Metz, M. Saakes, K. Nijmeijer, M. Wessling, On the resistances of membrane, diffusion boundary layer and double layer in ion exchange membrane transport, J Membrane Sci, 349 (2010) 369-379.

[14] T. Sata, Ion Exchange Membranes: Preparation, Characterization, Modification and Application, The Royal Society of Chemistry, Cambridge, 2004.

[15] A.H. Galama, D.A. Vermaas, J. Veerman, M. Saakes, H.H.M. Rijnaarts, J.W. Post, Membrane resistance: the effect of salinity gradients over a cation exchange membrane, J Membrane Sci, 467 (2014) 279-291.

[16] P. Sistat, G. Pourcelly, Chronopotentiometric response of an ion-exchange membrane in the underlimiting current-range. Transport phenomena within the diffusion layers, J Membrane Sci, 123 (1997) 121-131.

[17] R. Audinos, G. Pichelin, Characterization of Electrodialysis Membranes by Chronopotentiometry, Desalination, 68 (1988) 251-263.

[18] A.A. Moya, P. Sistat, Chronoamperometric response of ion-exchange membrane systems, J Membrane Sci, 444 (2013) 412-419.

[19] J.S. Park, J.H. Choi, J.J. Woo, S.H. Moon, An electrical impedance spectroscopic (EIS) study on transport characteristics of ion-exchange membrane systems, J Colloid Interf Sci, 300 (2006) 655-662.

[20] L.V. Karpenko, O.A. Demina, G.A. Dvorkina, S.B. Parshikov, C. Larchet, B. Auclair, N.P. Berezina, Comparative study of methods used for the determination of electroconductivity of ion-exchange membranes, Russ J Electrochem+, 37 (2001) 287-293.

[21] R.K. Nagarale, G.S. Gohil, V.K. Shahi, Recent developments on ion-exchange membranes and electro-membrane processes, Adv Colloid Interfac, 119 (2006) 97-130.

[22] V.V. Nikonenko, A.E. Kozmai, Electrical equivalent circuit of an ion-exchange membrane system, Electrochim Acta, 56 (2011) 1262-1269.

[23] F.G. Helfferich, Ion exchange, McGraw-Hill, New York,, 1962.

[24] H. Strathmann, A. Grabowski, G. Eigenberger, Ion-Exchange Membranes in the Chemical Process Industry, Ind Eng Chem Res, 52 (2013) 10364-10379.

[25] J. Veerman, J.W. Post, M. Saakes, S.J. Metz, G.J. Harmsen, Reducing power losses caused by ionic shortcut currents in reverse electrodialysis stacks by a validated model, J Membrane Sci, 310 (2008) 418-430.

[26] A. Grabowski, G.Q. Zhang, H. Strathmann, G. Eigenberger, The production of high purity water by continuous electrodeionization with bipolar membranes: Influence of the anion-exchange membrane permselectivity, J Membrane Sci, 281 (2006) 297-306.

[27] H. Strathmann, Electrodialysis, a mature technology with a multitude of new applications, Desalination, 264 (2010) 268-288.

[28] G.M. Geise, M.A. Hickner, B.E. Logan, Ionic Resistance and Permselectivity Tradeoffs in Anion Exchange Membranes, Acs Appl Mater Inter, 5 (2013) 10294-10301.

[29] D.L. Feldheim, Lawson, Del R., and Martin, Charles R., Influence of the sulfonate countercation on the thermal stability of Nafion perfluorousulfonate membranes, Journal of Polymer Science: Part B: Polymer Physics, 31 (1993) 953-957.

[30] N.P. Brandon, S. Skinner, B.C.H. Steele, Recent advances in materials for fuel cells, Annu Rev Mater Res, 33 (2003) 183-213.

[31] K. Kontturi, Murtomäki, L., Manzanares, J. A., Ionic Transport Processes in Electrochemistry and Membrane Science, Oxford University Press, 2008.

[32] H. Strathmann, Ion-exchange membrane separation processes, 1st ed., Elsevier, Amsterdam ; Boston, 2004.

[33] H. Strathmann, ScienceDirect (Online service), Ion-exchange membrane separation processes, in: Membrane science and technology series,, Elsevier,, Amsterdam ; Boston, 2004, pp. xi, 348 p.

[34] E. Guler, Y.L. Zhang, M. Saakes, K. Nijmeijer, Tailor-Made Anion-Exchange Membranes for Salinity Gradient Power Generation Using Reverse Electrodialysis, Chemsuschem, 5 (2012) 2262-2270.

[35] F. Helfer, C. Lemckert, Y.G. Anissimov, Osmotic power with Pressure Retarded Osmosis: Theory, performance and trends - A review, J Membrane Sci, 453 (2014) 337-358.

[36] S. Koter, P. Piotrowski, J. Kerres, Comparative investigations of ion-exchange membranes, J Membrane Sci, 153 (1999) 83-90.

[37] C. Klaysom, S.H. Moon, B.P. Ladewig, G.Q.M. Lu, L.Z. Wang, Preparation of porous ion-exchange membranes (IEMs) and their characterizations, J Membrane Sci, 371 (2011) 37-44.

[38] A.H. Galama, J.W. Post, M.A.C. Stuart, P.M. Biesheuvel, Validity of the Boltzmann equation to describe Donnan equilibrium at the membrane-solution interface, J Membrane Sci, 442 (2013) 131-139.

[39] E. Guler, R. Elizen, D. Vermaas, M. Saakes, K. Nijmeijer, Performance-determining membrane properties in reverse electrodialysis, J Membrane Sci, (2013).

[40] M. Kumar, S. Singh, V.K. Shahi, Cross-Linked Poly(vinyl alcohol)-Poly(acrylonitrile-co-2-dimethylamino ethylmethacrylate) Based Anion-Exchange Membranes in Aqueous Media, J Phys Chem B, 114 (2010) 198-206.

[41] A.R. Khare, N.A. Peppas, Swelling Deswelling of Anionic Copolymer Gels, Biomaterials, 16 (1995) 559-567.

[42] J. Veerman, M. Saakes, S. Metz, G. Harmsen, Reverse electrodialysis: Performance of a stack with 50 cells on the mixing of sea and river water, J Membrane Sci, 327 (2009) 136-144.

[43] R.E. Lacey, Energy by Reverse Electrodialysis, Ocean Eng, 7 (1980) 1-47.

[44] J. Veerman, M. Saakes, S. Metz, G. Harmsen, Reverse electrodialysis: evaluation of suitable electrode systems, J Appl Electrochem, 40 (2010) 1461-1474.

[45] D.A. Vermaas, M. Saakes, K. Nijmeijer, Doubled Power Density from Salinity Gradients at Reduced Intermembrane Distance, Environ Sci Technol, 45 (2011) 7089-7095.

[46] K.S. Kim, W. Ryoo, M.S. Chun, G.Y. Chung, Simulation of enhanced power generation by reverse electrodialysis stack module in serial configuration, Desalination, 318 (2013) 79-87.

[47] F. Suda, T. Matsuo, D. Ushioda, Transient changes in the power output from the concentration difference cell (dialytic battery) between seawater and river water, Energy, 32 (2007) 165-173.

[48] M. Turek, B. Bandura, Renewable energy by reverse electrodialysis, Desalination, 205 (2007) 67-74.

[49] E. Brauns, Salinity gradient power by reverse electrodialysis: effect of model parameters on electrical power output, Desalination, 237 (2009) 378-391.

[50] E. Brauns, Towards a worldwide sustainable and simultaneous large-scale production of renewable energy and potable water through salinity gradient power by combining reversed electrodialysis and solar power?, Desalination, 219 (2008) 312-323.

[51] H.P. Gregor, M.A. Peterson, Electrodialytic Polarization of Ion-Exchange Membrane Systems, J Phys Chem-Us, 68 (1964) 2201-&.

[52] Lakshmin.N, Transport Phenomena in Artificial Membranes, Chem Rev, 65 (1965) 491-565.

[53] V.M. Barragan, C. Ruiz-Bauza, Current-voltage curves for ion-exchange membranes: A method for determining the limiting current density, J Colloid Interf Sci, 205 (1998) 365-373.

[54] D.A. Vermaas, M. Saakes, K. Nijmeijer, Enhanced mixing in the diffusive boundary layer for energy generation in reverse electrodialysis, J Membrane Sci, 453 (2014) 312-319.

[55] D.A. Vermaas, E. Guler, M. Saakes, K. Nijmeijer, Theoretical power density from salinity gradients using reverse electrodialysis, Energy Procedia, 20 (2012) 170-184.

[56] D.A. Vermaas, M. Saakes, K. Nijmeijer, Early detection of preferential channeling in reverse electrodialysis, Electrochim Acta, 117 (2014) 9-17.

[57] L. Gurreri, A. Tamburini, A. Cipollina, G. Micale, M. Ciofalo, CFD Simulation of Mass Transfer Phenomena in Spacer Filled Channels for Reverse Electrodialysis Applications, Chem Engineer Trans, 32 (2013) 1879-1884.

[58] M. Tedesco, A. Cipollina, A. Tamburini, I.D.L. Bogle, G. Micale, A simulation tool for analysis and design of reverse electrodialysis using concentrated brines, Chemical Engineering Research and Design, (2014).

[59] J. Veerman, M. Saakes, S.J. Metz, G.J. Harmsen, Electrical Power from Sea and River Water by Reverse Electrodialysis: A First Step from the Laboratory to a Real Power Plant, Environ Sci Technol, 44 (2010) 9207-9212.

[60] J. Veerman, R.M. de Jong, M. Saakes, S.J. Metz, G.J. Harmsen, Reverse electrodialysis: Comparison of six commercial membrane pairs on the thermodynamic efficiency and power density, J Membrane Sci, 343 (2009) 7-15.

[61] J.W. Post, H.V.M. Hamelers, C.J.N. Buisman, Influence of multivalent ions on power production from mixing salt and fresh water with a reverse electrodialysis system, J Membrane Sci, 330 (2009) 65-72.

[62] J.G. Hong, W. Zhang, J. Luo, Y. Chen, Modeling of power generation from the mixing of simulated saline and freshwater with a reverse electrodialysis system: The effect of monovalent and multivalent ions, Applied Energy, 110 (2013) 244-251.

[63] J.G. Hong, W. Zhang, J. Luo, Y. Chen, Corrigendum to "Modeling of power generation from the mixing of simulated saline and freshwater with a reverse electrodialysis system: The effect of monovalent and multivalent ions"[Appl. Energy 110 (2013) 244–251], Appl Energ, (2014).

[64] D.A. Vermaas, J. Veerman, M. Saakes, K. Nijmeijer, Influence of multivalent ions on renewable energy generation in reverse electrodialysis, Energ Environ Sci, 7 (2014) 1434-1445.

[65] J.G. Hong, Y. Chen, Nanocomposite reverse electrodialysis (RED) ion-exchange membranes for salinity gradient power generation, J Membrane Sci, 460 (2014) 139-147.

[66] E. Guler, R. Elizen, M. Saakes, K. Nijmeijer, Micro-structured membranes for electricity generation by reverse electrodialysis, J Membrane Sci, 458 (2014) 136-148.

[67] N.Y. Yip, D.A. Vermaas, K. Nijmeijer, M. Elimelech, Thermodynamic, Energy Efficiency, and Power Density Analysis of Reverse Electrodialysis Power Generation with Natural Salinity Gradients, Environ Sci Technol, 48 (2014) 4925-4936.

[68] J. Jagur-Grodzinski, R. Kramer, Novel process for direct conversion of free energy of mixing into electric power, Industrial & Engineering Chemistry Process Design and Development, 25 (1986) 443-449.

[69] A. Elattar, A. Elmidaoui, N. Pismenskaia, C. Gavach, G. Pourcelly, Comparison of transport properties of monovalent anions through anion-exchange membranes, J Membrane Sci, 143 (1998) 249-261.

[70] E. Volodina, N. Pismenskaya, V. Nikonenko, C. Larchet, G. Pourcelly, Ion transfer across ion-exchange membranes with homogeneous and heterogeneous surfaces, J Colloid Interf Sci, 285 (2005) 247-258.

[71] R. Audinos, Inverse electrodialysis. Study of electric energy obtained starting with two solutions of different salinity, J Power Sources, 10 (1983) 203-217.

[72] P. Dlugolecki, J. Dabrowska, K. Nijmeijer, M. Wessling, Ion conductive spacers for increased power generation in reverse electrodialysis, J Membrane Sci, 347 (2010) 101-107.

[73] O. Kedem, Reduction of Polarization in Electrodialysis by Ion-Conducting Spacers, Desalination, 16 (1975) 105-118.

[74] O. Scialdone, C. Guarisco, S. Grispo, A. Angelo, A. Galia, Investigation of electrode material–Redox couple systems for reverse electrodialysis processes. Part I: Iron redox couples, J Electroanal Chem, 681 (2012) 66-75.

[75] W. Li, W.B. Krantz, E.R. Cornelissen, J.W. Post, A.R. Verliefde, C.Y. Tang, A novel hybrid process of reverse electrodialysis and reverse osmosis for low energy seawater desalination and brine management, Appl Energ, 104 (2013) 592-602.

[76] Y. Kim, B.E. Logan, Microbial reverse electrodialysis cells for synergistically enhanced power production, Environ Sci Technol, 45 (2011) 5834-5839.

[77] B.E. Logan, K. Rabaey, Conversion of wastes into bioelectricity and chemicals by using microbial electrochemical technologies, Science, 337 (2012) 686-690.

[78] H.V. Hamelers, A. Ter Heijne, T.H. Sleutels, A.W. Jeremiasse, D.P. Strik, C.J. Buisman, New applications and performance of bioelectrochemical systems, Applied microbiology and biotechnology, 85 (2010) 1673-1685.

[79] Y. Kim, B.E. Logan, Hydrogen production from inexhaustible supplies of fresh and salt water using microbial reverse-electrodialysis electrolysis cells, P Natl Acad Sci USA, 108 (2011) 16176-16181.

[80] J.-Y. Nam, R.D. Cusick, Y. Kim, B.E. Logan, Hydrogen generation in microbial reverse-electrodialysis electrolysis cells using a heat-regenerated salt solution, Environ Sci Technol, 46 (2012) 5240-5246.

[81] D.A. Vermaas, M. Saakes, K. Nijmeijer, Power generation using profiled membranes in reverse electrodialysis, J Membrane Sci, 385–386 (2011) 234-242.

[82] A. Daniilidis, D.A. Vermaas, R. Herber, K. Nijmeijer, Experimentally obtainable energy from mixing river water, seawater or brines with reverse electrodialysis, Renew Energ, 64 (2014) 123-131.

[83] G.M. Geise, M.A. Hickner, B.E. Logan, Ammonium Bicarbonate Transport in Anion Exchange Membranes for Salinity Gradient Energy, Acs Macro Lett, 2 (2013) 814-817.

[84] X.P. Zhu, W.H. He, B.E. Logan, Influence of solution concentration and salt types on the performance of reverse electrodialysis cells, J Membrane Sci, 494 (2015) 154-160.

[85] A. Daniilidis, R. Herber, D.A. Vermaas, Upscale potential and financial feasibility of a reverse electrodialysis power plant, Appl Energ, 119 (2014) 257-265.

[86] M. Tedesco, E. Brauns, A. Cipollina, G. Micale, P. Modica, G. Russo, J. Helsen, Reverse electrodialysis with saline waters and concentrated brines: A laboratory investigation towards technology scale-up, J Membrane Sci, 492 (2015) 9-20.

[87] R.P. Allison, The continuous electrodeionization process, Water Supply Puzzle: How Does Desalting Fit In?, (1996) 197-206.

[88] J.P. Denoncourt, Y. Oren, L.M. Woo, Y. Egozy, High-Purity Water by Electrodeionization-Ii - Operation on Hard Water, Abstr Pap Am Chem S, 197 (1989) 152-IAEC.

[89] O. Arar, U. Yuksel, N. Kabay, M. Yuksel, Various applications of electrodeionization (EDI) method for water treatment-A short review, Desalination, 342 (2014) 16-22.

[90] F. Zhang, M. Chen, Y. Zhang, R.J. Zeng, Microbial desalination cells with ion exchange resin packed to enhance desalination at low salt concentration, J Membrane Sci, 417 (2012) 28-33.

[91] K. Zhang, M. Wang, D. Wang, C.J. Gao, The energy-saving production of tartaric acid using ion exchange resin-filling bipolar membrane electrodialysis, J Membrane Sci, 341 (2009) 246-251.

[92] Q.H. Li, C.H. Huang, T.W. Xu, Alcohol splitting for the production of methyl methoxyacetate: Integration of ion-exchange with bipolar membrane electrodialysis, J Membrane Sci, 367 (2011) 314-318.

[93] G.C. Ganzi, J.H. Wood, C.S. Griffin, Water-Purification and Recycling Using the Cdi Process, Environ Prog, 11 (1992) 49-53.

[94] K.H. Yeon, J.H. Seong, S. Rengaraj, S.H. Moon, Electrochemical characterization of ion-exchange resin beds and removal of cobalt by electrodeionization for high purity water production, Sep Sci Technol, 38 (2003) 443-462.

[95] S. Pawlowski, J.G. Crespo, S. Velizarov, Pressure drop in reverse electrodialysis: Experimental and modeling studies for stacks with variable number of cell pairs, J Membrane Sci, 462 (2014) 96-111.

[96] J.W. Lee, K.H. Yeon, J.H. Song, S.H. Moon, Characterization of electroregeneration and determination of optimal current density in continuous electrodeionization, Desalination, 207 (2007) 276-285.

[97] L. Alvarado, A.C. Chen, Electrodeionization: Principles, Strategies and Applications, Electrochim Acta, 132 (2014) 583-597.

[98] E. Korngold, Electrodialysis Processes Using Ion-Exchange Resins between Membranes, Desalination, 16 (1975) 225-233.

[99] J.G. Hong, Y. Chen, Evaluation of electrochemical properties and reverse electrodialysis performance for porous cation exchange membranes with sulfate-functionalized iron oxide, J Membrane Sci, 473 (2015) 210-217.

[100] X. Zhu, M.C. Hatzell, R.D. Cusick, B.E. Logan, Microbial reverse-electrodialysis chemical-production cell for acid and alkali production, Electrochemistry Communications, 31 (2013) 52-55.

[101] H.K. Hansen, L.M. Ottosen, A. Villumsen, Electrical resistance and transport numbers of ion-exchange membranes used in electrodialytic soil remediation, Sep Sci Technol, 34 (1999) 2223-2233.

[102] N.P. Berezina, N.A. Kononenko, O.A. Dyomina, N.P. Gnusin, Characterization of ion-exchange membrane materials: Properties vs structure, Adv Colloid Interfac, 139 (2008) 3-28.

[103] V.I. Zabolotsky, V.V. Nikonenko, Effect of Structural Membrane Inhomogeneity on Transport-Properties, J Membrane Sci, 79 (1993) 181-198.

[104] A.A. Moya, Electric circuits modelling the low-frequency impedance of ideal ion-exchange membrane systems, Electrochim Acta, 62 (2012) 296-304.

[105] J.H. Choi, J.S. Park, S.H. Moon, Direct measurement of concentration distribution within the boundary layer of an ion-exchange membrane, J Colloid Interf Sci, 251 (2002) 311-317.

[106] J. Veerman, M. Saakes, S.J. Metz, G.J. Harmsen, Reverse electrodialysis: A validated process model for design and optimization, Chem Eng J, 166 (2011) 256-268.

[107] K. Urano, Y. Masaki, M. Kawabata, Electric Resistances of Ion-Exchange Membranes in Dilute-Solutions, Desalination, 58 (1986) 171-176.

[108] S.B. Sang, Q.M. Wu, K.L. Huang, A discussion on ion conductivity at cation exchange membrane/solution interface, Colloid Surface A, 320 (2008) 43-48.

[109] L. Gurreri, A. Tamburini, A. Cipollina, G. Micale, CFD analysis of the fluid flow behavior in a reverse electrodialysis stack, Desalin Water Treat, 48 (2012) 390-403.

[110] M. Tedesco, H.V.M. Hamelers, P.M. Biesheuvel, Nernst-Planck transport theory for (reverse) electrodialysis: I. Effect of co-ion transport through the membranes, J Membrane Sci, 510 (2016) 370-381.

[111] K. Kontturi, L. Murtomäki, J.A. Manzanares, Oxford University Press., Ionic Transport Processes in Electrochemistry and Membrane Science, in, Oxford University Press,, Oxford, 2008, pp. 304 p.

[112] Y. Tanaka, Ion exchange membranes : fundamentals and applications, 1st ed., Elsevier, Amsterdam ; Boston, 2007.

[113] S.B. Sang, K.L. Huang, X.G. Li, W. Xian, Structure and resistance of concentration polar layer on cation exchange membrane-solution interface, T Nonferr Metal Soc, 16 (2006) 1436-1441.

[114] S. Pawlowski, P. Sistat, J.G. Crespo, S. Velizarov, Mass transfer in reverse electrodialysis: Flow entrance effects and diffusion boundary layer thickness, J Membrane Sci, 471 (2014) 72-83.

[115] AGC, Selemion Ion Exchange Membrane, in, 2014, pp. Selemion Ion Exchange Membrane Products Pamphlet.

[116] A.A. Moya, A numerical comparison of optimal load and internal resistances in ion-exchange membrane systems under reverse electrodialysis conditions, Desalination, 392 (2016) 25-33.

[117] K.S. Kim, W. Ryoo, M.-S. Chun, G.-Y. Chung, Simulation of enhanced power generation by reverse electrodialysis stack module in serial configuration, Desalination, 318 (2013) 79-87.

[118] Y. Li, G. He, S. Wang, S. Yu, F. Pan, H. Wu, Z. Jiang, Recent advances in the fabrication of advanced composite membranes, J Mater Chem A, 1 (2013) 10058-10077.

[119] S. Kango, S. Kalia, A. Celli, J. Njuguna, Y. Habibi, R. Kumar, Surface modification of inorganic nanoparticles for development of organic–inorganic nanocomposites—A review, Progress in Polymer Science, 38 (2013) 1232-1261.

[120] B.P. Tripathi, V.K. Shahi, Organic–inorganic nanocomposite polymer electrolyte membranes for fuel cell applications, Progress in Polymer Science, 36 (2011) 945-979.

[121] X. Zuo, S. Yu, X. Xu, R. Bao, J. Xu, W. Qu, Preparation of organic–inorganic hybrid cation-exchange membranes via blending method and their electrochemical characterization, J Membrane Sci, 328 (2009) 23-30.

[122] G. Kickelbick, Concepts for the incorporation of inorganic building blocks into organic polymers on a nanoscale, Progress in Polymer Science, 28 (2003) 83-114.

[123] G. He, Z. Li, J. Zhao, S. Wang, H. Wu, M.D. Guiver, Z. Jiang, Nanostructured Ion-Exchange Membranes for Fuel Cells: Recent Advances and Perspectives, Adv Mater, 27 (2015) 5280-5295.

[124] B. Lin, S. Cheng, L. Qiu, F. Yan, S. Shang, J. Lu, Protic ionic liquid-based hybrid proton-conducting membranes for anhydrous proton exchange membrane application, Chem Mater, 22 (2010) 1807-1813.

[125] J.R. Capadona, O. Van Den Berg, L.A. Capadona, M. Schroeter, S.J. Rowan, D.J. Tyler, C. Weder, A versatile approach for the processing of polymer nanocomposites with self-assembled nanofibre templates, Nature Nanotechnology, 2 (2007) 765-769.

[126] M. Tortello, S. Bianco, V. Ijeri, P. Spinelli, E. Tresso, Nafion membranes with vertically-aligned CNTs for mixed proton and electron conduction, J Membrane Sci, 415 (2012) 346-352.

[127] H. Zarrin, D. Higgins, Y. Jun, Z. Chen, M. Fowler, Functionalized graphene oxide nanocomposite membrane for low humidity and high temperature proton exchange membrane fuel cells, The Journal of Physical Chemistry C, 115 (2011) 20774-20781.

[128] Y.-H. Su, Y.-L. Liu, Y.-M. Sun, J.-Y. Lai, D.-M. Wang, Y. Gao, B. Liu, M.D. Guiver, Proton exchange membranes modified with sulfonated silica nanoparticles for direct methanol fuel cells, J Membrane Sci, 296 (2007) 21-28.

[129] S. Chung, Y. Wang, L. Persi, F. Croce, S. Greenbaum, B. Scrosati, E. Plichta, Enhancement of ion transport in polymer electrolytes by addition of nanoscale inorganic oxides, J Power Sources, 97 (2001) 644-648.

[130] S.L. Avilés-Barreto, D. Suleiman, Effect of single-walled carbon nanotubes on the transport properties of sulfonated poly (styrene–isobutylene–styrene) membranes, J Membrane Sci, 474 (2015) 92-102.

[131] B.G. Choi, J. Hong, Y.C. Park, D.H. Jung, W.H. Hong, P.T. Hammond, H. Park, Innovative polymer nanocomposite electrolytes: nanoscale manipulation of ion channels by functionalized graphenes, ACS nano, 5 (2011) 5167-5174.

[132] Y. Yao, Z. Lin, Y. Li, M. Alcoutlabi, H. Hamouda, X. Zhang, Superacidic Electrospun Fiber-Nafion Hybrid Proton Exchange Membranes, Advanced Energy Materials, 1 (2011) 1133-1140.

[133] C. Klaysom, R. Marschall, S.-H. Moon, B.P. Ladewig, G.M. Lu, L. Wang, Preparation of porous composite ion-exchange membranes for desalination application, J Mater Chem, 21 (2011) 7401-7409.

[134] V.I. Zabolotsky, V.V. Nikonenko, Effect of structural membrane inhomogeneity on transport properties, J Membrane Sci, 79 (1993) 181-198.

[135] T. Xu, W.H. Yang, B.L. He, Ionic conductivity threshold in sulfonated poly (phenylene oxide) matrices: a combination of three-phase model and percolation theory, Chemical Engineering Science, 56 (2001) 5343-5350.

[136] L.V. Karpenko-Jereb, N.P. Berezina, Determination of structural, selective, electrokinetic and percolation characteristics of ion-exchange membranes from conductive data, Desalination, 245 (2009) 587-596.

[137] M. Marino, J. Melchior, A. Wohlfarth, K. Kreuer, Hydroxide, halide and water transport in a model anion exchange membrane, J Membrane Sci, 464 (2014) 61-71.

[138] A. Amel, N. Gavish, L. Zhu, D.R. Dekel, M.A. Hickner, Y. Ein-Eli, Bicarbonate and chloride anion transport in anion exchange membranes, J Membrane Sci, 514 (2016) 125-134.

[139] D.J. Lewis, T.M. Day, J.V. MacPherson, Z. Pikramenou, Luminescent nanobeads: attachment of surface reactive Eu(III) complexes to gold nanoparticles, Chem Commun, (2006) 1433-1435.

[140] X. Zuo, S. Yu, X. Xu, J. Xu, R. Bao, X. Yan, New PVDF organic–inorganic membranes: the effect of SiO 2 nanoparticles content on the transport performance of anion-exchange membranes, J Membrane Sci, 340 (2009) 206-213.

[141] J.-H. Kim, S.-K. Kim, K. Nam, D.-W. Kim, Composite proton conducting membranes based on Nafion and sulfonated SiO 2 nanoparticles, J Membrane Sci, 415 (2012) 696-701.

[142] X. Tong, B. Zhang, Y. Chen, Fouling resistant nanocomposite cation exchange membrane with enhanced power generation for reverse electrodialysis, J Membrane Sci, 516 (2016) 162-171.

[143] W.Y. Hsu, J.R. Barkley, P. Meakin, Ion percolation and insulator-to-conductor transition in Nafion perfluorosulfonic acid membranes, Macromolecules, 13 (1980) 198-200.

[144] C. Peng, W. Zhang, H. Gao, Y. Li, X. Tong, K. Li, X. Zhu, Y. Wang, Y. Chen, Behavior and Potential Impacts of Metal-Based Engineered Nanoparticles in Aquatic Environments, Nanomaterials-Basel, 7 (2017) 21.

[145] X.F. Li, H.M. Zhang, Z.S. Mai, H.Z. Zhang, I. Vankelecom, Ion exchange membranes for vanadium redox flow battery (VRB) applications, Energ Environ Sci, 4 (2011) 1147-1160.

[146] J.G. Hong, B. Zhang, S. Glabman, N. Uzal, X. Dou, H. Zhang, X. Wei, Y. Chen, Potential ion exchange membranes and system performance in reverse electrodialysis for power generation: A review, J Membrane Sci, 486 (2015) 71-88.

[147] B.P. Zhang, J.G. Hong, S.H. Xie, S.M. Xia, Y.S. Chen, An integrative modeling and experimental study on the ionic resistance of ion-exchange membranes, J Membrane Sci, 524 (2017) 362-369.

[148] X. Tong, B. Zhang, Y. Fan, Y. Chen, Mechanism exploration of ion transport in nanocomposite cation exchange membranes, Acs Appl Mater Inter, 9 (2017) 13491-13499.

[149] R.G. Larson, L.E. Scriven, H.T. Davis, Percolation Theory of Residual Phases in Porous-Media, Nature, 268 (1977) 409-413.

[150] P. Sotta, D. Long, The crossover from 2D to 3D percolation: Theory and numerical simulations, Eur Phys J E, 11 (2003) 375-387.

[151] P. Dean, A New Monte Carlo Method for Percolation Problems on a Lattice, P Camb Philos Soc, 59 (1963) 397-&.

[152] A. Sur, J.L. Lebowitz, J. Marro, M.H. Kalos, S. Kirkpatrick, Monte-Carlo Studies of Percolation Phenomena for a Simple Cubic Lattice, J Stat Phys, 15 (1976) 345-353.

[153] Y.X. Bai, Y.F. Li, Preparation and characterization of crosslinked porous cellulose beads, Carbohyd Polym, 64 (2006) 402-407.